N_2 state population in Titan's atmosphere

P. Lavvas[a], R.V. Yelle[b], A. Heays[c], L. Campbell[d], M.J. Brunger[d,e], M. Galand[f], V. Vuitton[g]

[a] *Groupe de Spectroscopie Moléculaire et Atmosphérique, Université de Reims, Champagne-Ardenne, CNRS UMR 7331, France*
[b] *Lunar and Planetary Laboratory, University of Arizona, 1629 E University Blvd, 85723,AZ, USA*
[c] *Leiden Observatory, Leiden University, P.O. Box 9513, 2300 RA Leiden, The Netherlands*
[d] *School of Chemical and Physical Sciences, Flinders University, GPO Box 2100, Adelaide, SA 5001, Australia*
[e] *Institute of Mathematical Sciences, University of Malaya, 50603 Kuala Lumpur, Malaysia*
[f] *Space and Atmospheric Physics Group, Department of Physics, Imperial College London*
[g] *Univ. Grenoble Alpes, CNRS, IPAG, F-38000 Grenoble, France*

Abstract

We present a detailed model for the vibrational population of all non pre-dissociating excited electronic states of N_2, as well as for the ground and ionic states, in Titan's atmosphere. Our model includes the detailed energy deposition calculations presented in the past (Lavvas et al., 2011) as well as the more recent developments in the high resolution N_2 photo-absorption cross sections that allow us to calculate photo-excitation rates for different vibrational levels of singlet nitrogen states, and provide information for their pre-dissociation yields. In addition, we consider the effect of collisions and chemical reactions in the population of the different states. Our results demonstrate that above 600 km altitude, collisional processes are efficient only for a small sub-set of the excited states limited to the A and W(ν=0) triplet states, and to a smaller degree to the a$'$ singlet state. In addition, we find that a significant population of vibrationally excited ground state N_2 survives in Titan's upper atmosphere. Our calculations demonstrate that this hot N_2 population can improve the agreement between models and observations for the emission of the c_4' state that is significantly affected by resonant scattering. Moreover we discuss the potential implications of the vibrationally excited population on the ionospheric densities.

Keywords: Titan, Airglow, Atmospheric heating, Vibrational population, Pre-dissociation

1. Introduction

Airglow (induced by solar photons) and aurora (by magnetospheric particles) are fundamental molecular processes that allow us to characterize the high altitude regions of planetary atmospheres. For the N_2-rich atmosphere of Titan (as well as those of the Earth, Triton, and Pluto) the emission spectrum of excited nitrogen demonstrates multiple bands from the plethora of excited electronic states available and covers a large part of the electromagnetic spectrum. Airglow is just one of the processes that take place at the high altitude regions of planetary atmospheres, though, the other being the collisional de-excitation of the different N_2 states that eventually defines the atmospheric local heating rate. Therefore, a detailed description of the N_2-state population is necessary for understanding these two processes. In this study we present a new N_2-state model focusing on Titan's atmosphere.

The analysis of Cassini/UVIS Titan limb airglow measurements at EUV wavelengths reveals the dominance of the Carroll-Yoshino (CY) band system and of multiple atomic nitrogen (NI) emission lines, while in the FUV part of the spectrum, the Lyman-Birge-Hopfield (LBH) and the Vegard-Kaplan (VK) systems provide the major contributions (Ajello et al., 2007, 2008, 2012; West et al., 2012; Stevens et al., 2011, 2015). Further significant additions arise from the Birge-Hopfield (BH) band system and scattering from atomic hydrogen (Stevens et al., 2011), while scattering from aerosol particles appears at the longest wavelength region of the observed disk spectra (λ >150 nm, Ajello et al., 2008). These observations confirm previous detections from Voyager/UVS and clarify the relative contributions of the CY(0,0) and NI in the observed spectra (see Stevens, 2001, and references therein). Moreover the Cassini observa-

tions demonstrate the dominance of the solar energy input in the dayglow measurements (Stevens et al., 2011), but also reveal for the first time emissions from Titan's nightside that are driven by energetic particles originating from Saturn's magnetosphere (Ajello et al., 2012; West et al., 2012; Lavvas et al., 2014).

Calculation of the atmospheric airglow requires a detailed simulation of the populations of the different nitrogen states, which are defined by the excitation rate from the incident energy flux and the de-excitation through emission (leading to airglow) and collisions. Models for these processes were originally developed for the Earth's atmosphere and subsequently modified for application on Titan. In the most recent applications, the Atmospheric Ultraviolet Radiance Integrated Code (AURIC) (Strickland et al., 1999; Stevens, 2001) was used for the interpretation of Titan's ultraviolet emissions observed by Cassini and allowed the retrieval of the atmospheric density (Stevens et al., 2015). Similarly, Bhardwaj and Jain (2012) evaluated the population of the N_2 triplet states in Titan's atmosphere and reported the anticipated emissions under different geometry and solar conditions for the dominant Vegard-Kaplan band observed by Cassini in the FUV. Although these models are suitable for the investigation of the atmospheric airglow, they follow only a limited number of excited states and do not discuss the ground state properties. Therefore they cannot provide a complete picture of the N_2 state population that is required for the evaluation of the energy transfer in the atmosphere. In addition, the latest developments in the theoretical investigation of the N_2 optical properties have an important impact on the evaluation of the singlet state properties, thereby necessitating a reassessment of the state populations.

In this study we developed a new model for the N_2 states' population, specifically for Titan. The advantage of our model is that it calculates the population of all non pre-dissociating states of N_2 and utilizes the detailed energy deposition calculations for Titan's atmosphere we have performed in the past (Lavvas et al., 2011). The latter include the high-resolution cross sections of N_2 derived from theoretical calculations, which only became available in recent years (Lewis et al., 2005a; Heays et al., 2011), and have important ramifications for the energy deposition in the atmosphere and the excitation of different electronic states (see Section 2). In addition, our model includes a detailed description of the collisional processes that could affect the different states, including chemical reactions, suitable for Titan's atmosphere. Thus, our model can calculate emission rates in the whole spectrum and at different altitudes in Titan's atmosphere, which can be used for the evaluation of the airglow.

Moreover, we specifically focus here on the resulting vibrational distribution of the ground state that has not been addressed in the previous studies. The presence of vibrationally excited N_2 can have important consequences for the atmospheric chemistry; excited molecules can partake in processes that are energetically forbidden for the more abundant ground state molecules, in this way allowing for chemical reactions that normally are not considered possible under Titan's atmospheric conditions. Such mechanisms have been identified in the Earth's atmosphere where the N_2 vibrational population has an important influence on the ionospheric electron density (see Campbell et al., 2006, and references therein).

In the following sections we provide a detailed description of the model (Section 2), followed by the presentation of the model results on a specific case study that corresponds to Titan's atmospheric conditions during the T40 flyby (Section 3). The local emissions generated under the simulated conditions are presented in Section 4, while we calculate the implications of the ground state vibrational distribution on the resonant scattering of the singlet states in Section 5. The role of the N_2 states in the atmospheric heating is discussed in Section 6, and in Section 7 we discuss the possible consequences of our results on the atmospheric properties. Final conclusions are provided in Section 8. A detailed application of the model to specific Cassini observations, as well as the implications for the overall heating efficiency in Titan's atmosphere will be presented in future studies.

2. Model description

Solar energy can excite the ground electronic state of N_2 ($X\ ^1\Sigma_g^+$) to a large number of excited electronic states. In our calculations we include the major singlet (a $^1\Pi_g$, a$'$ $^1\Pi_g$, w $^1\Delta_u$, b $^1\Pi_u$, b$'$ $^1\Sigma_u^+$, c_3 $^1\Pi_u$, c_4' $^1\Sigma_u^+$, o_3 $^1\Pi_u$, e/c_4 $^1\Pi_u$, e$'/c_5'$ $^1\Sigma_u^+$) and triplet (A $^3\Sigma_u^+$, B $^3\Pi_g$, W $^3\Delta_u$, B$'$ $^3\Sigma_u^-$, C $^3\Pi_u$, E $^3\Sigma_g^+$, D $^3\Sigma_u^+$) states of neutral nitrogen, and some of the doublet states of N_2^+ (X $^2\Sigma_g^+$, A $^2\Pi_u$, B $^2\Sigma_u^+$). For each state we calculate the vibrational population up to the first 21 energy levels above the ground state of

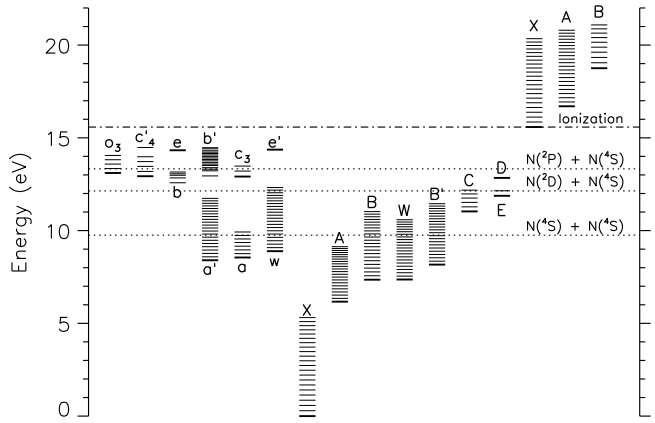

Figure 1: Vibrational energy levels, relative to the ground state, for the N_2 states we consider. Thick bars correspond to the ground vibrational level (ν=0) for each state and thin bars present higher levels. We only present levels that do not completely pre-dissociate and for which we calculate populations. Parameters for the calculation of the energy levels of the triplet, doublet and lower energy singlet states (a, a′, w) are from Laher and Gilmore (1991), while for the other singlet states the energy levels are calculated by the CSE model (see text). The horizontal lines mark the energies for different dissociation channels (dotted lines), as well as the first ionization limit (dash-dotted line).

each electronic state[1] (Fig. 1). We do not follow the rotational population within each level, as this degree of detail would be a formidable computational task for the purpose of our study. We do discuss though the implications of the rotational levels for the resonant scattering of the singlet states. For many of the states, pre-dissociation dominates thereby nulling the population for some of their levels. In this section we discuss in detail the radiative and collisional processes included in the calculations, as well as the limitations of the study.

2.1. Direct excitation & predissociation

Direct population of the different states is induced by interaction of photons and photoelectrons with the ground state. Usually the contribution of photon excitation is neglected in studies of N_2 airglow because only a small population of high energy singlet states can be excited through photo-absorption, and because most of the vibrational levels of these states strongly pre-dissociate. Moreover, a thorough evaluation of the photon excitation was not possible until now due to the lack of state-specific photo-absorption cross sections and pre-dissociation yields. Information for these parameters is now available through theoretical studies and we present below a thorough evaluation of the contribution of photon excitation.

Our fluxes of photons and photoelectrons are based on our previous study of energy deposition in Titan's atmosphere (Lavvas et al., 2011). For a given solar spectrum at the top of Titan's atmosphere the model calculates the energy-dependent photon and electron fluxes at different altitudes, taking into account the spherical geometry of the system. The model includes the high resolution theoretical cross sections for the neutral dissociation of N_2 (Lewis et al., 2005b, 2008), which were shown to have an important impact on the resulting production rates of different N_2 products (Lavvas et al., 2011). Moreover we updated these cross sections with the latest calculations that include a better description of the state specific cross sections (Heays et al., 2014). In addition, we also updated the nitrogen photo-ionization cross section with the high resolution measurements of Shaw et al. (1992) between the ionization threshold and ∼49 nm. For the photoelectrons we consider excitation to all of the electronic states and perform the electron degradation calculations assuming local energy deposition (LED). Comparison with calculations of photoelectron energy deposition including transport shows that the LED approach is valid below ∼1200 km (Lavvas et al., 2011), therefore our current results will be valid below this altitude limit, which is well within the altitudes of observed airglow (Stevens et al., 2011).

Finally, for both photons and photoelectrons we assume only excitation from the ν=0 level of the ground electronic state. The only exceptions are the electron impact excitation of the ground state to its different vibrational levels for which we have cross sections for transitions among all vibrational levels (Campbell et al., 2004), and the electron impact excitation of the A and B ion states from the ground ion state with cross sections from Crandall et al. (1974). Below we discuss in detail the methods applied for the evaluation of the excitation rate of each state/level.

2.1.1. Photons

The lack of a permanent dipole in N_2 limits the photon absorption cross section to high energy photons with wavelengths $\lambda < 100$ nm, while the singlet nature of the ground state does not allow for the excitation of the triplet states (spin forbidden transi-

[1]For simplicity the term *state* will always refer to an electronic state and the term *level* to a vibrational level.

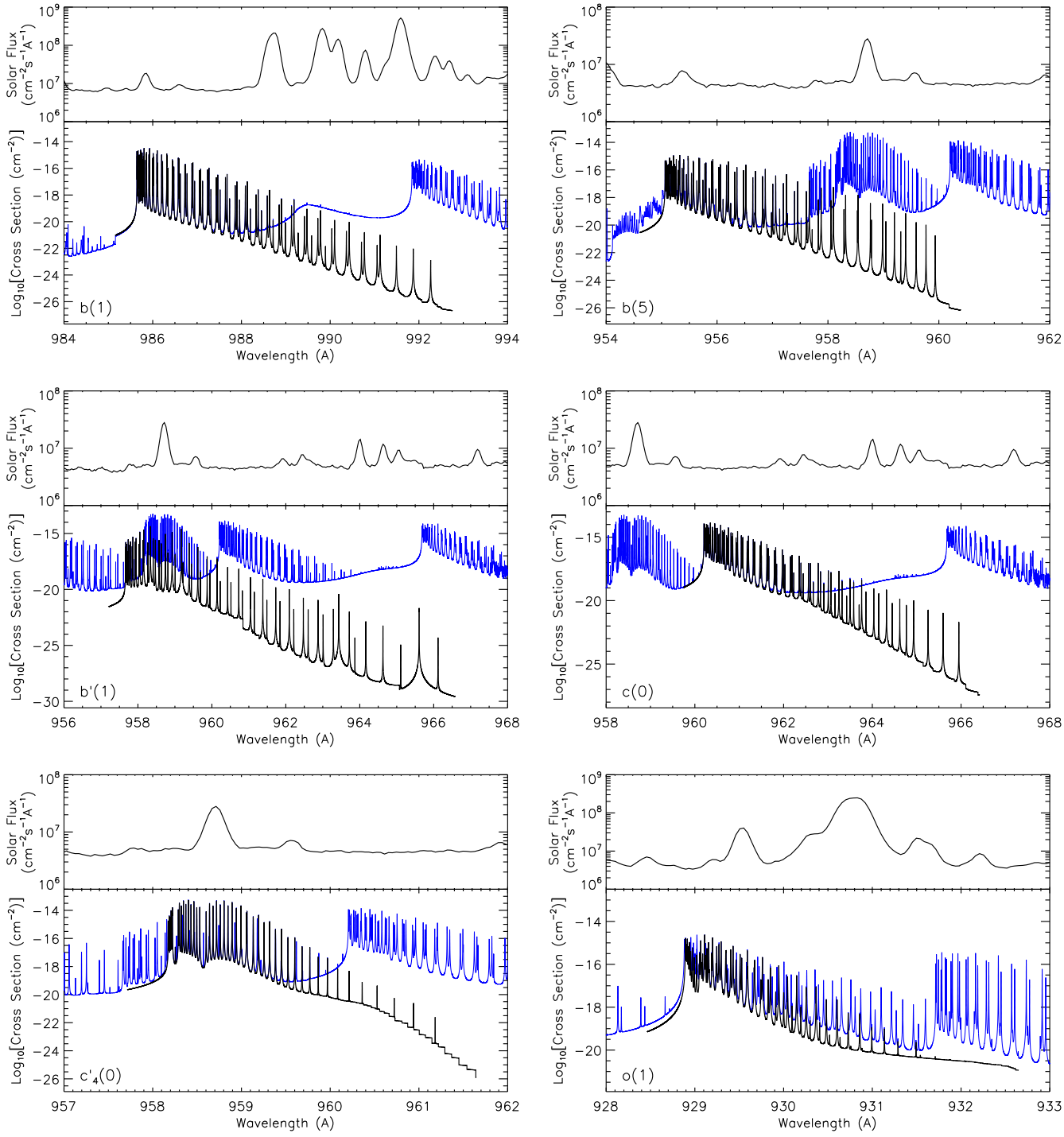

Figure 2: Theoretical photoabsorption cross sections for excitation of N_2 to different excited singlet states. The panels compare the partial cross sections (black) with the total photo absorption cross section (blue). The top panel for each state presents a high resolution spectrum of the solar flux (at 1 A.U.) in the same region of the spectrum from Lavvas et al. (2011), that allows for the correlation of solar emissions with N_2 absorption features.

tions). Direct dipole-allowed excitation by photons is limited to the excitation of singlet states of opposite (ungerade) parity to the ground state ($X\ ^1\Sigma_g^+$). The major contribution in the photoabsorption cross section occurs from two valence ($b\ ^1\Pi_u$, $b'\ ^1\Sigma_u^+$) and three Rydberg ($c_4'\ ^1\Sigma_u^+$, $c_3\ ^1\Pi_u$, $o_3\ ^1\Pi_u$) states (Stark et al., 2005, 2008). Most of the vibrational levels of these states pre-dissociate completely and only a small sub-

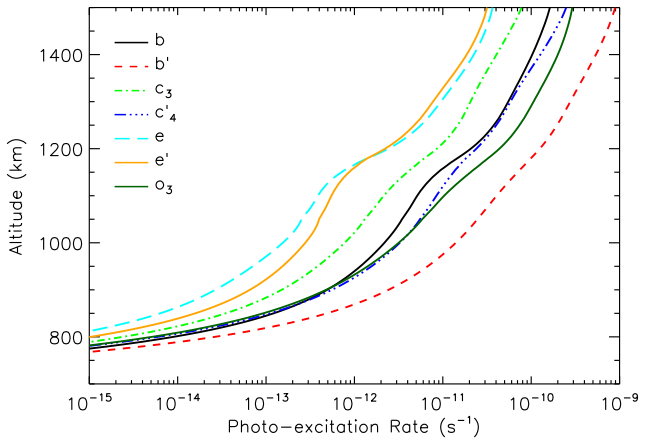

Figure 3: Photo-excitation rates of singlet states included in the calculations. The profiles correspond to the sum of all vibrational levels considered for each state. Atmospheric and solar illumination conditions (solar zenith angle of 60°) correspond to those presented in the case study below (Section 3).

set leads to photo-excitation. These correspond to the states/levels $b\ ^1\Pi_u(\nu$=1,4-7), $b'\ ^1\Sigma_u^+(\nu$=1,4-19), $c_4'\ ^1\Sigma_u^+(\nu$=0-4,6), $c_3\ ^1\Pi_u(\nu$=0-2), and $o_3\ ^1\Pi_u(\nu$=0-4). In addition, we consider in our calculations the e $^1\Pi_u(\nu$=0) and e$'\ ^1\Sigma_u^+(\nu$=0) levels that also do not completely pre-dissociate.

The evaluation of the excitation cross sections for these states has been a formidable experimental task with the limited information available. The reason for this difficulty arises from the overlap of bands with different pre-dissociation yields. Therefore, the use of segments of the total photo-absorption cross section for the estimation of the excitation rate of different states leads to overestimations. The latest developments in the high resolution theoretical calculations for the N_2 cross sections (Heays et al., 2011, and references therein), resulted in a breakthrough in our understanding of the interaction of the different molecular states and the role of these interactions in defining the molecular cross section and the magnitude of pre-dissociation of different states/levels (see discussion below).

These theoretical calculations allow us to extract the partial cross section for each state. Figure 2 provides an example of the partial photo-absorption cross sections we use in our calculations, where we compare them with the total photo-absorption cross section and the solar flux distribution in the spectral region of interest for each band. A spectral region that most characteristically demonstrates the advantage of using the partial cross sections is the region between 95.5 and 96.5 nm, where four different bands, the b(ν=5), b$'$(ν=1), $c_3(\nu$=0), and $c_4'(\nu$=0), overlap to different degrees. All these states/levels predissociate only partially, thus their individual excitation rates are required for a correct assessment of their resulting population.

We use these partial cross sections and the total N_2 cross sections, evaluated at different temperatures between 100 and 200 K appropriate for Titan's atmospheric conditions in our energy deposition calculations (see Lavvas et al., 2011), taking also into account absorption by methane. Note that due to the variation of the N_2 cross sections with tempera-

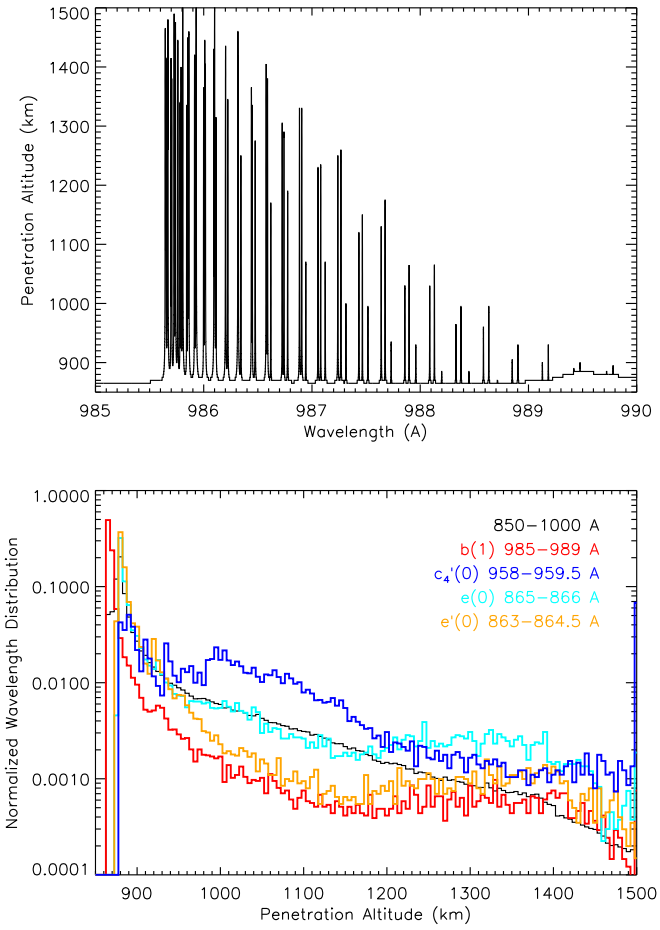

Figure 4: Top: Photon penetration altitudes in the region of the b(ν=1) excitation, showing that due to the highly variable magnitude of the cross section, photons can be absorbed between 1500 and 850 km altitude. Penetration altitudes are calculated from the $\tau = 1$ condition. Bottom: Normalized histograms for the altitude of photon penetration for different N_2 bands (thick colored lines) and for the whole region of the high resolution cross sections (thin black line).

ture, we need to consider the variation of the cross section along each segment of the slant column opacity, which significantly increases the computational time. The resulting photo-excitation rates for the singlet states are shown in Fig. 3, and correspond to the atmospheric and solar illumination conditions of the case study presented in the following section. The profiles presented correspond to the sum of all vibrational levels considered for each state. Photons able to excite these states are absorbed above 800 km, thus excitation is limited to higher altitudes.

The behavior of the excitation profiles depends strongly on the distribution of solar flux and opacity within each band. For example, photons able to excite the b(ν=1) state are absorbed in multiple altitudes ranging between 1500 km for wavelengths with the highest cross sections to ∼850 km for the lower troughs between the absorption peaks (Fig. 4). If we make a histogram of the distribution of altitudes at which the different photons can penetrate we can see that each band has a significantly different behavior from the corresponding distribution for the total photoabsorption range (85-100 nm) of the high resolution cross sections (Fig. 4). The latter shows a rather monotonic increase of the number of photons deposited at lower altitudes, due to the prevalence of troughs over peaks in the cross sections. On the contrary, the band distributions reveal local maxima at high altitudes that imply that the photo-excitation rates for these states can have local inversion points for the high and low magnitude cross section regions as demonstrated by our results (Fig. 3). For some cases (e.g. e(ν=0) and e$'$(ν=0)) the inversion is so efficient that the production rates of these states demonstrate double peaks (see Section 3). These characteristics are further modulated by the variation of the solar flux over each band region.

2.1.2. Photoelectrons

Among the singlet states, only the low lying a, a$'$, and w states are not strongly pre-dissociated, but they are optically forbidden because of parity considerations. Therefore their populations, along with the populations of the triplet states, are predominantly populated by photoelectron excitation.

In order to simulate the population of the different vibrational levels of each electronic state, we need to know the state and level specific electron impact cross section. With the exception of the ground state, such cross sections are not available in the literature. Our current knowledge is limited to the manifold cross section for the excitation of the ground state to all vibrational levels of an excited state. In order to distribute the manifold cross section to the different vibrational levels, we assume that we have vertical transitions, i.e. we estimate the partial cross section by the product of the manifold cross section with the Franck-Condon (FC) factor appropriate for the excitation of the ground state to each vibrational levels of the excited state. A small modification is further required in order to take into account the threshold energy for the different vibrational levels of the excited electronic state, for which we follow the methodology of Borst (1973). The latter accounts for a small shift of the resulting partial cross section to higher energies by an amount equal to the energy difference between the excited vibrational level and the ν=0 level of the excited electronic state. Finally, in order to conserve the total absorbed energy we renormalize the partial cross sections to the total measured cross section. Such an approach is approximate, but is a common tactic in similar studies of energy deposition and airglow for the Earth (Cartwright, 1978; Gordillo-Vazquez, 2010), which leads to good agreement with observations for the low-lying energy states.

As the levels of the higher energy singlet states are strongly perturbed by their mutual interactions, the relative excitation probabilities of each vibrational band requires the inclusion of these modifications in the resulting wave function of each state/level. Thus, the FC factors that are derived from the unperturbed wave functions are not suitable in this case. For these states we use the probabilities reported in Malone et al. (2012) for the b(ν=0-14), c_3(ν=0-3), o_3(ν=0-3), c_4'(ν=0-3) and b$'$(ν=0-10) states. For the b$'$ state, excitation from the ground state favors predominantly higher vibrational levels from those reported in Malone et al. (2012), with the peak vibrational overlap occurring for ν=16 (Stahel et al., 1983; Ajello et al., 1989; Malone et al., 2012). In order to extend to higher vibrational levels for this state we used the excitation probabilities for ν=11-21 reported by Ajello et al. (1989), after scaling them to the total probability for transitions into these levels as reported by Stahel et al. (1983).

For the ground electronic state, we have both theoretical studies and laboratory measurements for the electron-impact excitation of the different vibrational levels. This process proceeds through a resonance

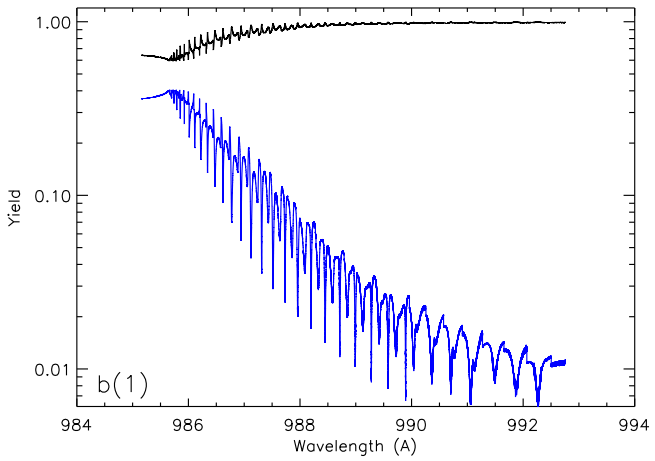

Figure 5: Yields for pre-dissociation (black) and photo-excitation (blue) for the b(ν=1) state.

with the N_2^- anion that rapidly auto-ionizes leaving N_2 in a different vibrational level depending on the energy of the impinging electron. A recent review of these cross sections can be found in Campbell et al. (2004) where comparison between measurements and theory is made. We use the cross sections from this study, with updates from the latest theoretical calculations by Laporta et al. (2012) for $\nu > 10$. We include both the forward and reverse excitation cross sections, the latter calculated based on the principle of detailed balance.

2.1.3. Pre-dissociation

The pre-dissociation of the different bound N_2 states strongly depends on the symmetry of each state and its coupling with the dissociating continua. The mechanisms of pre-dissociation depend sensitively on the energy overlap of different molecular features at the detail of rotational energies. Since we do not describe our system at rotational detail, the pre-dissociation of the different vibrational levels we consider in our study corresponds to the average properties over the rotational population of each level. Thus we use a constant pre-dissociation probability, f_{dis}, for each state/level, the value of which is retrieved from the literature.

For the gerade singlet bound states only the $a\ ^1\Pi_g$ state is observed to dissociate for vibrational levels $\nu \geq 7$. The dissociation occurs through coupling to the $A'\ ^5\Sigma_g^+$ continuum, yielding $N(^4S) + N(^4S)$ (van der Kamp et al., 1994).

Pre-dissociation of the lowest $^1\Pi_u$ states (b,c,o) was quantitatively explained for the first time through spin-orbit coupling of the singlet manifold states with the $^3\Pi_u$ manifold (Lewis et al., 2005b, 2008). More specifically this coupled-channel Schrödinger equation (CSE) model showed that the b-state is strongly coupled to the C-state, which is itself strongly electrostatically coupled to the F-, G-, and C-$'$ states, where pre-dissociation occurs through the continuum of the latter, yielding $N(^4S) + N(^2D)$. Moreover, the pre-dissociation yields of each state/level depend on the rotational levels involved (Haverd et al., 2005; Lewis et al., 2005a; Wu et al., 2012), thus can be used as a probe of the rotational temperature. This particularly holds for the b(ν=1) level that exhibits the strongest emission from this state, and contributes to the UVIS EUV observations of Titan's airglow (Stevens et al., 2011). The pre-dissociation theoretical yield for b(ν=1) ranges from ∼20% for J=1 to ∼100% at J=25 (Lewis et al., 2005a).

Pre-dissociation of the c_4'-state proceeds through rotational coupling to the $c_3\ ^1\Pi_u$ state, that readily dissociates through spin-orbit coupling to the C-, F-, G-, and C$'\ ^3\Pi_u$ states (Liu et al., 2008, 2009). There is a strong dependence on the rotational energy of the molecule with no pre-dissociation for J=0, and increasing efficiency for higher rotational levels. This picture becomes more complex through the interaction of the c_4'-state with the b- and b'-states: interaction with the b'-state modifies the energy levels and FC factors for both states. As a result of this interaction there is an important crossing between the $c_4'(\nu = 0)$ and $b'(\nu = 1)$ levels for specific rotational levels that results in an overlap of their emissions. This phenomenon further affects the pre-dissociation rates because the J dependence of the b' pre-dissociation is weaker than that of the c_4'.

The latest theoretical calculations for the N_2 photoabsorption cross sections allow us to quantitatively evaluate the pre-dissociation yield for each of the singlet states at any temperature. Figure 5 presents an example of the yields (pre-dissociation and photo-excitation) for the b(ν=1) state that demonstrates the variable character of the yields over the spectral range of this band. The band average yield for pre-dissociation, $< f_{dis} >$, for this state would be ∼90%. Yet, the cross section, σ_λ, within the band is variable (see Fig. 2). Thus, an accurate averaging for the yield would be :

$$< f_{dis} >= \frac{\int \sigma_\lambda f_{dis,\lambda}}{\int \sigma_\lambda}, \qquad (1)$$

which for the b(ν=1) state gives an average pre-dissociation yield of ∼65%. Note that σ_λ is the partial cross section of each state/level and that the derived yields correspond only to the partial state cross section and not the manifold cross section. The corresponding yields for all pre-dissociating singlet states included in the model are provided in Table 1. Values are provided for three different assumed temperatures in the calculations of the cross sections (100, 150, and 200 K). The variance of the yields among these conditions is small and in our calculations we assumed the yields at 150 K. These yields can be further modified by the variation of the solar flux within each band, but our calculations show that this effect is rather small.

Table 1: Average dissociation yields for singlet states. States in boldface characters have pre-dissociation yields less that 95%.

	$< f_{dis} >$		
State	100K	150K	200K
b(1)	0.634	0.657	0.678
b(4)	0.994	0.994	0.994
b(5)	0.979	0.974	0.968
b(6)	0.957	0.958	0.959
b(7)	0.969	0.972	0.974
b′(1)	0.453	0.444	0.440
b′(4)	0.903	0.920	0.926
b′(5)	0.683	0.683	0.684
b′(6)	0.938	0.938	0.938
b′(7)	0.485	0.531	0.579
b′(8)	0.930	0.930	0.930
b′(9)	0.730	0.751	0.768
b′(10)	0.965	0.965	0.966
b′(11)	0.946	0.946	0.946
b′(12)	0.834	0.827	0.819
b′(13)	0.971	0.971	0.971
b′(14)	0.981	0.980	0.980
b′(15)	0.978	0.978	0.978
b′(16)	0.949	0.950	0.951
b′(17)	0.988	0.987	0.986
b′(18)	0.975	0.975	0.975
b′(19)	0.975	0.976	0.977
c(0)	0.980	0.979	0.978
c(1)	0.976	0.980	0.983
c(2)	0.985	0.985	0.985
c'_4(0)	0.109	0.133	0.155
c'_4(1)	0.689	0.694	0.699
c'_4(2)	0.800	0.797	0.795
c'_4(3)	0.826	0.826	0.827
c'_4(4)	0.752	0.779	0.798
c'_4(6)	0.922	0.924	0.928
e(0)	0.925	0.927	0.928
e′(0)	0.491	0.494	0.524
o(0)	0.951	0.959	0.962
o(1)	0.989	0.990	0.990
o(2)	0.991	0.991	0.991
o(3)	0.990	0.990	0.990
o(4)	0.712	0.716	0.717

In addition to the above, resonant scattering of the c'_4(0)-X(0) emission also affects the pre-dissociation of the c'_4-state, because of the gradual population of the X(1) vibrational level through the $c'_4(0)$-$X(\nu'')$ transitions. Photons emitted from the $c'_4(0)$-$X(1)$ transition are resonantly absorbed by the near coincident b(ν=2) state that completely pre-dissociates, reducing in this way the emission from the c'_4-state (Stevens et al., 1994; Stevens, 2001; Campbell et al., 2005). We discuss further below the implications of this mechanism.

For the triplet states, pre-dissociation starts within a narrow range of vibrational levels of the B-state ($13 \leq \nu \leq 18$). This process occurs due to the close alignment of these energy levels to those of the $A'\,^5\Sigma_g^+$ continuum, as for the a-state (Geisen, H, Neuschäfer, D and Ottinger, Ch, 1990). Similarly, the C-state pre-dissociates for $\nu \geq 5$ (Lofthus and Krupenie, 1977). Theoretical calculations for the D-state show that pre-dissociation rapidly increases with increasing vibrational levels and rotational energy (Lewis et al., 2008). Thus, we consider that all levels above the ground level pre-dissociate for this state. Similarly, for the E-state pre-dissociation dominates for $\nu \geq 2$.

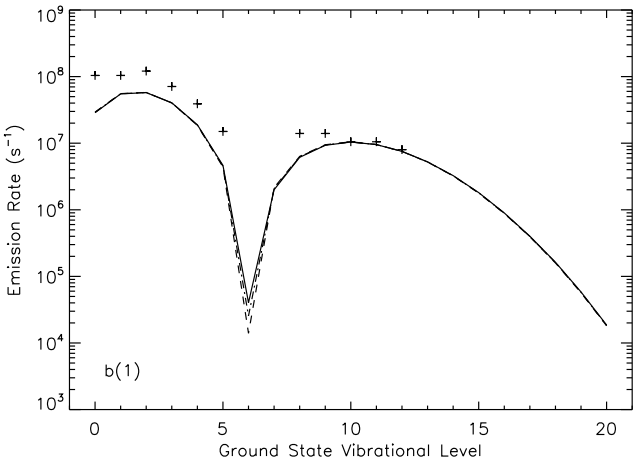

Figure 6: Comparison between radiative emission rates of the b(ν=1) levels to different levels of the ground state. Lines present the theoretical rates evaluated with a pre-dissociation yield of 65% at different temperatures (solid for 200 K, dashed for 100 K and dash-dotted for 150 K) and the crosses are the rates from Gilmore et al. (1992) assuming a pre-dissociation yield of the 10.5% for the b(ν=1) level.

For all other states we do not consider pre-dissociation.

2.2. Radiative Transitions

Table 2 provides a complete list of the radiative transitions included in our calculations. The radiative de-excitation rates among the different vibrational levels are taken from the studies of Cartwright (1978), Gilmore et al. (1992) and Campbell et al. (2010) for the doublet and triplet states. Typically, transitions occur from a higher to a lower electronic state. Depending on the involved levels, though, transitions can take place in the inverse direction as well (intrasystem crossing). The bands for which inverse transitions are possible are presented by the double arrows in Table 2. We also provide the largest radiative transition rate for each band in order to present the relative lifetimes of the different states. For the w→X transition, we estimated the rates for the different levels using the total radiative lifetime for the w-state and the FC factors reported in Gilmore et al. (1992), while for the a′ →X transition we followed a similar approach using the lifetime (13 ms) reported for this state by Tilford and Benesch (1976).

For the singlet states, Gilmore et al. (1992) provide rates for de-excitation of the b(ν=1) and c$'_4$(ν=0-4,6) levels to the first vibrational levels of the ground state which are based on experimental measurements and assumptions about the pre-dissociation yield of each state. For example, emission rates for the b(ν'=1) -X(ν'') transitions were calculated assuming a pre-dissociation yield of 10.5% for this level (Gilmore et al., 1992), while our calculated yield for this level is 65%. Therefore, in order to be consistent with the excitation rates we use for the singlet states, we used the radiative transition rates evaluated from the CSE model, which reflect the temperature conditions for which the N_2 cross sections are evaluated. Taking into account the differences in the yields assumed, the theoretical results are consistent with the experimental measurements (Fig. 6).

2.3. Collisional Transitions

Collisions of the electronically/vibrationally excited nitrogen molecules with other molecules or atoms result in a redistribution of the excited state energy and population. These processes, contrary to the radiative transitions described above, depend on the atmospheric temperature. The type of energy redistribution depends on the nature of the collision and can be generally separated into intramolecular or intermolecular processes (Ottinger et al., 1995). In the first case the redistribution occurs only on the target molecule. If we designate as $N_2(x, \nu)$ a molecule in electronic state x and vibrational level ν colliding with species M, the intramolecular process can be described as:

$$N_2(x, \nu) + M \rightarrow N_2(x', \nu') + M.$$

If the electronic state after the collision remains the same ($x = x'$) then we have only a vibrational redistribution and the excess energy is distributed to the translational and rotational degrees of freedom. If the electronic state changes as well, the transition occurs in such a way that the internal energy of the excited molecule is about the same before and after the collision (quasi-resonant transitions). If the collision partner is another molecule (e.g. $N_2(y, v)$) then we also have the option of an intermolecular collision in which there is an energy transfer between the internal degrees of freedom of the two molecules:

$$N_2(x, \nu) + N_2(y, v) \rightarrow N_2(x', \nu') + N_2(y', v').$$

In this case, the transitions occur again in a quasi-resonant mode where the total internal energy of the system before and after the collision is about the same. Intermolecular and intramolecular processes can have comparable importance to the energy redistribution among different states. Moreover, collisions that induce changes among different electronic states are particularly important from an observational point of view since they allow for the enhancement or decrease of airglow emissions from specific bands, relative to the emissions anticipated from pure radiative transitions. A characteristic example is the orange airglow observed in the Earth's lower thermosphere and attributed to an excess emission from the second positive band (B→A), induced by the pumping of the triplet B-state population in collisions of the triplet A-state with ground state N_2 (Piper, 1994).

A large number of laboratory studies have addressed the measurement and interpretation of the different mechanisms involved in the collisional processes of excited nitrogen molecules. Due to the different types of possible reactions, many studies have extended the characterization of the reactions beyond the inter- or intra-molecular character, as will become obvious below. Most of these measurements focus on the longest lived metastable states, which are easier

Table 2: Radiative transitions included in the model.

	Transition	Band Name	Max A[s^{-1}]	(ν',ν'')	$\lambda(\mu m)$	Reference
Triplet	A $^3\Sigma_u^+ \rightarrow$ X $^1\Sigma_g^+$	Vegard-Kaplan	1.95(-1)	(19,1)	0.1435	[1]
	B $^3\Pi_g \leftrightarrow$ A $^3\Sigma_u^+$	First Positive	1.11(5)	(13,9)	0.5696	[1]
	W $^3\Delta_u \leftrightarrow$ B $^3\Pi_g$	Wu-Benesch	5.40(3)	(20,10)	1.0733	[1]
	B$'$ $^3\Sigma_u^- \leftrightarrow$ B $^3\Pi_g$	IR afterglow	2.29(4)	(10,5)	0.8212	[1]
	C $^3\Pi_u \rightarrow$ B $^3\Pi_g$	Second Positive	1.31(7)	(0,0)	0.3370	[1]
	E $^3\Sigma_g^+ \rightarrow$ A $^3\Sigma_u^+$	Herman-Kaplan	3.10(3)	(1,2)	0.2204	[1]
	E $^3\Sigma_g^+ \rightarrow$ B $^3\Pi_g$		1.56(2)	(1,0)	0.2587	[2]
	E $^3\Sigma_g^+ \leftrightarrow$ C $^3\Pi_u$		7.63(2)	(0,0)	1.471	[2]
	D $^3\Sigma_u^+ \rightarrow$ B $^3\Pi_g$	Fourth Positive	3.78(7)	(1,0)	0.2159	[2]
	D $^3\Sigma_u^+ \rightarrow$ E $^3\Sigma_g^+$		5.61(5)	(0,0)	1.283	[2]
Singlet	w $^1\Delta_u \rightarrow$ X $^1\Sigma_g^+$	Tanaka	1.25(8)	(7,0)	0.1220	[1]
	w $^1\Delta_u \leftrightarrow a$ $^1\Pi_g$	MCF2	4.77(3)	(19,12)	1.0024	[1]
	a $^1\Pi_g \rightarrow$ X $^1\Sigma_g^+$	Lyman-Birge-Hopfield	5.16(3)	(3,0)	0.1354	[1]
	a $^1\Pi_g \leftrightarrow a'$ $^1\Sigma_u^-$	MCF1	2.62(3)	(18,15)	1.4644	[1]
	a' $^1\Sigma_u^- \rightarrow$ X $^1\Sigma_g^+$	Fifth Positive	6.14(1)	(8,0)	0.1264	[1]
	b $^1\Pi_u \rightarrow$ X $^1\Sigma_g^+$	Birge-Hopfield I	2.08(8)	(4,0)	0.09658	[3]
	b' $^1\Sigma_u^+ \rightarrow$ X $^1\Sigma_g^+$	Birge-Hopfield II	2.18(8)	(5,4)	0.1019	[3]
	c_3 $^1\Pi_u \rightarrow$ X $^1\Sigma_g^+$		1.74(8)	(0,0)	0.09603	[3]
	c_4' $^1\Sigma_u^+ \rightarrow$ X $^1\Sigma_g^+$	Carroll-Yoshino	1.02(9)	(0,0)	0.09586	[3]
	c_4' $^1\Sigma_u^+ \rightarrow a$ $^1\Pi_g$	Gaydon-Herman	4.82(6)	(0,1)	0.2970	[2]
	e $^1\Pi_u \rightarrow$ X $^1\Sigma_g^+$		1.82(7)	(0,0)	0.08654	[3]
	e$'$ $^1\Sigma_u^+ \rightarrow$ X $^1\Sigma_g^+$		6.14(7)	(0,0)	0.08633	[3]
	o_3 $^1\Pi_u \rightarrow$ X $^1\Sigma_g^+$		2.44(8)	(0.1)	0.09676	[3]
Doublet	A $^2\Pi_u \leftrightarrow$ X $^2\Sigma_g^+$	Meinel	5.85(4)	(1,0)	0.9183	[1]
	B $^2\Sigma_u^+ \rightarrow$ X $^2\Sigma_g^+$	First Negative	1.14(7)	(0,0)	0.3912	[1]

[1] Gilmore et al. (1992), [2] Campbell et al. (2010), [3] CSE model

to investigate and at the same time are more important for the atmospheric modeling since they have a higher probability of being affected by collisions. Below we describe in detail the processes we have included in our calculations based on the available observations, while in Table 3 we provide an overview of all processes.

2.3.1. Triplet manifold

Most of the published laboratory investigations for the role of collisions focus on the triplet state manifold and specifically on transitions among the low lying A-, B-, W-, B′-, and C-states. Dreyer (1973) observed the deactivation of different vibrational levels of N_2 A(ν) by ground state N_2 X(0) and found that the collisions induced *vibrational − vibrational* transitions with a double quantum difference for the A-state accompanied with a single quantum increase of the ground state vibrational level:

$$\mathrm{A}(\nu) + \mathrm{X}(0) \rightarrow \mathrm{A}(\nu - 2) + \mathrm{X}(1).$$

In a more recent study Popov (2013) re-evaluated the results of this experiment taking into account the role of collisions of N_2 A-state molecules with atomic nitrogen formed in the apparatus, and derived an analytical formula for the rate of the above reaction:

$$k(\nu) = 1.1 \times 10^{-13} \nu(\nu - 1) \exp\left[-0.1 \frac{\Delta E}{\sqrt{T}}\right], \quad (2)$$

for $2 \leq \nu \leq 7$ and where ΔE (in cm^{-1}) is the energy difference between reactants and products (positive for exothermic transitions) and T, the temperature. For higher levels we use the rates from the theoretical study of Kirillov (2008) that provide consistent results with the experimental measurements at the low vibrational levels. For A(ν <2), collisions with N_2 lead to electronic quenching to the ground state with rates 3.7 $\times 10^{-16}$ and 3.4×10^{-16} $\mathrm{cm}^3\mathrm{s}^{-1}$ for ν=0 and ν=1, respectively (Dreyer, 1973).

Other types of reactions leading to electronic transitions are those of *energy pooling* in which two A-state molecules collide to generate molecules in the B- or C-state:

$$\mathrm{A}(\nu) + \mathrm{A}(\nu') \rightarrow \mathrm{B}(\nu'') + \mathrm{X}(\nu''')$$
$$\mathrm{A}(\nu) + \mathrm{A}(\nu') \rightarrow \mathrm{C}(\nu'') + \mathrm{X}(\nu''')$$

Table 3: Collisional processes included for each electronic state in the calculations, EQ: electronic quenching, EP: energy pooling, ICT: intersystem crossing transition, C: chemical reaction, VV: vibrational-vibrational, VT: vibrational-translational. The entries for each case present the states or species involved.

N_2 State	EQ	EP	ICT	C	VV	VT
A	X	B,C,X	B,W,X	CH_4,C_2H_2,C_2H_4,C_2H_6	X	
B	X		A,W,B′,X			
B′	X		B			
C	X				X	
W,E,D	X					
X^+				CH_4,e^-	X	X
A^+,B^+	X^+			e^-	X	X
X				CH_4	X	X
a	X		a′,w			
a′	X		a			
w	X		a			
b,b',c_3,c_4'	X					
o_3,e,e'	X					

Measurements for these rates are available only for collisions among the ν, ν'=0 and 1 vibrational levels of the A state resulting in population of the C(ν''=0-4) and B(ν''=1-11) vibrational levels (Piper, 1988a,b). For the vibrational level of the product ground state molecule we have chosen the level that corresponds to the closest quasi-resonant transition for each combination of the collision partners at ∼150 K (see Table 4). Energy pooling reactions affect the populations of the B- and C-states, but are not a significant loss mechanism for the A-state population.

On the contrary, electronic transitions induced by reaction with the ground state can be more important. In this case we have contributions from both intramolecular and intermolecular mechanisms (Bachmann et al., 1993; Ottinger et al., 1995). In the former case, collisions of ground state molecules with the N_2 A-state lead to the production of the N_2 B-state:

$$\mathrm{A}(\nu) + \mathrm{X} \leftrightarrow \mathrm{B}(\nu') + \mathrm{X}$$

These collisions are efficient for a combination of vibrational levels of similar energy and can work in both directions (Bachmann et al., 1992, 1993). On the other hand, collisions with excited vibrational levels of the ground state ($\nu' \geq 4$) lead to the production of the triplet B state through the intermolecular path:

$$\mathrm{A}(\nu) + \mathrm{X}(\nu') \rightarrow \mathrm{B}(\nu'') + \mathrm{X}(\mathrm{v}'''').$$

With the aid of isotopic labeling of the reactants it was possible to demonstrate that the latter reaction proceeds through the transfer of the A-state energy to the ground state molecule, instead of the transfer of the ground state's vibrational energy to the N_2 A-state (Piper, 1989, 1994). In addition, intersystem collisions appear to populate the low vibrational levels of the B-state, while the intrasystem collisions predominantly affect the higher vibrational levels, but the contributions of the two types have comparable magnitudes (Ottinger et al., 1995). The rates for the intrasystem processes in our calculations are based on the theoretical study of Kirillov (2008), for the calculation of intermolecular and intramolecular processes. The latter allows us to calculate the rates for all possible vibrational level combinations of the involved molecules, and at any temperature. Finally, we also include electronic quenching to the ground state with rates from Gordillo-Vazquez (2010).

The B triplet state is coupled to the A-, B′-, and W-states through collisions of an intramolecular type:

$$\mathrm{B}(\nu) + \mathrm{X} \leftrightarrow \mathrm{A}(\nu') + \mathrm{X}$$
$$\mathrm{B}(\nu) + \mathrm{X} \leftrightarrow \mathrm{W}(\nu') + \mathrm{X}$$
$$\mathrm{B}(\nu) + \mathrm{X} \leftrightarrow \mathrm{B}'(\nu') + \mathrm{X}.$$

Similar to the intersystem crossing discussed previously for radiative transitions, collisions can lead to electronic variations of these states for vibrational levels of similar energy (Bachmann et al., 1992, 1993). We calculate the rates for these processes based on the theoretical work of Kirillov (2008), while we also consider electronic quenching of the B-, B′- and W-states to the ground state with rates from Morrill and Benesch (1996).

For collisions of the triplet C-state the most recent measurements were made by Dilecce et al. (2006) and Pereira et al. (2010). The former investigated the relative role of vibrational redistribution within

Table 4: Energy pooling rates for the production of different vibrational levels of the B and C states from the collision of two A(0,1) state N_2 molecules. Units are 10^{-11}cm^{3}s^{-1}. Numbers in parenthesis give the vibrational level of the ground state closest to overall resonance between the energy levels of products and reactants (the numbers in italics show the only endothermic channel at 150 K).

Vib. Level	B			C		
(ν'')	k_{00}	k_{01}	k_{11}	k_{00}	k_{01}	k_{11}
0				2.6 (4)	3.4 (5)	<1.0 (5)
1		3.3 (19)		4.1 (3)	5.4 (4)	<2.0 (5)
2	1.6 (17)	3.0 (18)	14.7(19)	4.1 (2)	3.3 (3)	<1.0 (4)
3	0.4 (16)	4.2 (17)		2.8 (2)	2.2 (2)	<0.7 (3)
4	0.5 (15)	1.6 (16)	3.8 (17)	1.0 (1)	1.0 (1)	<0.6 (2)
5	0.7 (15)	1.6 (15)	4.5 (16)			
6	0.6 (14)	1.3 (*15*)	1.5 (15)			
7	0.6 (13)	1.3 (14)				
8	0.4 (12)	1.1 (13)				
9	0.8 (11)	0.9 (13)	1.6(13)			
10	1.8 (11)	2.8 (12)	1.3(12)			
11	0.3 (10)	0.4 (11)	1.0(12)			

the C-state to that of electronic quenching to lower laying electronic states. Their study provides rates for the vibrational relaxation for the $\nu = 0-4$ vibrational levels and the corresponding electronic quenching rates (Table 5), although an assignment of the product lower state was not possible. When we include these rates in our calculations we assume that the electronic quenching results in the production of the X(ν=0) state, while for the vibrational redistribution we consider only the path:

$$C(\nu') + X(0) \rightarrow C(\nu'') + X(\nu), \quad (3)$$

where ν is the ground state vibrational level closest to resonance for the given combination of ν' and ν'' (see Table 5). Pereira et al. (2010) investigated the temperature dependence of the quenching rates for the first two vibrational levels (ν'=0,1) and found that the electronic quenching rates have a small negative temperature dependence, while the vibrational redistribution rates demonstrate a stronger and positive dependence on temperature.

For the D- and E-triplet states we only consider electronic quenching to the ground state with rates estimated from the quenching rates of the B-state.

2.3.2. Singlet manifold

Collisions among N_2 molecules are the major process for the re-distribution of the vibrational level populations of the ground electronic state. Due to the lack of a permanent dipole moment the Vibrational-Vibrational (VV) and Vibrational-Translational (VT) transition rates for N_2 are difficult to measure, and

Table 5: Quenching rates for the C $^3\Pi_u$ state from Dilecce et al. (2006), including contributions from electronic quenching and vibrational redistribution within the C-state. Numbers in parenthesis correspond to the produced vibrational level of the ground state assumed in the calculations (see text). Units are 10^{-11} cm^{3}s^{-1}.

$\nu'' \setminus \nu'$	0	1	2	3	4
0	-	1.19(1)	0.528(2)	0.734(3)	0.736(3)
1	-	-	0.763(1)	0.464(2)	1.02(2)
2	-	-	-	0.36(1)	0.285(2)
3	-	-	-	-	0.105(1)
Elec.	1.14	1.95	2.989	4.782	7.714

theoretical calculations are required for these rates. The typical approach commonly used is that of a semiclassical theory where the translational and rotational degrees of freedom for the N_2 molecules are treated with a classical Hamiltonian, while the vibrational energy is quantized. Based on this approach and taking into account the long and short range interaction potentials among the colliding molecules calculations for both the VT and the VV transitions are possible (Kurnosov et al., 2010).

VT collisions are of the form:

$$X(\nu) + X(\nu') \leftrightarrow X(\nu - \Delta\nu) + X(\nu').$$

For the forward pathway of this reaction, vibrational energy is transformed to translational (or rotational) energy, thereby heating the atmosphere, while in the reverse reaction we have energy transfer from the translational/rotational degrees to the vibrational degrees of freedom, thereby causing cooling of the atmosphere. For the (kinetic) temperature of Titan's

atmosphere the reverse pathway is inefficient, while multi-quantum steps are only important for high vibrational levels at high temperatures (T>8000K, Billing and Fisher, 1979). For our study we therefore consider only single quantum transitions ($\Delta\nu$=1). We calculate the rates for this process based on the analytical formulation of Kirillov (1998).

VV collisions are of the form:

$$X(\nu) + X(\nu') \leftrightarrow X(\nu - \Delta\nu) + X(\nu' + \Delta\nu').$$

Here we can separate different options for the type of the transitions, such as single quantum transitions ($\Delta\nu = \Delta\nu' = 1$), multi-quantum symmetric transitions ($\Delta\nu = \Delta\nu' > 1$), and multi-quantum asymmetric transitions ($\Delta\nu \neq \Delta\nu'$). For N_2 collisions multi-quanta symmetric transitions have smaller rates than single quantum transitions and are important only for high vibrational levels (Cacciatore et al., 2005; Kurnosov et al., 2007). Asymmetric transitions can have rates comparable to single quantum transitions, but are limited to vibrational levels significantly larger than those investigated here. Thus, we only need to consider the single quantum transitions in our calculations. The rates we use for the VV collisions are taken from the analytical formulation for single quantum transitions from Kurnosov et al. (2010). As a general characteristic the rates peak in the near resonance region and increase for increasing vibrational level. Keep in mind that only for the imaginary case of a harmonic oscillator do these collisions result in a complete energy exchange among the different vibrational levels. In reality, the divergence of the N_2 vibrational potential from that of a harmonic oscillator with increasing ν makes the VV transitions either endothermic or exothermic depending on the vibrational levels involved.

For a given vibrational level, ν, production by VV collisions occurs from both the ν+1 and ν−1 levels at different rates. At the lower boundary (ν=0) of our simulated vibrational level space, production is possible only from the ν=1 level, while at the upper boundary (ν=21) production is also possible from the ν=22 level that is not simulated. In order to take into account the contribution from the higher level we estimated the N_2 X(ν=22) population by linear extrapolation in log-space. Similarly we included loss to the ν=22 level by VV collisions. These boundary conditions affect the shape of the vibrational distribution at the edge of the vibrational space.

Finally, for the a, a′, and w states we assume the intrasystem collisions:

$$a(\nu) + X \leftrightarrow a'(\nu') + X$$
$$a(\nu) + X \leftrightarrow w(\nu') + X,$$

along with the corresponding intersystem collisions. Rates for these processes are calculated based on the theoretical study of Kirillov (2011). These transitions can potentially affect the distribution of emitted radiation in the LBH band (as was found for the Earth's atmosphere by Eastes and Dentamaro, 1996), which are some of the main emission bands observed in Titan's atmosphere. Electronic quenching rates for the a′-state are taken from Cartwright (1978). The theoretical calculations also allow us to include the cross manifold collision rates due to spin-orbit interactions. However, these processes proceed much more slowly than the collisional rates within each manifold and they do not affect the results. For all other singlet states we estimate the electronic quenching rates based on other states of similar molecular symmetry. As we will see below, these estimations do not affect the results of our calculations as the radiative transitions dominate the population of the singlet states.

2.3.3. Doublet manifold

For the ion states we include the radiative transitions to the ground ion state (Gilmore et al., 1992) and recombination rates with electrons. The latter process leads to the dissociation of the molecule and the production of excited fragments. For recombination we use the rates suggested by Sheehan and St Maurice (2004) for the ν=0 or higher levels. Dilecce et al. (2010) measured the electronic quenching of the N_2^+ B(ν=0) state and we assume that the same rate applies for all levels of the excited ion states.

The ground ion state is also affected by VV and VT collisions with the ground neutral state:

$$N_2^+(\nu) + N_2(\nu = 0) \rightarrow N_2^+(\nu - \delta\nu) + N_2(\delta\nu)$$
$$N_2^+(\nu) + N_2(\nu = 0) \rightarrow N_2^+(\nu - \delta\nu) + N_2(\nu = 0),$$

while charge transfer reactions

$$N_2^+(\nu) + N_2(\nu = 0) \leftrightarrow N_2(\nu) + N_2^+(\nu = 0)$$

are also efficient. The latter reactions, however, proceed efficiently in both directions so they do not affect the vibrational distribution of the neutral and ion ground states. Theoretical and laboratory studies show that the former collisions (VV and VT) proceed with either single or multi-quantum transitions

(Kato et al., 1998; Sohlberg, 1999). In our calculations we assumed only single ($\delta\nu$=1) and double ($\delta\nu$=2) quantum transitions for the VV collisions and single quantum transitions for the VT collisions. We set the branching ratio for the single quantum transitions to 0.8 and we assumed that the branching ratio for the double quantum VV collisions is equal to that of the VT collisions, i.e. 0.1. These values are based on quantum mechanical calculations (Sohlberg, 1999), while the overall rate of the VV+VT reaction is k= 1.66×10^{-10} cm^3s^{-1} based on laboratory measurements (Kato et al., 1998).

2.3.4. Collisions with other molecules

The main species that can affect the population of the N_2 states is methane. The reactivity of ground state N_2 with CH_4 is weak, but the reactivity of higher energy states/levels could be more efficient. So far we have not found any published measurements for these processes. Studies on the reactivity of N_2 X(ν) with SiH_4 demonstrate that the reaction rate increases with vibrational level from 10^{-13} cm^3s^{-1} for ν=0 to 6×10^{-13} cm^3s^{-1} for 4<ν<13 at 300 K (Piper, 2002). A similar behavior is anticipated for methane although the absolute value of the energy exchange rates is unknown. Thus, we evaluate the role of this process by testing different rates.

Other long lived excited states can also partake in chemical reactions with methane and other hydrocarbons in Titan's atmosphere. For the N_2 A-state we also consider reactions with CH_4, C_2H_6, C_2H_2, and C_2H_4. The rates for these reactions increase as we move from an alkane to an alkyne reactant (Dutuit et al., 2013), demonstrating a transition in the reaction character from electronic/vibrational de-excitation of the excited N_2 state to collision induced dissociation of the reaction partner. For CH_4 and C_2H_6 the reaction rates were found to increase with the N_2 vibrational level involved, although quantitative information for the reaction rate is not currently available. In our calculations we assumed the measured reaction rates for the A(ν=0) case for all vibrational levels. On the contrary the vibrational dependence of the reactions with C_2H_2 and C_2H_4 is small, as these reactions lead to dissociation.

N_2 A can also transfer its energy to CO, due to the resonance of its energy levels with those of the CO a $^3\Pi$ state (Thomas et al., 1987). The rates for the energy transfer to CO vary strongly with the vibrational level of N_2 A and increase from v=0 to v=3, followed by a rapid drop at higher ν (for measurements performed at room temperature). For the reported rates, the CO/CH_4 reaction rate ratio varies from 500 for ν=0, to 15, 17, 5, and lower values for vibrational levels, 1,2,3, and higher levels, respectively (Herron, 1999). Considering that the CH_4/CO density ratio in Titan's atmosphere is ∼300, this would mean that the energy transfer rate could be important only for N_2 A(ν=0) if the ratio of the CO and CH_4 reaction rates does not significantly change with lower temperature, for which we do not have any information. On the other hand, the large radiative lifetime (∼ms, Clyne and Heaven, 1981) for the produced CO a $^3\Pi$ state in this process, implies that the produced population is dominantly lost in reactions with N_2 leading back to N_2 A, thereby results in a zero net effect. For these reasons we did not include this process in our calculations. A thorough comparison of the model results with the VK band observations from Cassini/UVIS should help us evaluate this assumption in a future study.

We also considered the reactivity of the ion ground state with methane that predominantly results in dissociative ionization of CH_4, producing CH_2^+ and CH_3^+. The rate for this reaction is measured as 1.2×10^{-9} cm^3s^{-1} (Dutuit et al., 2013) and we assumed the same rate for all vibrational levels of the ground ion state. This assumption is supported by laboratory measurements of the branching ratios of the different reaction products for $N_2^+(\nu = 0-2)$ that showed a weak dependence on the vibrational level (Xu et al., 2013). For the excited ion states other processes are faster and therefore we did not include their reaction with CH_4.

2.4. Solution method

For the calculation of the state/level populations we assume a steady state solution at each atmospheric altitude whereby we balance the production and loss rates for each state/level (s,l) taking into account its pre-dissociation probability, $f_{dis}^{s,l}$:

$$(1 - f_{dis}^{s,l})P_{s,l} = L_{s,l}. \quad (4)$$

In general the production term for each state is:

$$P = P_{h\nu} + P_e + P_{rad} + P_{col}, \quad (5)$$

where we have dropped the s,l designation for simplicity. The terms included on the RHS of equation 5 correspond to production by photon absorption, electron excitation, radiative de-excitation of a higher

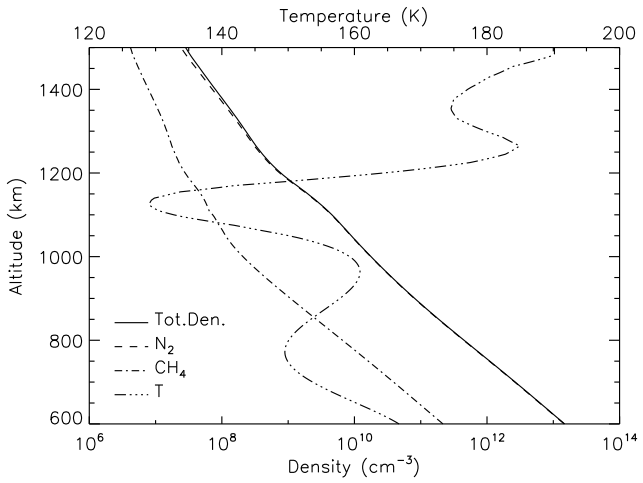

Figure 7: Atmospheric properties (temperature and density) assumed for the case study presented, corresponding to the T40 flyby conditions.

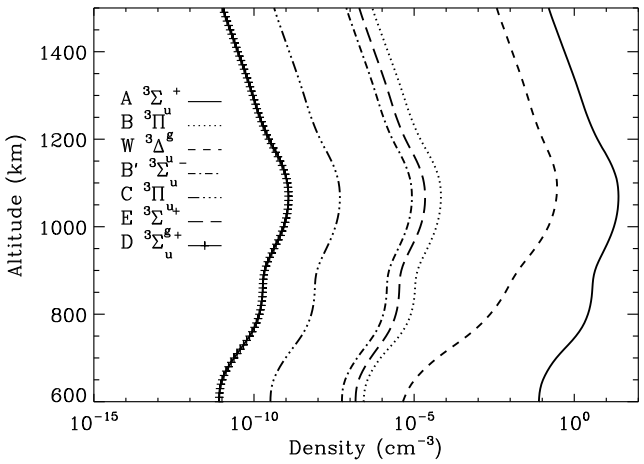

Figure 8: Vertical profiles of different triplet states. Each line corresponds to the sum of the vibrational levels of each state.

level, and production through collisions, respectively. The last term is a composite of all the collision processes discussed earlier and its calculation depends on the specific state/level considered. The corresponding loss terms are dominated by the radiative excitation and collisional terms. For the ground states of N_2 and N_2^+ we also consider the loss by electron impact excitation of the different vibrational levels.

Our 'solver' starts by assuming that all N_2 is in the ground state and proceeds by taking increasing time steps until all state/levels for all altitudes are converged within a pre-defined accuracy. For each atmospheric level and time step used we obtain the new densities for each state/level by solving the coupled system of equations with the Newton-Raphson method (Press et al., 2007). Due to the short lifetime of the excited states, the required time steps initiate with very small values (10^{-13} s) and gradually increase as the short lived state population converges. We assume that a given state/level is converged after the fractional difference in the production and loss terms is smaller than 10^{-3}. Due to the intricate way in which different states are coupled through collisions and radiative de-excitation, we noticed that some extremely short lived states can inhibit the increase in the time step due to changes made to longer lived states to which they are coupled. For this reason, once a state/level is converged we no longer consider it in the evaluation of the subsequent time steps in order to allow for a faster relaxation of the system to the global solution. Once a global solution is obtained we re-run the system with the new densities for a number of iterations to verify the global convergence.

This local balance solution is valid for all excited electronic states, but it does not suffice for the ground state balance. All excited states are balanced whence the time steps reach ∼1 second, but the ground state population requires a significantly longer time to reach equilibrium and during this elongated time it can be affected by diffusion. We include this effect in our calculations by solving the full scale continuity equation for all ground state levels taking into account molecular diffusion and atmospheric mixing. The solution method can be found in Lavvas et al. (2008), along with details for the atmospheric mixing profile we use. At the lower boundary, diffusion does not affect the abundances, thus we fix our N_2 X profiles to the solutions found with the local balance approach. At the top boundary we assume zero flux conditions (no escape). For the diffusion coefficients we assumed that all vibrational levels of the ground state have similar transport properties. In reality the excited vibrational levels can have different collision integrals since the interaction potentials for each vibrational level and the ground state is modified in each case. However, for N_2 this effect is expected to be weak (Fujimoto et al., 1976), a conclusion that is supported by measurements of CO (Margottin-Maclou et al., 1971).

3. Case study

In order to provide a detailed description of the mechanisms involved in the establishment of the vibrational population of each electronic state, we pre-

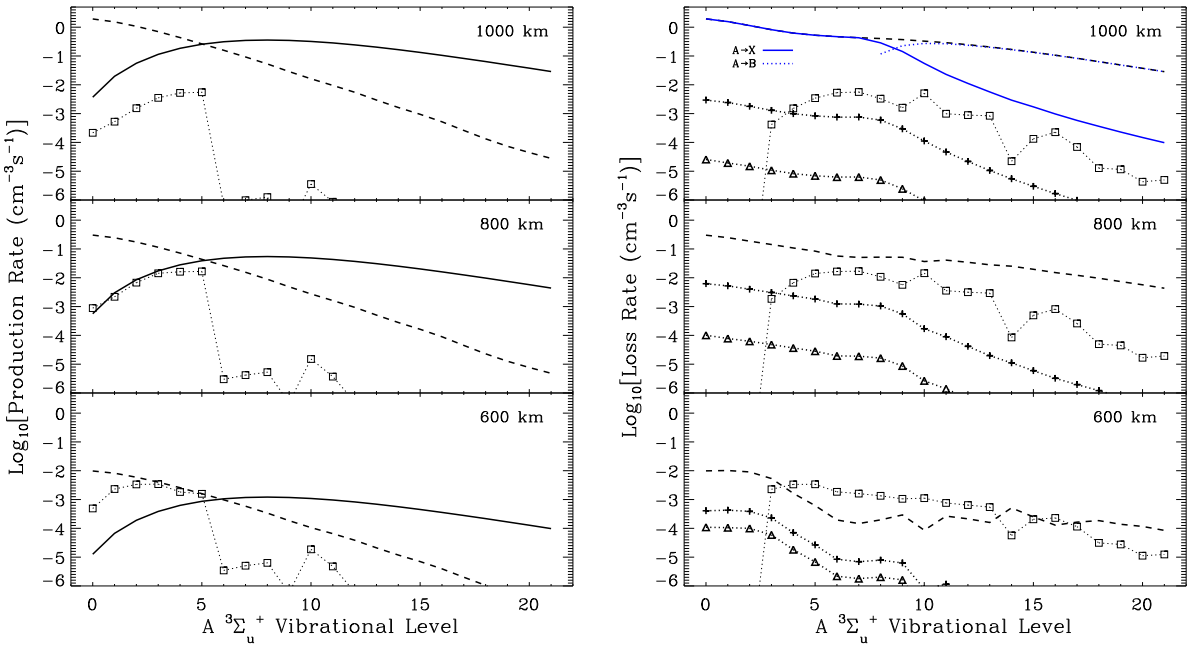

Figure 9: Production (left) and loss (right) rates for the A $^3\Sigma_u^+$ state at different vibrational levels and at three different altitudes in Titan's atmosphere. The relative contributions of the different mechanisms are shown with black lines for direct excitation (solid line), radiative de-excitation (dashed line), intersystem crossing (squares), chemical reactions (crosses), and quenching (triangles). The blue lines for the loss rates at 1000 km show the contribution of different transitions to the radiative cascade. The deeper we move into the atmosphere, the more efficient collisional processes become and therefore the more comparable to direct excitation (for production) and radiative de-excitation (for loss) they are. Note also the absolute change in magnitude for the three altitudes, that demonstrates the variation in the energy input for each location.

sent here the results of the model for a specific case of atmospheric conditions and solar illumination. For the atmospheric properties we chose the conditions observed on Titan during the T40 flyby. We derive the atmospheric properties for this flyby from the INMS observations (outbound leg, calibration factor of 2.6, see Fig. 7 and Lavvas et al., 2011) in the upper atmosphere, and we smoothly connect them to the lower atmosphere properties measured by the Huygens probe below 500 km (Aboudan et al., 2008). For the solar flux we use the measured insolation from the TIMED/SEE instrument at the time of the Cassini observations, and a high resolution spectrum from the SOHO/SUMER instrument for the spectral region of the N_2 neutral dissociation, the latter scaled to the total insolation of the former for the T40 conditions (see Lavvas et al., 2011). The T40 flyby took place on January 5, 2008, at which time the solar activity was at its minimum, with an F10.7 index of 77.1[2]. For the illumination conditions we assume a solar zenith angle of 60°, characteristic of disk average conditions. In the following section we discuss the densities and vibrational distribution of each state separating them based on their multiplicity.

3.1. Triplet states

An overview of the model results for the population of the triplet states is presented in Fig. 8, where the total density of each state is shown. Among the triplet states (and surpassed only by the population of the ground neutral and ion states) the A $^3\Sigma_u^+$ state has the highest population at all altitudes, followed by the W $^3\Delta_u$ state. All other states have significantly smaller densities ranging between 5 and 10 orders of magnitude lower than the density of the A-state. This density variation among the states reflects their different radiative lifetimes.

The A $^3\Sigma_u^+$ state is produced by direct electron impact excitation of the ground state N_2, and by cascade from higher lying states (Fig. 9). At 1000 km the cascade contribution dominates the production for vibrational levels with ν<5, and is due to the radiative de-excitation B→A (First Positive band), while the E→A (Herman-Kaplan band) transition has a minor role. Direct excitation by electron impact dominates

[2]http://omniweb.gsfc.nasa.gov/ow.html

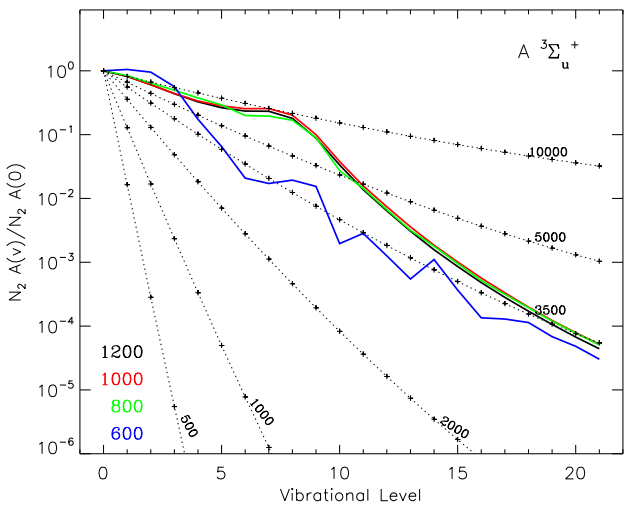

Figure 10: Vibrational distribution of the A-state at different altitudes (colored lines). Here we normalized the density of each vibrational level to the density of the ν=0 level at each altitude. The dotted lines correspond to the Boltzmann distributions at different temperatures (see numbered labels in K). The effect of collisions start to be seen as we move below 1000 km, as demonstrated by the change in the structure of the distributions.

for higher vibrational levels although the exact vibrational level for the transition between these two contributions changes with altitude. This dependence results from the decrease of the direct excitation contribution at lower altitudes, combined with the increasing role of collisions (due to the higher atmospheric density). Production by vibrational redistribution is efficient only at low vibrational levels ($\nu \leq 5$), since the rate for this process decreases rapidly for higher levels. Similarly the collisional transition from the B-state to the A-state has a negligible effect due to the low population of the B-state (see Fig. 8 and below).

A similar picture is seen for the loss rates of the A-state where at high altitudes radiative cascade dominates. At 1000 km loss of the different vibrational levels from radiative transitions to the ground state dominates for ν<9, while at higher levels the intersystem radiative transition to the lower vibrational levels of the B-state makes the major contribution. At lower altitudes contributions from the vibrational redistribution and intersystem crossing with the B-state make an increasing contribution at vibrational levels ν>3. Note that chemical reactions and direct quenching to the ground state have always a small effect in the overall loss, while energy pooling reactions have a negligible role for the population of the A(ν=0,1) levels (not shown).

The above processes have a direct reflection in the vibrational distribution of the A-state (Fig. 10). Above 1000 km the dominance of radiative processes results in smooth profiles for the vibrational distribution. At lower altitudes, as collisions become progressively more important, the distribution is modified due to the vibrational redistribution and the intersystem crossing that have a structured variation with vibrational level. The overall effect of these collisions is to increase the relative population for the low vibrational levels compared to that of higher altitudes. This result is consistent with the Morrill and Benesch (1996) study on the effect of collisions in the vibrational population of the A state in the Earth's atmosphere.

We can also compare the vibrational distribution derived, with the theoretical Boltzmann distributions at different temperatures (see dotted lines in Fig. 10). It becomes clear from this comparison that the vibration distribution of the A-state cannot be characterized by a single vibrational temperature. At and above 1000 km, vibrational levels with $\nu \leq 7$ can be approximately characterized by a Boltzmann distribution with a temperature between 5,000 and 10,000 K. At higher vibrational levels the distribution drops rapidly to lower temperatures and, at $\nu \geq 18$, approaches a vibrational temperature of $\sim$3500 K. This transition in the characteristic vibrational temperature reflects the different sources of population of the different levels, as identified above. At lower altitudes the collisions progressively decrease the vibrational temperature of the distribution and only the first few vibrational levels (ν=0-2), as well as the highest levels ($\nu \geq 18$), retain the same vibrational temperature as at high altitudes, since at these levels collisions have a minimal effect (see Fig. 9).

The production of the B $^3\Pi_g$ state is equally controlled by direct excitation and cascade, for all levels (Fig. 11). For $\nu \leq 3$ radiative cascade from the C- and the A-state dominates the production rates at 1000 km, while at higher levels the cumulative contribution of the A-, W-, and B′-states has a comparable effect to the direct electron excitation. Comparison with the loss rates of the A-state (Fig. 9) demonstrates how the intersystem radiative crossing from the higher levels of the A-state ($\nu \geq 8$) populates the lower levels of the B-state ($\nu \leq 8$). At lower altitudes collisions of the A-state with the ground state levels populate the low levels of the B-state, but with

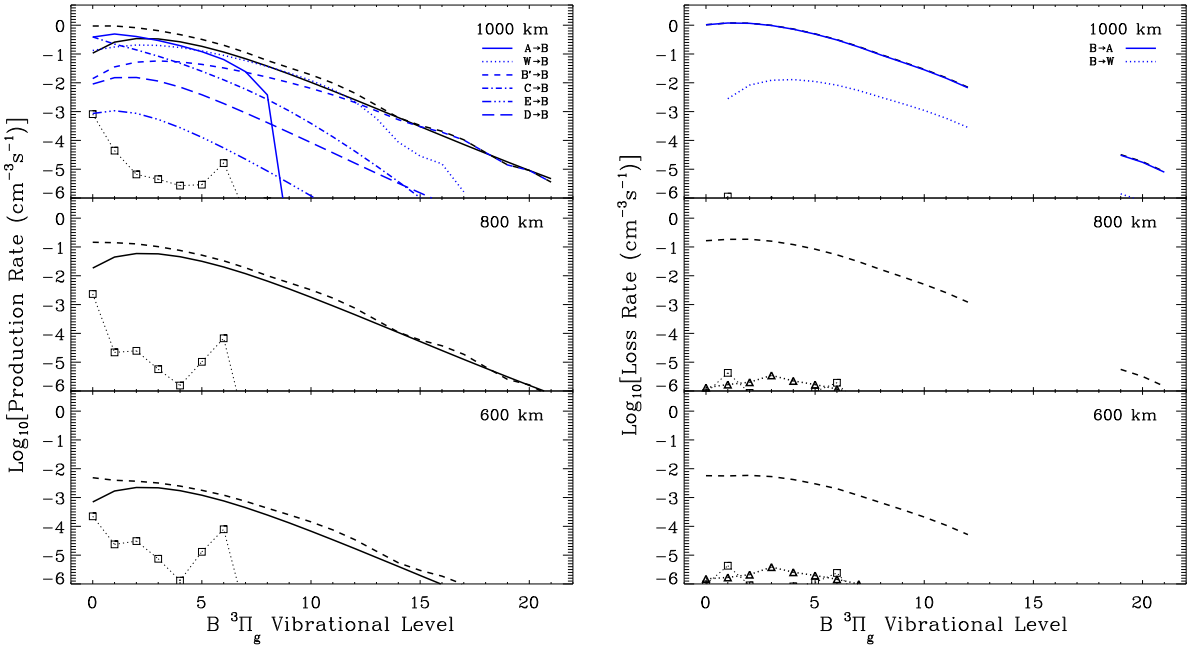

Figure 11: Same as for Fig. 9 but now for the production rates of the B $^3\Pi_g$ state. The blue lines for the rates at 1000 km present the contribution of the different states to the radiative cascade. The gap in the loss rates for vibrational levels between 13 and 18 is due to the pre-dissociation of these levels.

a minor contribution to the overall production, while energy pooling collisions of the A-state have a negligible effect. For the loss rate of the B-state levels, radiative de-excitation dominates in the three altitude regions, with the B→A transition having the most important contribution at all levels, followed by the B→W transition (Fig. 11).

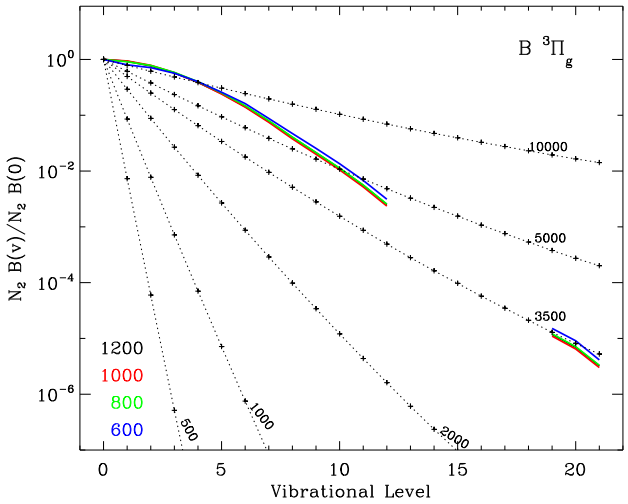

Figure 12: Same as Fig. 10 but now for the vibrational distribution of the B-state. For this case, radiative processes are far more efficient than collisional processes and the shape of the distribution does not significantly change with altitude.

Due to the small contribution of collisional processes in the production and loss rates, the vibrational distribution of the B-state does not significantly change with altitude (Fig. 12). As with the A-state, the overall shape of the vibrational distribution cannot be characterized by a single vibrational temperature. The more efficient population of the low vibrational levels from the radiative cascade of the A-state is characteristic of a higher effective temperature (∼10,000 K) relative to the slower production through the radiative cascade from the B′-state, that dominates at high vibrational levels and where a lower effective vibrational temperature (∼3,500 K) is more consistent with the distribution.

The production of W $^3\Delta_u$ is dominated by direct electron excitation at all three altitude regions (Fig. 13). Only for the first three vibrational levels ($\nu \leq 2$) does production from the de-excitation of the higher B-levels contribute significantly to the production rates. Moreover, collisions do not substantially affect the production rates of this state and only make a small contribution close to 600 km for the low levels. Similarly the loss rates are controlled by the radiative cascade to the B-state for all altitudes, with the exception of the first vibrational level which has a long radiative lifetime. For this case, quenching to the

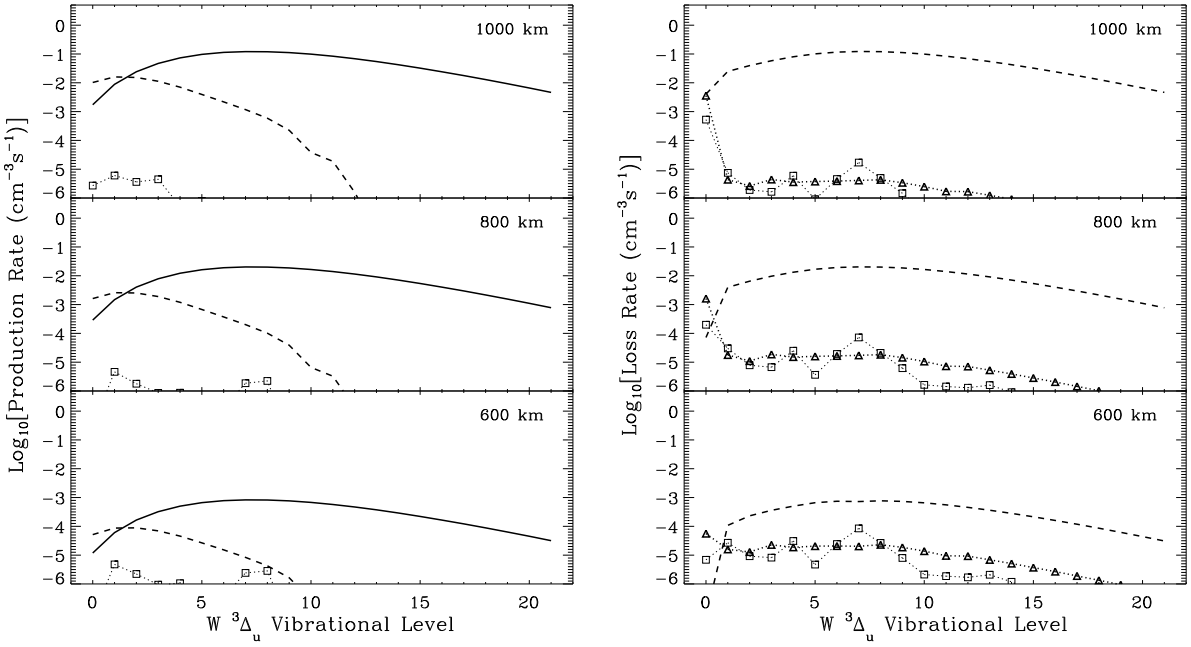

Figure 13: Same as for Fig. 9 but now for the W state.

ground state controls the loss rate, with collisional coupling to the B-state having a secondary role.

The vibrational distribution of the W-state has the same shape for $\nu \geq 1$ for all altitudes since radiative processes dominate at these levels. As collisions control the lifetime of the lower levels, the relative population between these two regions (i.e. the population for ν=0 and the population for $\nu \geq 1$) decreases with decreasing altitude. Therefore, the normalized distribution at $\nu \geq 1$ shifts to higher values as the relative population of the ν=0 level decreases with decreasing altitude (Fig. 14). Our results demonstrate that even at 1000 km there are enough collisions to affect the W(ν=0) population. This conclusion is ev-

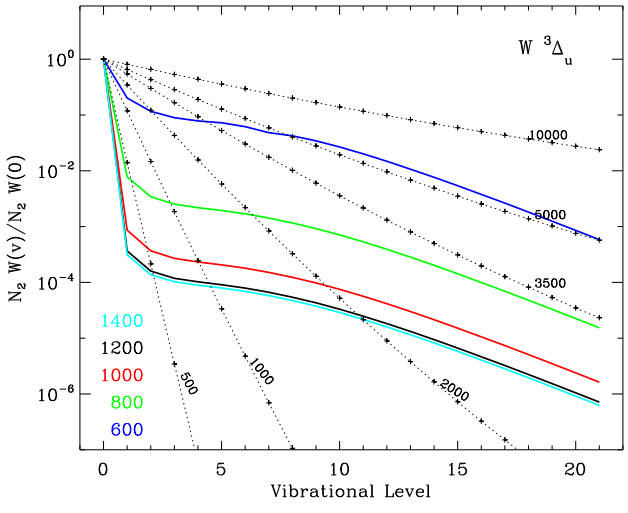

Figure 14: Vibrational distribution of the W-state normalized to the ν=0 level. The different colors correspond to different altitudes. The dotted lines are Boltzmann distributions at the presented temperatures. For this state collisions become important below 1200 km and result in a gradual shift of the distribution for ν>2 to higher values (see text).

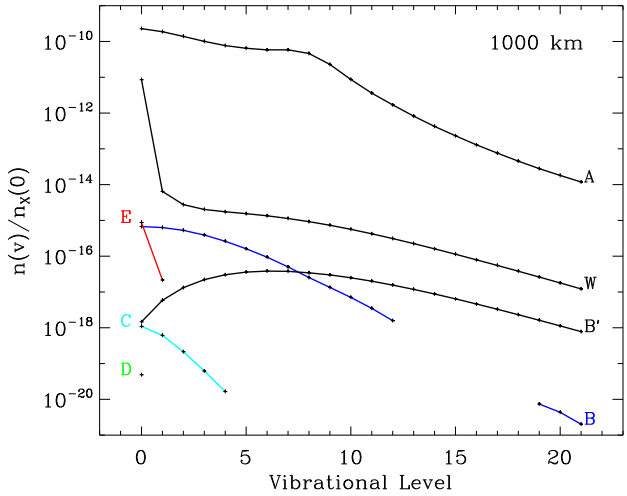

Figure 15: Vibrational distribution of the triplet states at 1000 km. Here we present the density of each state/level relative to the ground state (ν=0 level) density.

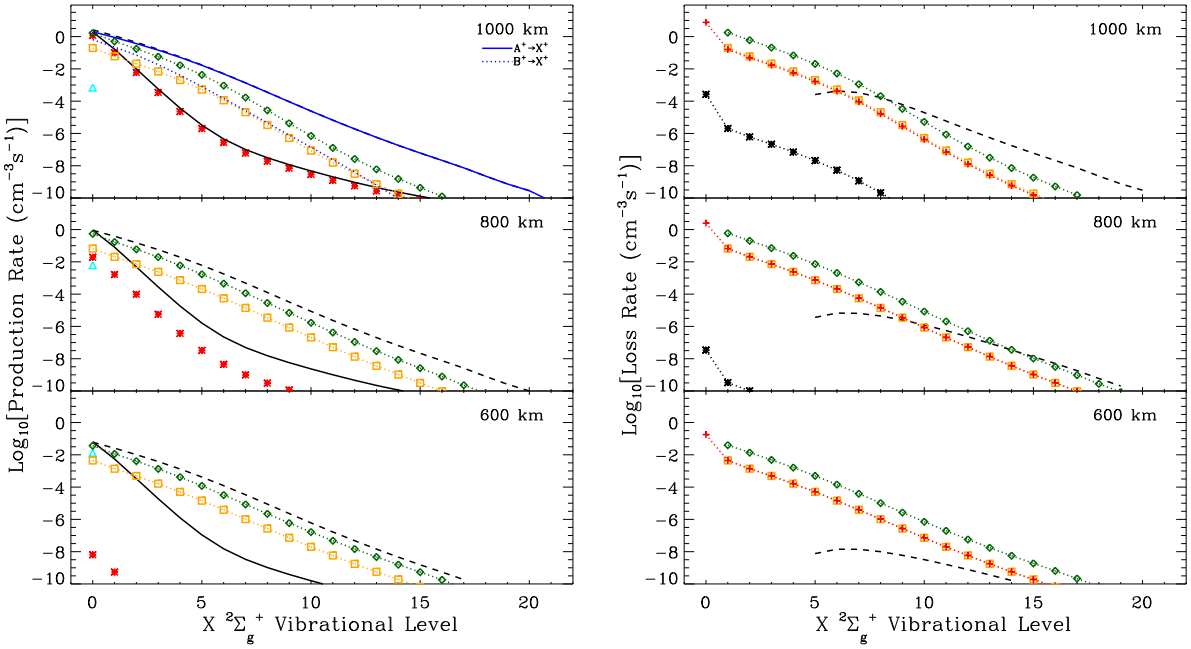

Figure 16: Production and loss rates for the ground ion state. The solid black lines represent production by electron impact excitation and the red asterisks excitation by photon absorption. The dashed lines present production or loss by radiative cascade, and the blue colored lines designate the contribution in this cascade of the different states described in the plot (only for the 1000 km production panel). Green diamonds and orange squares represent the contribution of VV and VT ion collisions and the cyan triangles for the ν=0 level for production, represent the contribution of quenching of higher electronic state ions. Chemical quenching rates (i.e. reaction with CH_4) are shown with red pluses and recombination rates with black asterisks.

ident when the distributions at 1000 and 1200 km are compared. At even higher altitudes, the effect is minimal as demonstrated by the closer agreement of the distributions between 1200 and 1400 km.

The other triplet states have a more simple behavior. For the B′-state radiative lifetimes are very small, therefore collisional processes are ineffective for all three altitude ranges. Direct excitation and radiative transitions to the B-state dominate the rates for all vibrational levels. For the C-state, levels with $\nu \geq 5$ are pre-dissociated, and for the lower levels direct excitation dominates the production as the resulting population of the higher lying E-state is too small to have an important contribution through radiative cascade. Vibrational redistribution within the C-state levels, energy pooling from the A-state and quenching to the ground state have small contributions for all vibrational levels. Similarly, for the E-state levels that do not pre-dissociate (ν=0,1) direct excitation and radiative cascade dominate the production and loss rates, respectively. The only collisional process considered for this state (quenching) has a negligible role for the loss rates, and radiative cascade from the C-state does not affect its production. The same picture holds for the D(ν=0) level, which is the only vibrational level that does not pre-dissociate for this state. Thus, all these states (B′,C,D,E) are not affected by collisions in the pressure range under investigation.

The dominance of radiative processes in the rates of these states implies that their vibrational distributions do not change with altitude, which is confirmed by our calculations. Therefore we present in Fig. 15 the distributions at 1000 km altitude of the B′-, C-, D-, and E-states along with the distributions of the other triplet states discussed earlier, normalized to the total N_2 density. In this way, the absolute abundance and the vibrational distribution of each state is clear. The shape of the B′-state distribution is markedly different from the previous cases as the ν=0 level has a lower density than higher levels of this state. This characteristically non-Boltzmann distribution results from FC factors for direct excitation from the ground state that favor transitions to vibrational levels between ν=5 and ν=10 rather than adjacent levels. Similarly, the remaining triplet states have distributions that are defined by the FC factors for the direct excitation through electron impact.

3.2. Doublet states

The ground ion state, X $^2\Sigma_g^+$, is predominantly produced through the radiative de-excitation of the higher ion states at all vibrational levels, with the exception of the ν=0 level for which the FC factors from the ground neutral state have significant values and excitation by electron impact (solid line) and photons (red asterisks) become important (Fig. 16). Among the excited ion states, A $^2\Pi_u$ provides the major contribution to the cascade, while the B $^2\Sigma_u^+$ state has a significant contribution only at low vibrational levels. Quenching to the ground ion state also provides an increasing contribution with decreasing altitude to the population of the ν=0 level (cyan triangles in Fig. 16). At 1000 km excitation by photons and electrons have similar magnitudes, but at lower altitudes photon population with the required energy is strongly reduced and electron excitation remains the only direct ionization process. Note also the sharp decrease in the rates with increasing vibrational levels relative to the previous states discussed. In practice only the low levels ($\nu \leq 5$) have significant production rates that eventually lead to significant populations, as we will see below.

The loss rates for the X $^2\Sigma_g^+$ state depend strongly on the vibrational level considered. For all altitudes the ν=0 level is primarily lost by chemical reaction with CH_4 that predominantly produces CH_3^+ or CH_2^+, and by recombination leading to dissociation. For higher levels, loss is due to VV and VT collisions with the ground state population, while radiative de-excitation to the low levels of the A $^2\Pi_u$ state contributes only for $\nu \geq 5$. At 1000 km the transition between the latter two processes occurs at ν=7, but as density increases at lower altitudes quenching becomes progressively more efficient and the transition occurs at higher levels (Fig. 16). Chemical loss for the ν>0 vibrational levels follows the same altitude behavior as with the collisional rates with N_2, and has a similar magnitude to the VT rates.

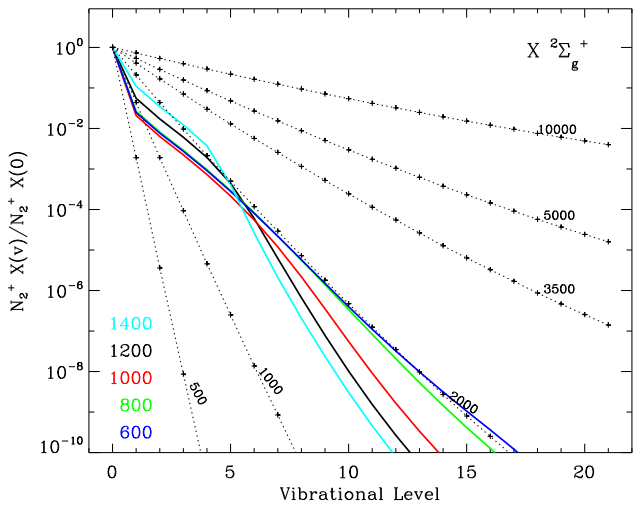

Figure 17: Vibrational distribution of the ground ion state normalized to the ν=0 level. The different colors correspond to different altitudes. The dotted lines are Boltzmann distributions at the presented temperatures.

The resulting vibrational distribution of the ground ion state demonstrates a rapid drop with increasing vibrational level, with a small shoulder for ν=1-4 (Fig. 17). This feature is caused by the different loss processes affecting the vibrational levels. The chemical loss of the ν=0 level, which dominates the loss processes of this level, proceeds with a reaction rate that we assume is the same for all vibrational levels. For higher levels, where other loss processes have important contributions increasing the total loss rate, a smaller vibrational population is required to balance the production rate. Therefore, the resulting density for ν=1 is significantly smaller than the density for ν=0. The small shoulder for ν = 1-4 occurs because of the corresponding behavior of the production rates of these vibrational levels, while the rapid drop of the production at higher levels causes the drop in the distribution.

For the other two ion states the picture is simpler. Excitation occurs predominantly due to direct ionization by photons and electrons with a similar altitude variation as for the ground ion state, while intra-system radiative transitions from the ground state have a negligible contribution to the total production of these states. Radiative cascade to the ground ion state dominates the loss rates, with quenching and recombination providing minor contributions. Thus, although we assumed the same recombination rates for the excited ion states as for the ground ion state this assumption is not affecting our conclusions since the actual recombination rates should be even lower for the excited ions. As their production and loss rates are dominated by radiative processes, their distributions do not vary with altitude. An overview for the density profiles of the doublet states and their vibrational distribution at 1000 km is provided in Fig. 18. The first excited ion state (A $^2\Pi_u$) has a broad vibrational distribution as all of its levels are significantly populated. On the contrary the second ion

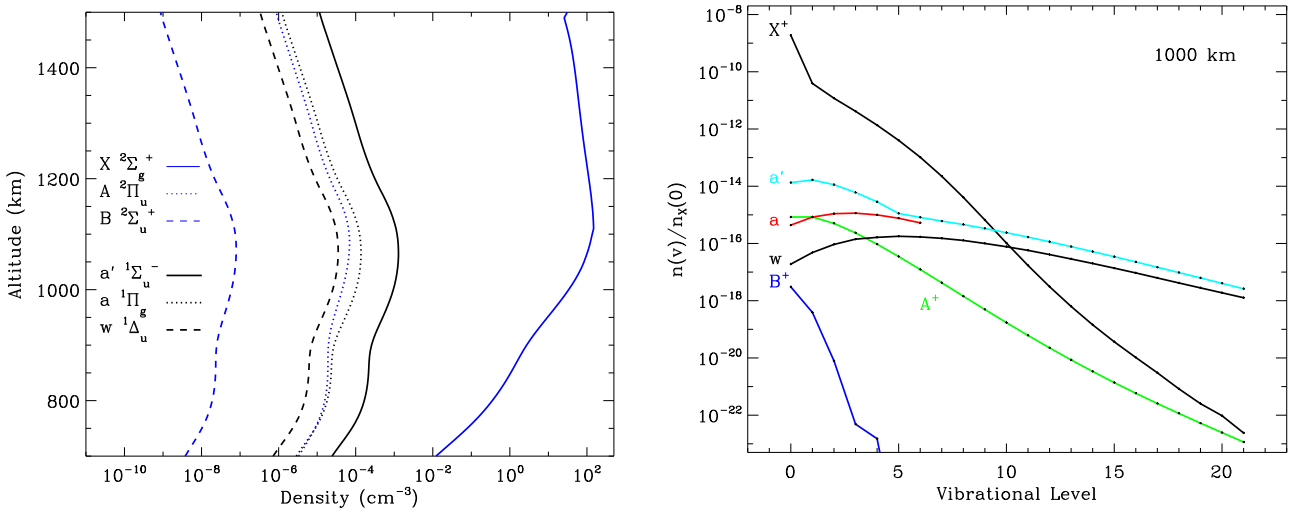

Figure 18: Left: Density profiles of neutral singlet and ionic doublet states summed over their vibrational population. Right: Vibrational distributions of singlet and doublet states at 1000 km altitude. All populations are normalized to the ground state population.

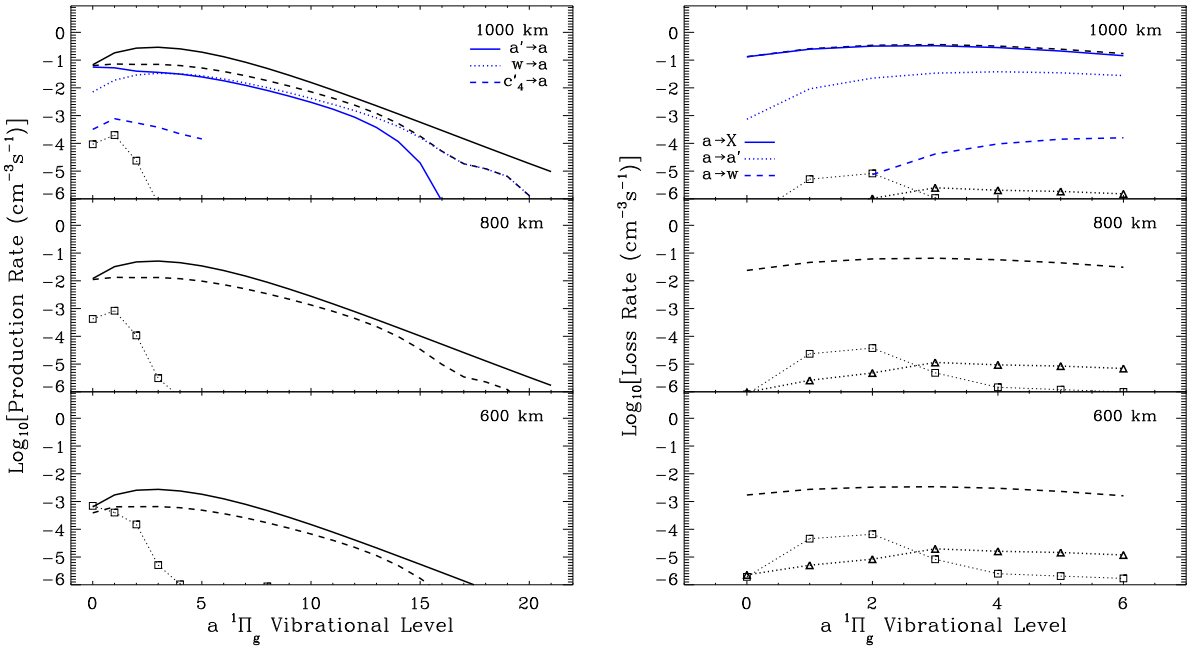

Figure 19: Production and loss rates for the a $^1\Pi_g$ state at different vibrational levels and at three different altitudes in Titan's atmosphere. The relative contributions of different mechanisms are shown with black lines for direct excitation (solid line), radiative de-excitation (dashed line), intersystem crossing collisions (squares), and quenching (triangles). The blue lines for the loss rates at 1000 km show the contribution of different transitions to the radiative cascade. Loss rates for $\nu \geq 7$ are zero due to pre-dissociation of these levels.

state (B $^2\Sigma_u^+$) has a much more narrow distribution as only for the lower levels the FC factors for direct excitation from the the ground state have significant values. Finally, due to the higher photon and electron energies required for the excitation of the B $^2\Sigma_u^+$ state, its overall population is significantly smaller than the population of the A $^2\Pi_u$ state.

3.3. Singlet states

An overview of the density and distribution of the first three singlet states (a, a′, and w) is provided in Fig. 18. Our calculations show that these singlet states have the highest density, since the population of the other singlet states is strongly reduced by predissociation.

The first three singlet states demonstrate a rather collisionless behavior in the altitude range of interest. At 1000 km the a-state is mainly produced by direct excitation, while transitions from the a′- and w-states dominate the radiative cascade (Fig. 19). The ratio between these two terms remains roughly the same at lower altitudes and the total production is only affected by collisions (inter-system crossing), close to 600 km and at low vibrational levels from coupling to the a′- and w-states. Similarly, the loss rates for the a-state are dominated by the radiative cascade (primarily to the ground state, generating the LBH emission) and collisions are unimportant down to 600 km. As a result, the vibrational distribution of the a-state does not change significantly with altitude and follows a monotonic decrease for ν>3 (note that levels with $\nu\geq$7 pre-dissociate). The local maximum in the distribution at ν=3 results from the preferential population of levels around this value from direct excitation (see Fig. 19).

A similar picture applies to the a′-state case, but we note the differential role that radiative cascade has on the loss rate of the different vibrational levels: only the first 3 levels of a′-state are efficiently lost to the ground state, while all higher levels de-excite to the a-state (Fig. 20). The same effect holds for the radiative de-excitation of the w-state, where only the first two levels of this state efficiently de-excite to the ground state, and all higher levels proceed predominantly to the a-state (not shown). The reason for the preferential transition to different states, depending on the vibrational levels, is the variable overlap of the wavefunctions for different levels that results in different FC factors. For small vibrational levels of the a′- and w-states, the overlap with the ground state levels is large but rapidly decreases with increasing ν. On the contrary, the coupling with the a-state levels is small for small ν levels of the a′- and w-states and increases for larger vibrational levels. Thus, although the a′- and w-states emit in the IR, much of their energy is diffused to the a-state, in this way enhancing the LBH emission at UV wavelengths.

Collisions for both a′- and w-states have a small effect above 600 km. The low temperature conditions in Titan's atmosphere make the collisional processes among these states inefficient, contrary to what is observed in Earth's atmosphere (Eastes and Dentamaro, 1996). Therefore, the vibrational distributions at 1000 km (see Fig. 18) are similar in the whole simulated atmosphere. Both states have a similar distribution at high vibrational levels, but diverge for ν<10. This difference is induced by the different FC factors of the two states during direct excitation from the ground state, with the a′-state having high population close to ν=1 and the w-state population peaking close to ν=5.

The other singlet states we consider in our study (b, b′, c_3, o_3, c_4', e, e′) are strongly pre-dissociated. These states can be directly excited by photons, as well as by photoelectrons, and our calculations demonstrate that both energy sources are important for their overall population (Fig. 21). Due to the struc-

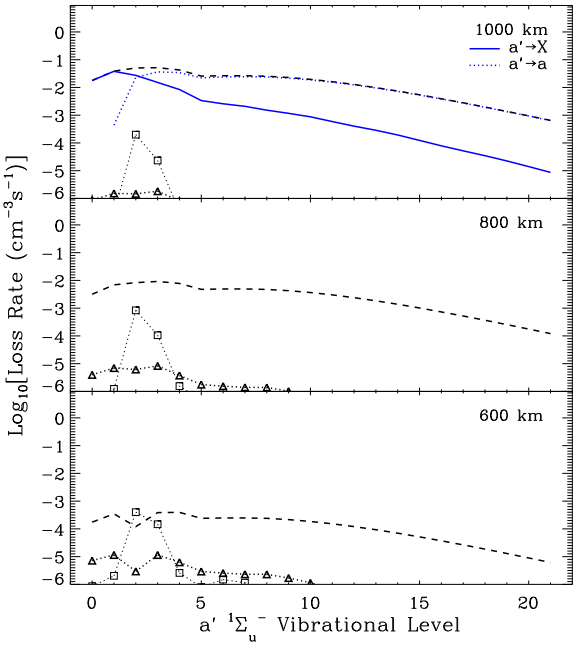

Figure 20: Same as for Fig. 19 but for the loss rates of the a′-state.

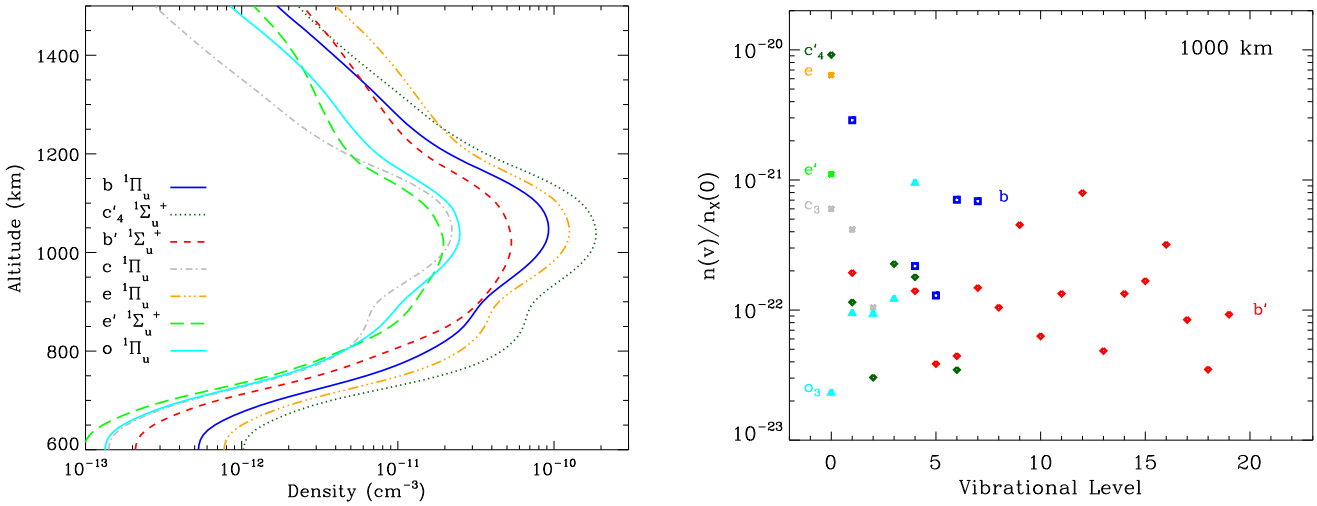

Figure 22: Left: Density profiles of the higher energy singlet states (b, b′, c$_3$, c′$_4$, e, e′, and o$_3$) summed over their vibrational population. Right: Vibrational distributions of these states at 1000 km altitude. All populations are normalized to the ground state population.

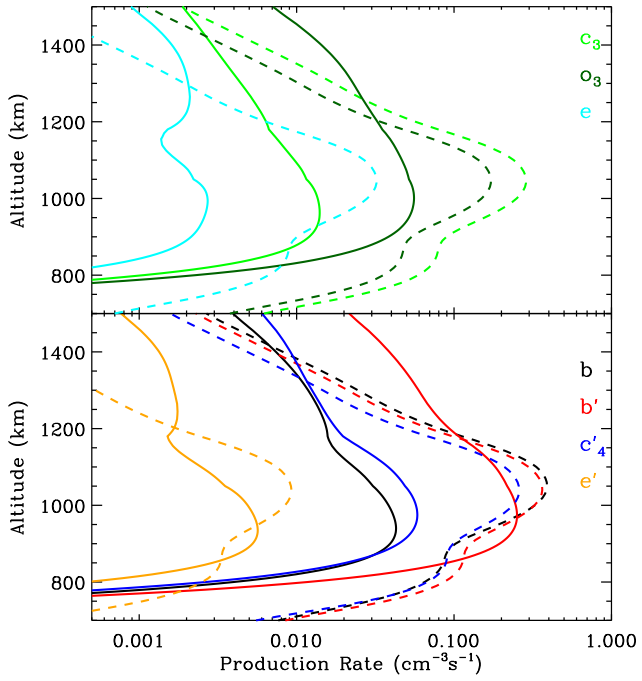

Figure 21: Comparison between production rates by photons (solid lines) and photoelectrons (dashed lines) for the singlet states: b (black), b′(red), c$_3$ (green), o$_3$ (dark green), c′$_4$(blue), e (cyan) and e′ (orange). Each line corresponds to excitation of all vibrational levels of each state that do not completely pre-dissociate.

ture of the absorption cross section between 80 and 100 nm, photons can penetrate deep into Titan's thermosphere and deposit their energy close to 900 km (Lavvas et al., 2011). This picture is reproduced here for the individual excitation profile of each singlet state, although the vertical structure and magnitude for each state reflects the relative cross section magnitude and spectral distribution of each case, convoluted with the solar spectrum. The corresponding production rates by photoelectrons peak close to 1050 km, as at this altitude most of the ionizing UV radiation generating the primary photoelectrons is deposited, followed by a secondary production peak close to 800 km due to the deeper penetration of X-rays (Lavvas et al., 2011). The relative contribution of each energy source varies with each state: for the b′- and e′-states photons and photoelectrons have comparable contributions, while for the other singlet states photoelectron excitation dominates for altitudes below ∼1200 km. At higher altitudes photons provide the major contribution for all states, hence the use of the LED approximation for the electrons does not affect significantly the accuracy of our calculations for these singlet states.

Population loss of excited singlet states is dominated by radiative de-excitation. Their relatively low (compared to the other states) excitation rate, combined with fast de-excitation and strong pre-dissociation, results in these states having the lowest densities among the simulated states (Fig. 22). Nevertheless, emission from these states makes the highest contribution to Titan's EUV airglow (Ajello et al.,

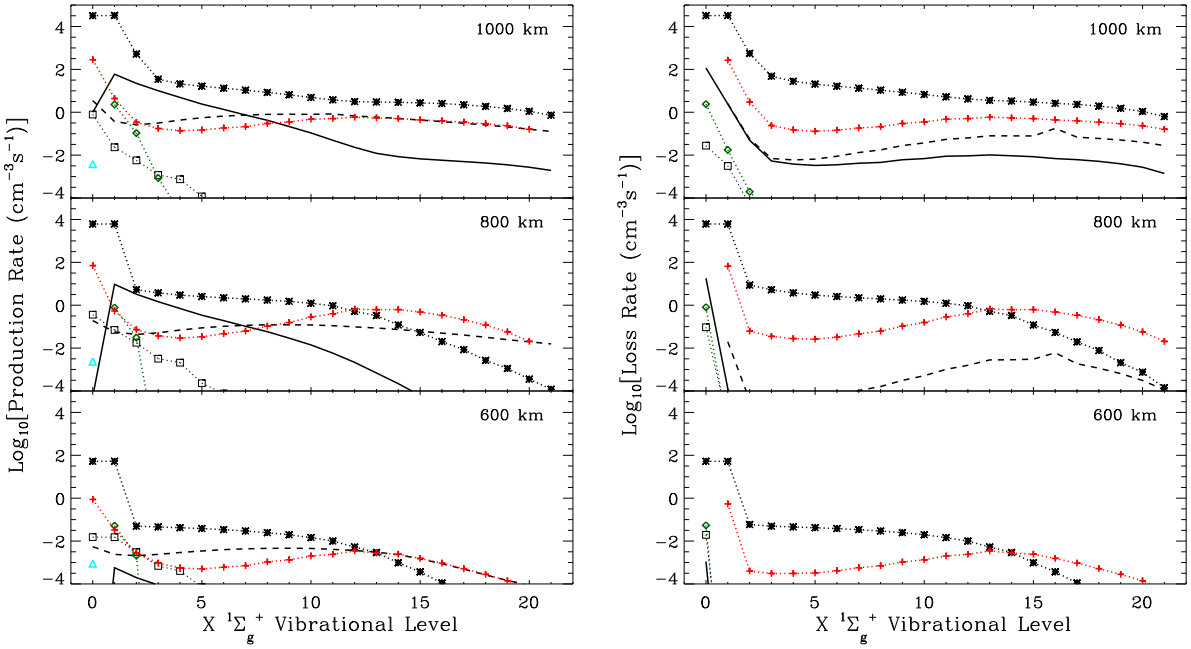

Figure 23: Production and loss processes for the ground state vibrational population at three different characteristic altitudes in Titan's atmosphere. Black lines show production rates by direct electron excitation (solid) and radiative cascade from higher laying states (dashed). Rates for energy pooling reactions that generate ground state molecules are very small and are not shown. The black asterisks represent the VV rates, while the VT rates are many orders of magnitude smaller and not shown. The red crosses show the rates for reaction with CH_4. The black squares represent the rates for the inter/intra system collision processes and the green diamonds the contribution from the VV and VT rates from collisions with the ion ground state. The cyan triangle represents the rate for quenching to the ground level from all other states.

2008; Stevens et al., 2011; Heays et al., 2014).

3.4. The ground state

The ground state population is affected by all the other states, thus we discuss it here separately. First we should note that for the ground state two types of processes are at play: on the one hand there are the production and loss rates that transfer molecules to/from the ground state from/to other electronic states, and on the other hand there are the processes that redistribute the vibrational population within the ground state. A similar distinction can be made for a few of the other states as we saw earlier (e.g. for the A-state and the ground ion state), but for the case of the neutral ground state these two different mechanisms have significantly different efficiencies.

The vibrational population of the N_2 ground state is produced by direct electron impact excitation, and by cascade from higher lying states (Fig. 23). The major cascade contribution happens for vibrational levels v>7, while for lower vibrational levels direct excitation has a predominant contribution (except for ν=0). All other collisional processes of higher energy states that result in production of ground state molecules have a minor role in the overall production rates. On the other hand, among the redistribution processes the VV collisions are far more efficient than all other processes and dominate the total production rate at 1000 km. The VV rates depend quadratically on the vibrational population, thus they decrease rapidly with decreasing altitude as the overall population of the excited vibrational levels of the ground state decreases (see below and Fig. 24). At the same time the increasing total density with lower altitudes enhances the chemical quenching of the vibrational levels by CH_4, which dominates for ν>12 over the VV rates. The same description applies for the loss rates too, with the VV rates dominating the redistribution of the vibrational levels at high altitudes, and the chemical reaction with CH_4 increasing its efficiency with decreasing altitude. Finally, due to the lower temperature conditions, the VT rates are more than four orders of magnitude weaker than the corresponding VV rate for each level, thus they do not affect the vibrational distribution of the ground state. Note that, for the loss processes, the electron impact loss and radiative cascade also effectively redistribute

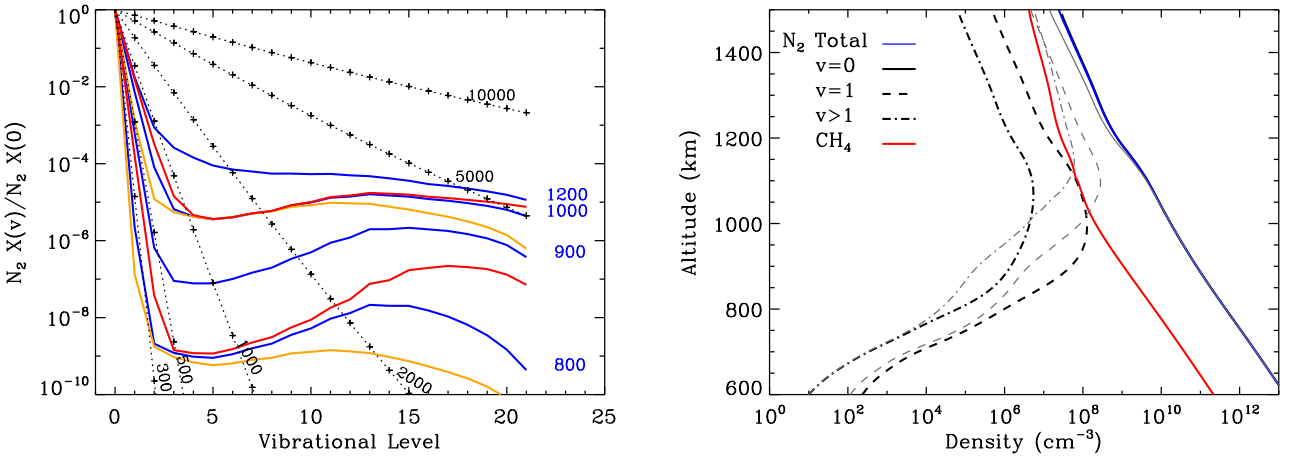

Figure 24: Overview for the vibrational distribution and density of the ground state levels. Left: Vibrational distribution of the ground state population at different altitudes (blue lines and numbers). The black crosses represent the anticipated Boltzmann distributions at different temperatures (black numbers). The orange and red lines represent the sensitivity of the 800 and 1000 km distributions on the vibrational energy exchange rate with methane for $k_{CH4} = 10^{-13}$ cm^3s^{-1} (orange) and $k_{CH4} = 10^{-15}$ cm^3s^{-1} (red) relative to the nominal case used ($k_{CH4} = 10^{-14}$ cm^3s^{-1} for the blue lines). Right: Density profiles for the ν=0, 1, and ν >1 vibrational levels for the nominal case compared with the total N_2 (blue) and CH_4 (red) density profiles. The thin gray lines represent the same results, but in the case that diffusion is not included in the calculations.

the vibrational population within the ground state for levels above the ground level. Thus, we see that although the vibrational population of the ground state depends on the rate of cascade from higher states, the actual shape of the vibrational distribution will be dominated by the far more efficient VV rates at high altitudes and the energy transfer to methane at lower altitudes.

Our resulting vibrational distributions reflect these processes (Fig. 24). At high altitudes (∼1200 km) the VV transitions dominate and the distribution is monotonically decreasing with increasing level. As we move deeper, the efficiency of the VV collisions decreases while the reaction with methane becomes progressively more important. Thus, a local minimum appears in the distributions that separates the local production by direct excitation (low ν) from the production by cascade of higher states (high ν). Finally, the total population of excited levels decreases rapidly below 900 km as reaction with CH_4 efficiently de-excites all levels.

It is also important to demonstrate the role of diffusion in the vertical profiles of the different levels. If diffusion is not included in the calculations, the peak densities for the different levels are above 1100 km and the slope of the profiles is not consistent with the total density slope (Fig. 24). Diffusion redistributes all molecules, lowering the peak density altitude and providing a slope above the peak that is consistent with the observed atmospheric density.

We turn our attention now to the reaction rate for the vibrational energy exchange between N_2 and CH_4, which as we saw has an important role in the resulting vibrational population. So far we assumed that this reaction rate is the same and equal to $k_{CH_4}=10^{-14}$ cm^3s^{-1} for all vibrational levels of the ground state.

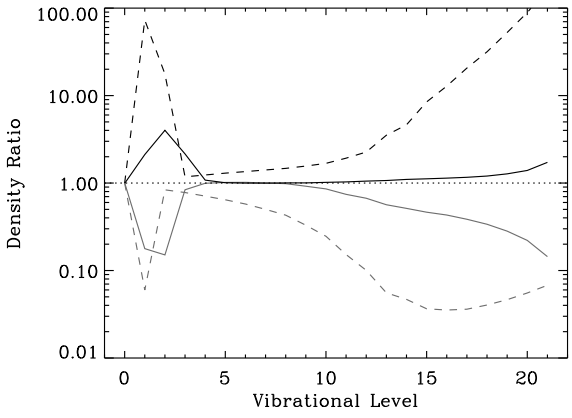

Figure 25: Sensitivity of the model ground state vibrational distribution to the reaction rate with methane. Each line presents the density ratio of a sensitivity test to the nominal density. The solid lines present results for 1000 km and the dashed lines for 800 km altitude. The black and gray lines correspond to a 10× slower and faster than the nominal rates, respectively.

This value is an estimate from a similar reaction of vibrational energy transfer between CO(ν=1) and CH_4 at room temperature (Stephenson and Mosburg, 1974). In order to evaluate the sensitivity of the model results to different reaction rates, we also performed calculations assuming 10 times faster and slower energy transfer rates (Fig. 24). The results of this test demonstrate that the variation in the rate predominantly affects the levels with $\nu \leq 2$ and $\nu > 10$, leading to a reduction of the population of excited molecules with increasing rate. For the X(ν=1) level the nominal abundance of 1.3×10^8 cm^{-3} at 1000 km is reduced to 2.3×10^7 cm^{-3} for the faster rate and is increased to 2.7×10^8 cm^{-3} for the reduced rate (Fig. 25). These changes depend strongly on the vibrational level considered and they magnify as we move deeper in the atmosphere, since the role of methane becomes more significant there. In reality, the reaction rate could change for each vibrational level as it is observed for other cases such as the reaction $N_2(\nu)$ + SiH_4 (Piper, 2002). Given the lack of any information for the reaction with methane our sensitivity test should bracket the total range of rate values anticipated for the different levels. As we will demonstrate below, the Cassini observations can help us put further constraints on the magnitude of the rate.

Notwithstanding the current limitations in our understanding of the vibrational energy exchange between N_2 and methane (and possibly other species as we discuss below), we note that this process does not significantly modify our results above 1000 km altitude. Thus, we can conclude that a significant population of vibrationally excited molecules survives in Titan's upper atmosphere. Our results demonstrate that at 1000 km, the density of the ν=1 level is comparable to the density of methane, while the total density of all higher levels is ~30 times lower (Fig. 24). For comparison the anticipated populations of these levels under thermal conditions would be more than 8 and 16 orders of magnitude lower, respectively. Such a high population of hot molecules can have significant implications in the atmospheric processes, which we discuss further in Sections 4-7.

4. Local emissions

Photons emitted during the de-excitation of the different N_2 states have wavelengths that cover a large part of the spectrum, from the UV to the near IR. These emissions are local, and depending on their wavelength, they will be attenuated by the atmosphere to different degrees. Here we discuss the relative contribution of the different states to the total local emission and how this contribution changes with altitude. Emissions in the EUV can result in re-excitation of the ground state (optically thick emissions), further complicating the resulting emission spectrum outside the atmosphere. This issue is discussed in Section 5. Higher energy N_2 states that completely dissociate into nitrogen fragments can also contribute to the airglow when their fragments are produced in excited states. This is particularly important for the N_2^+ H state that dissociates into excited atoms and ions whose emission contributes to the EUV and FUV radiation observed from Titan's upper atmosphere (Strobel et al., 1991; Bishop and Feldman, 2003; Stevens et al., 2011).

If we add all the photons emitted from each band we can compare the relative strength of emission from each electronic state (Fig. 26). Among the singlet states the strongest emission is from the LBH band ($a \rightarrow$X) followed by emissions from the Carroll-Yoshino ($c_4' \rightarrow$X) and the (w$\rightarrow$X) bands. From the higher energy singlet states the strongest emissions occur from the de-excitation of the b- and b$'$-states, although these emissions are almost 100 times smaller than the emission from the LBH band. For the ion states, the major emission from the Meinel band ($A^+ \rightarrow X^+$) is one of the strongest emissions in the atmosphere, followed by the 1^{st} negative system ($B^+ \rightarrow X^+$), while the intersystem crossing from the ground ion state to the first excited ion state ($X^+ \rightarrow A^+$) has a minor contribution. Emission from triplet states is dominated by the Vegard-Kaplan (A$\rightarrow$X) and 1^{st} positive (B$\rightarrow$A) bands. These emissions are roughly 10 times larger than the LBH and Meinel band emissions, and thus make the major contribution over the whole spectrum in terms of photons. Our emissions for the LBH and VK bands are consistent with those calculated by Stevens et al. (2011), although the absolute magnitudes are different due to differences in the insolation and atmospheric structure assumed in the two studies.

The spectral distribution, i.e. the energy content of each emitting band, changes depending on the state type. Since the dominant emissions from the singlet states occur in transitions to the ground state, their photon energy falls in the UV part of the spectrum (see Figs. 27 & 28). In addition, since the energy levels of the high singlets are very close, their pho-

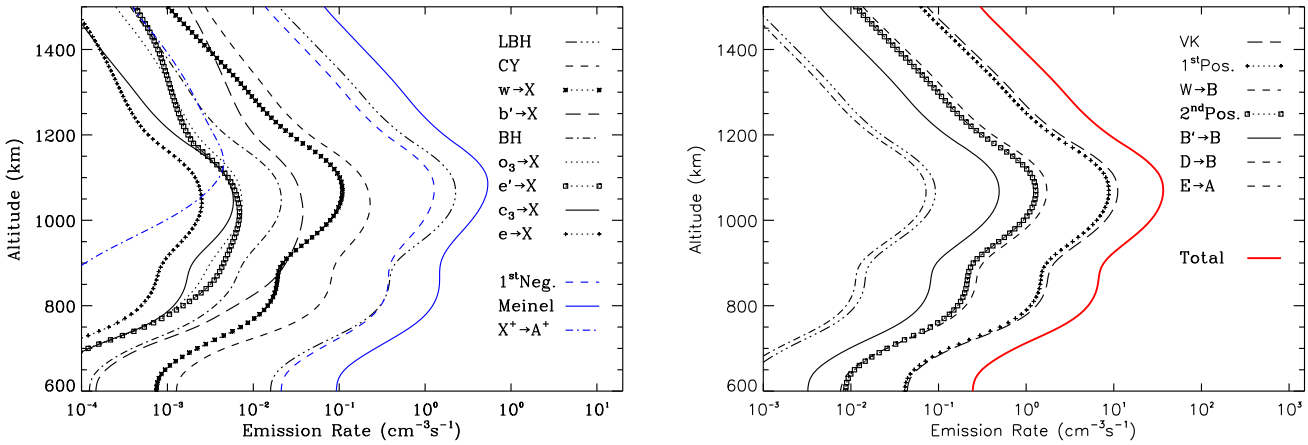

Figure 26: Local emission profiles from the major bands of the different electronic states we consider in our calculations. The red line represents the cumulative emission rate from all states.

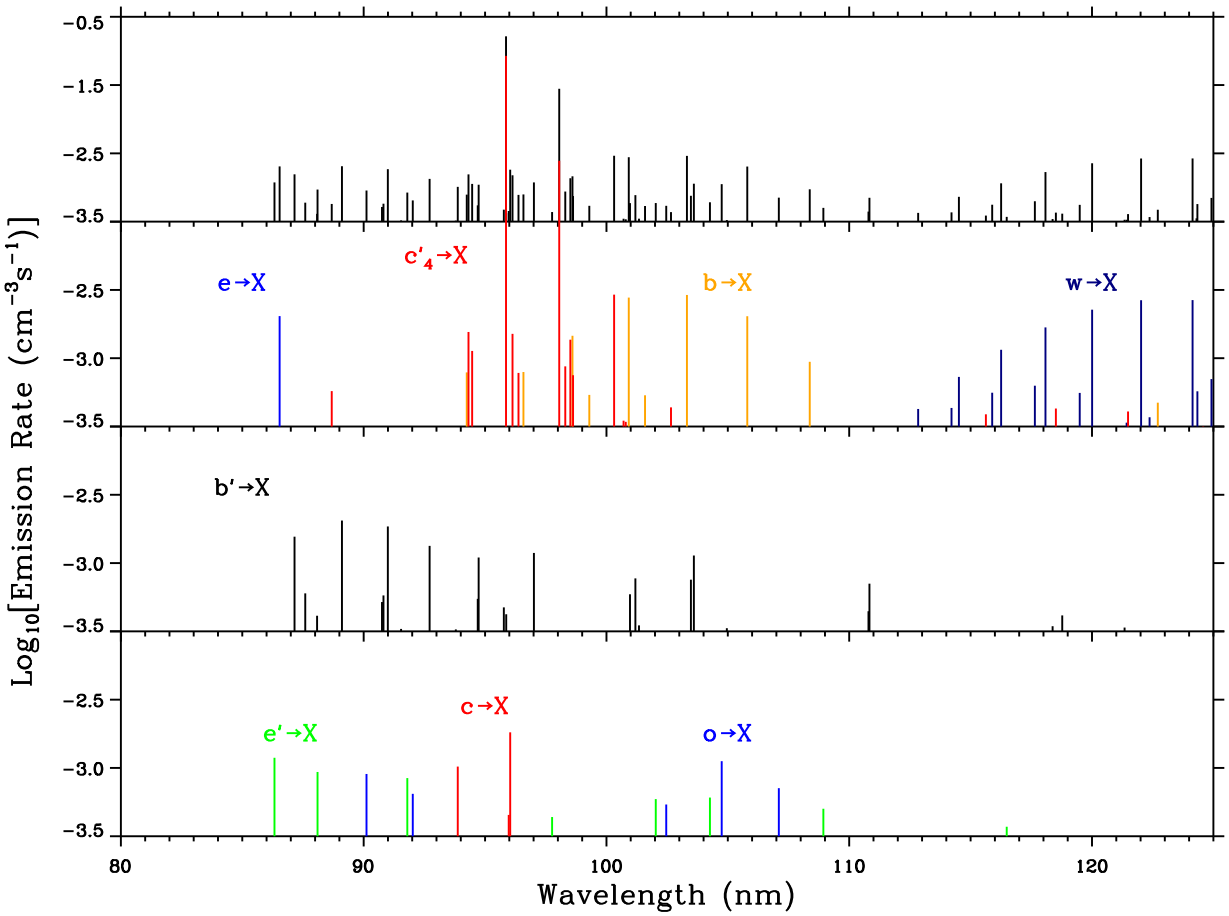

Figure 27: Local emission spectrum in the EUV from excited N_2 states at 1000 km altitude. The top panel presents the cumulative spectrum and the lower panels present the contributions of the different bands. In this part of the spectrum only singlet states emit. Some of these emissions are optically thick and the resulting spectrum of emitted radiation out of the atmosphere can be significantly modified, particularly for the CY emissions (see Section 5).

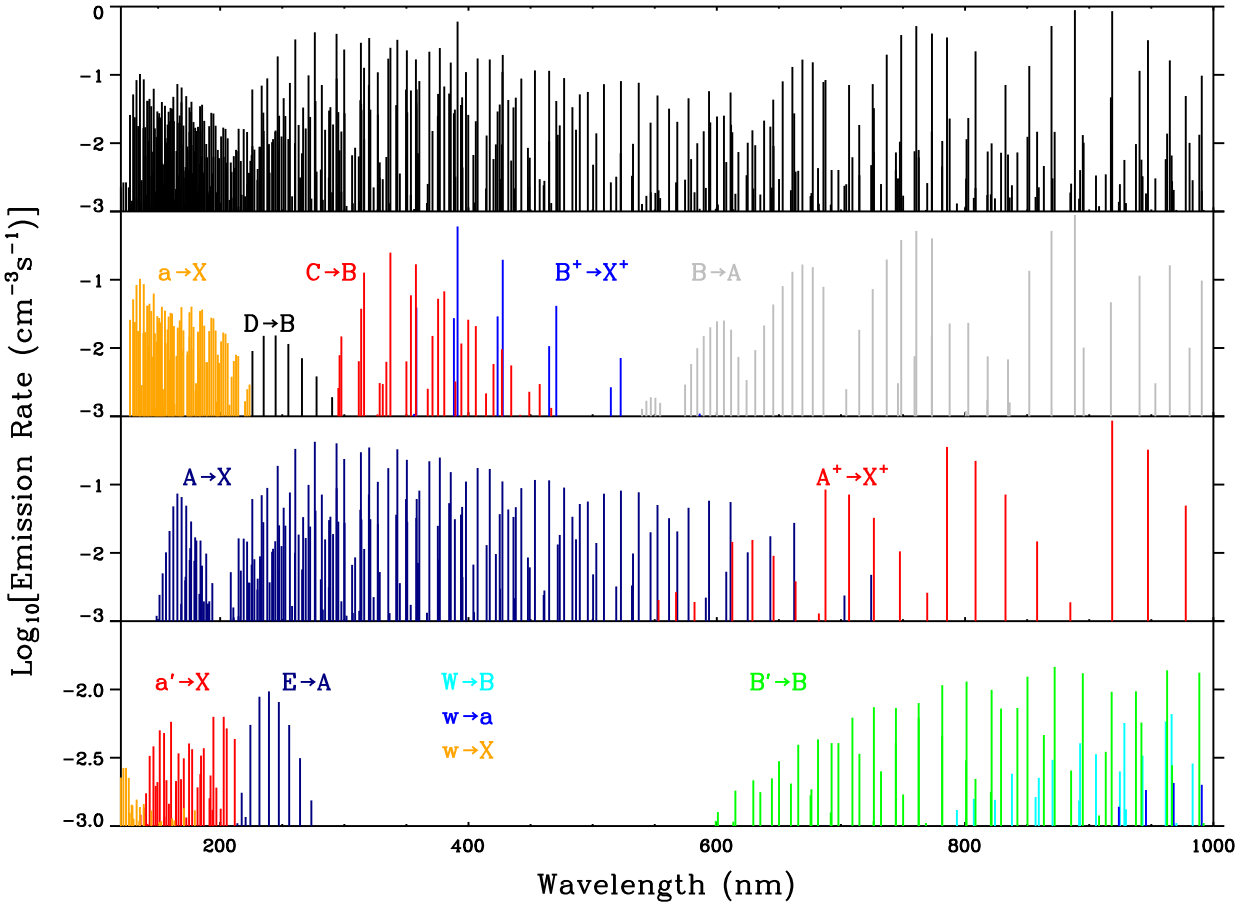

Figure 28: Local emission spectrum between 120 and 1000 nm, from excited N_2 states at 1000 km altitude. The top panel presents the cumulative spectrum and the lower panels present the contributions of the different bands.

tons overlap at similar spectral bands. However, their strong level interactions and pre-dissociation lead to a relatively sparse EUV spectrum (Fig. 27), contrary to the typical band structures observed for the lower energy singlet states (a, a′, w) that emit in the FUV. From the triplet states only the A-state can emit to the ground state leading to a band that extends from the FUV and over the whole visible range (Fig. 28), while the energy of all other triplet states has to stepwise diffuse among themselves before reaching the A-state. As a result, emissions from all other triplet states cover a large part of the spectrum from the visible to the near IR (Fig. 29) depending on the involved energy levels of each transition (see Fig. 1). A similar picture applies for the doublet states as well, with the Meinel band spreading over part of the visible and the near IR, and the 1^{st} negative band having its major contribution close to 400 nm. Most of the long wavelength airglow would be difficult to separate from the thermal emission of Titan's atmosphere (depending on the observation geometry). Emissions though at visible and shorter wavelengths should be observable. Cassini UVIS observations extend up to ∼190 nm and have observed the main bands at shorter wavelengths (Ajello et al., 2007, 2008; Stevens et al., 2011; Ajello et al., 2012; Heays et al., 2014), while broad band observations by Cassini/ISS during eclipse have verified the visible emissions induced by excitation from magnetospheric particles (West et al., 2012; Lavvas et al., 2014). In the future, high resolution observations of good signal to noise ratio should be able to discriminate the contribution of the higher energy singlet states in the EUV spectrum, while observations at visible wavelengths could identify the dominant emissions from the transitions of the B and C triplet states, and the A and B doublet states.

The profiles of photon emission reflect the state production rates defined by the photon and photo-

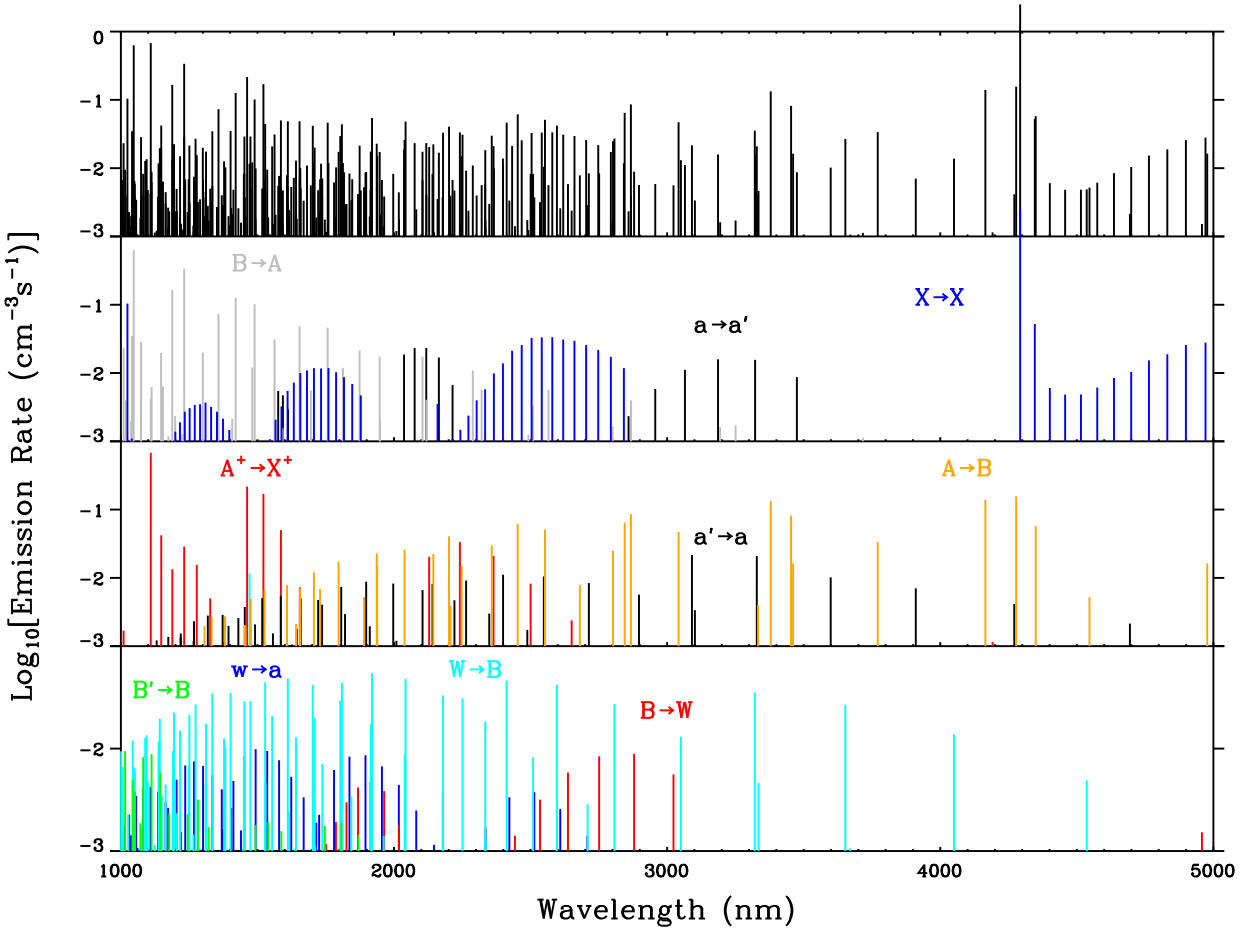

Figure 29: Local emission spectrum in the near IR, from excited N_2 states at 1000 km altitude. The top panel presents the cumulative spectrum and the lower panels present the contributions of the different bands.

electron excitation rates. As collisions become important for some of the states with decreasing altitude, however, the emitted spectra change due to modifications in the vibrational distributions. Thus, spectrally resolved observations for the contribution of different vibrational levels in the emission can yield information about the atmospheric density. A characteristic example is the VK band emission that is partially observed by Cassini/UVIS. The A-state, as we saw earlier, is strongly affected by collisional processes (see Fig. 9), while the a-state of the close-by LBH emission is not. Thus, the relative emission within the LBH system does not change with altitude, while the VK emission within the system is strongly dependent on the choice of vibrational levels observed (Fig. 30). As both states are excited only by photo-electrons, the relative emission in these bands depends on the atmospheric N_2 density, but also on the methane content that will partially absorb photons with energy below ∼155 nm. Thus it is possible to retrieve information for both methane and nitrogen from these observations provided there is a high signal to noise ratio (Stevens et al., 2011, 2015). Emission from other states that are affected by collisions, such as the W- and the a′-states, should have a similar behavior. Nevertheless they would be difficult to observe; the a′-state is affected by collisions only deep in the atmosphere close to 600 km, where local emissions close to 200 nm would be significantly attenuated by the atmosphere (mainly by hydrocarbons), while the weak emission from the W(ν=0)-state that is significantly affected by collisions provides photons in the IR (λ(0,0)=136μm), which would be difficult to separate from the thermal background. Thus, the UV observations are optimal for the retrieval of the atmospheric densities.

In terms of energy output our calculations show that the overall energy emission rate of the triplet

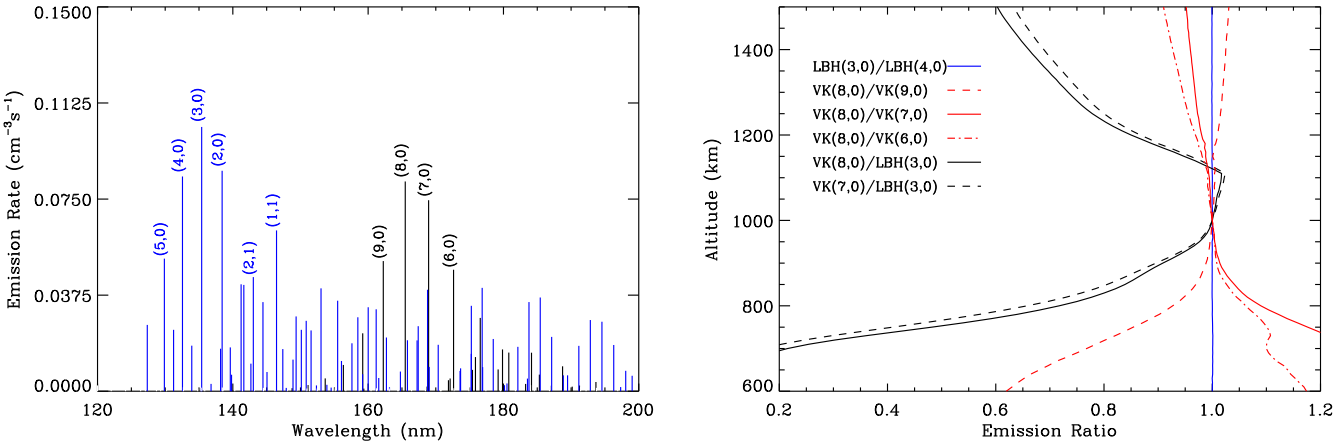

Figure 30: Left: Local emission rates from the LBH (blue) and VK (black) bands at 1000 km altitude. The numbers indicate the vibrational levels of the transition in the form (ν',ν''), where ν' is the vibrational level of the initial state and ν'' the vibrational level of the final state. Right: Ratio of emission rates among the VK and LBH bands. The LBH emission ratios are not affected significantly by collisions (blue line), contrary to the VK emission ratios between different vibrational levels (red lines). Thus, the observed variation of intensity of the VK lines can provide information on the atmospheric density as well as the ratios of emission between the two bands. All ratios are normalized to their value at 1000 km.

states dominates over the doublet and singlet, due to the larger population of the former relative to the latter (Fig. 31). Despite their smaller densities, the high energy of their emitted photons puts the singlet states in the second place of energy emission. The doublet states are third in emitted energy which, however, becomes comparable to that of the singlet states in the lower atmosphere. We discuss the energetic aspects of our calculations in Section 6.

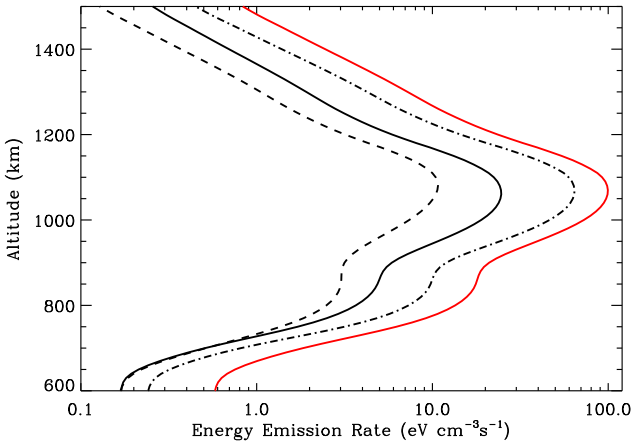

Figure 31: Energy emission rates from singlet (solid), doublet (dashed), and triplet (dash-dotted) states, and the cumulative rate (red).

5. Resonant scattering

For the high energy singlet states resonant scattering is an important complication, which, however, provides us an opportunity to demonstrate the implications of the ground state vibrational distribution. In a nutshell, photons emitted during radiative de-excitation of the singlet states to the ground state levels can be absorbed by N_2 resulting in re-excitation of the singlet states. During this process, energy is gradually lost due to the pre-dissociation of the singlet states, due to absorption of emitted photons by methane, and also due to absorption by vibrationally excited N_2. In the latter case, the nitrogen molecules are excited to different states, which depending on the case of each state can completely pre-dissociate, thereby eliminating any further scattering. For example, the CY(0,1) emission overlaps with the BH(2,0) band that completely pre-dissociates, while emissions to higher vibrational levels correspond to wavelengths beyond the N_2 photo-dissociation limit and can only be absorbed by CH_4, and other minor hydrocarbons (Stevens et al., 1994; Stevens, 2001).

In their recent analysis of EUV airglow, Stevens et al. (2011) found that although the inclusion of resonant scattering significantly improved the model-data comparison, their simulated peak emission for the CY(0,1) was larger by a factor of 2-5. Moreover the observed altitude profiles of both CY(0,1) and CY(0,2) emissions (that depend on the atmo-

spheric density profile) peak at an altitude that is more than 100 km below the anticipated emission peak. In their study, they assumed a thermal population for the vibrational distribution of the ground state. A higher population for the excited X(ν) levels, as we find in our study, can reduce the emissions because more photons are absorbed by the ν>0 levels that leads to excitation of N_2 to states that completely pre-dissociate. Hence, we explore here the impact of this mechanism on the $c'_4(\nu = 0)$ emission. Resonant scattering effects for the other singlet state will be discussed in a future study focusing on the application of the model to specific flyby conditions and observations.

Stevens et al. (1994) were the first to demonstrate that the emissions of the CY(0,0) and CY(0,1) bands from N_2 rich atmospheres are affected by resonant scattering and provide a detailed method for its simulation. We follow closely their approach here. In this procedure, multiple scattering of the resonant photons is taken into account by a sequence of single scattering steps, during which a detailed account of pre-dissociation, absorption, and emission for each band is considered. We use in our calculations cross sections for absorption and emission, and pre-dissociation yields calculated with the CSE model (see Section 2), which allow us to evaluate the role of resonant scattering for transitions to all ground state vibrational levels. In the example presented below we assume a temperature of 150 K, and we also assume that the rotational population of each state/level is characterized by this temperature, therefore the spectral distribution of emitted photons is the same during each scattering event.

Our calculations start with the excitation rate of the $c'_4(\nu = 0)$ level based on the results presented above, and follow the fraction of the excitation that results in emission (f_{dis}=0.133, see Table 1) after each scattering. Depending on the atmospheric opacity at each altitude, photons can be absorbed at a different location than their emission origin, and also escape to space. Our results show that above 900 km pre-dissociation of the $c'_4(\nu = 0)$ state dominates among the loss mechanisms that limit the resonant scattering, while at lower altitudes the losses are dominated by absorption from methane and absorption by vibrationally excited nitrogen that leads to pre-dissociation (Figure 32). The ν >1 ground state levels also enhance significantly the loss by photon escape to space, since photons emitted to these levels are not attenuated by nitrogen.

The increase in the loss rates due to the $\nu > 0$ levels translates to a lower number of scatterings required to reach a specific level of reduction in the excitation after each scattering. In our calculations we apply 30 scattering iterations, which at the end of this process and when all ground state vibrational levels are considered, result in a column excitation rate that

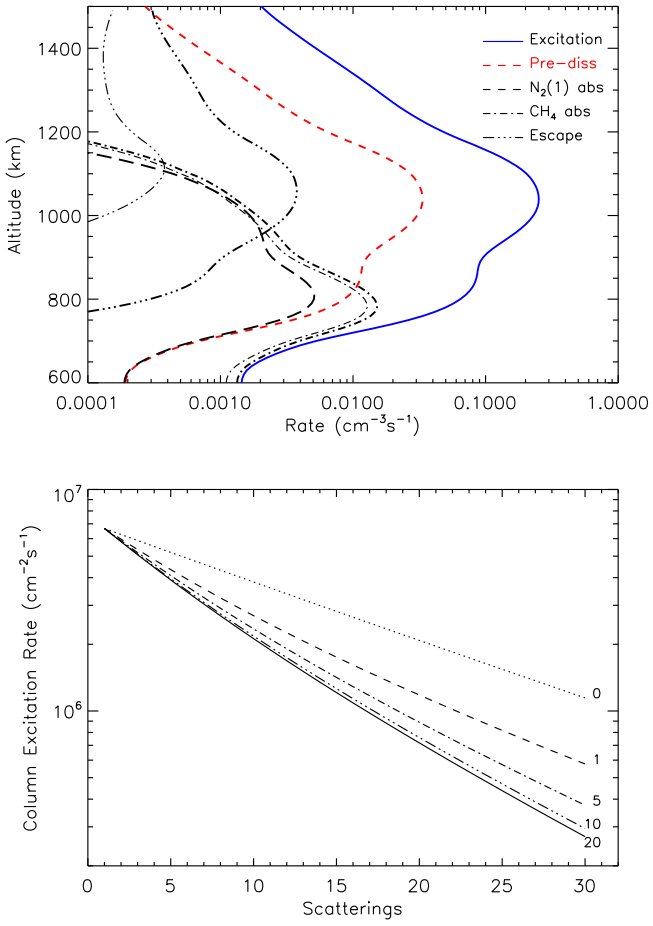

Figure 32: TOP: Rates for different processes affecting the resonant scattering in the CY(0,ν) bands. The blue line represents the original excitation by photons and photoelectrons and the red, dashed line, the loss of photons due to pre-dissociation of the $c'_4(\nu$=0) level. The black, dashed line represents absorption by N_2 X(ν=1) that leads to pre-dissociation through the overlapping BH(2,0) band, and the dash-dotted line represents absorption by CH_4 in all emitting bands. The dash-triple-dotted line represents local loss of photons to space. The thin lines represent the same physical parameters but due to emission to the X(ν=0) level only, demonstrating the contribution of the higher levels for each case. The presented results correspond to only 1 scattering event. BOTTOM: Column excitation rate of $c'_4(\nu$=0) during each scattering. The different lines represent the column rates when a different number of ground state levels is considered.

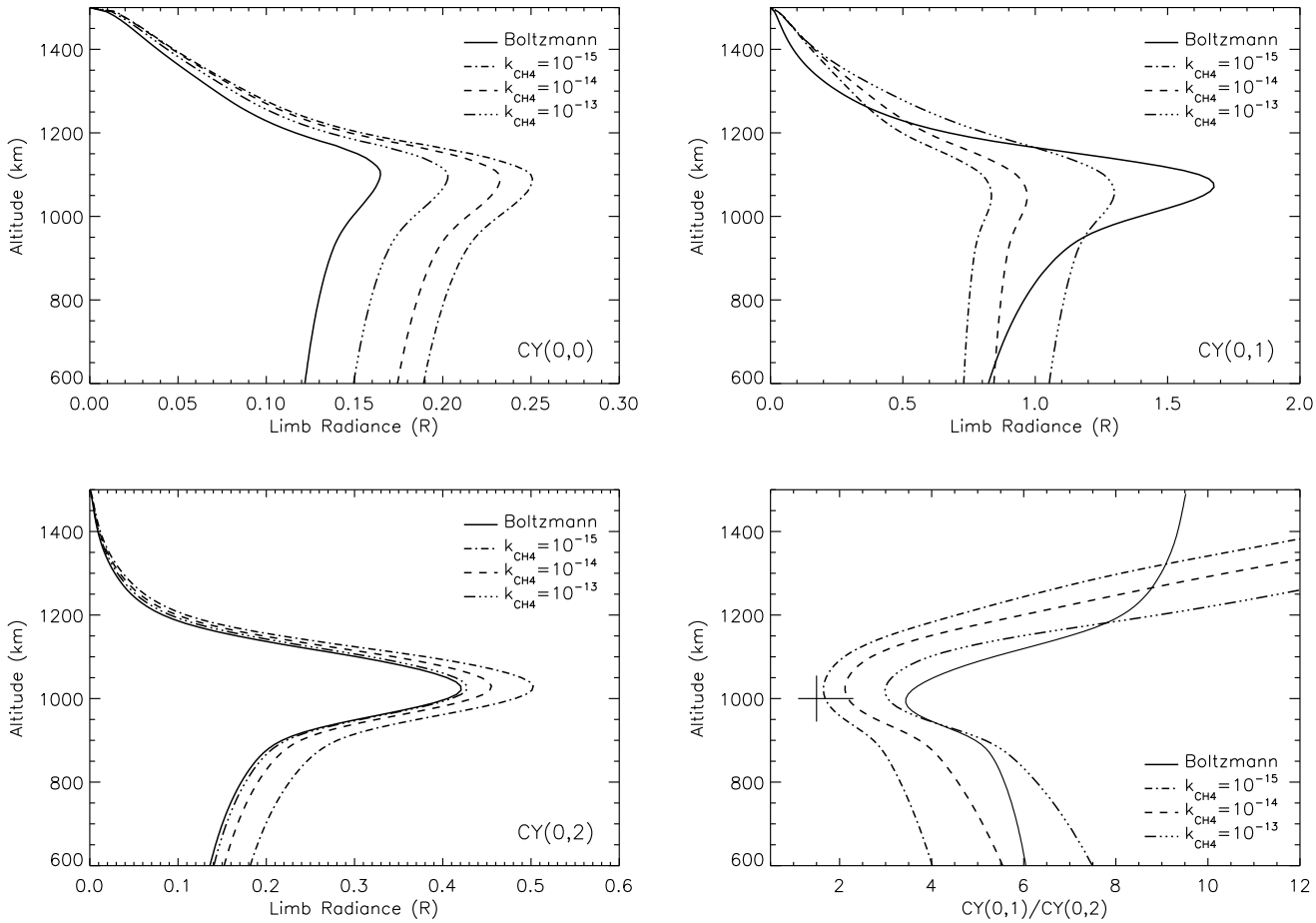

Figure 33: Limb radiances for the CY(0,0), CY(0,1), and CY(0,2) transitions and the altitude profile of CY(0,1)/CY(0,2). Each panel presents the calculated emissions in spherical geometry, assuming different N_2 state vibrational distributions: solid lines correspond to a Boltzmann distribution at 150 K, while the broken lines correspond to the ground state vibrational distributions calculated with our model for the three different values of the vibrational energy transfer rate assumed between N_2 and CH_4 (Sec. 3.4). Their differences demonstrate the importance of the ground state population on the observable emissions. The error bar on the CY(0,1)/CY(0,2) plot is taken from Stevens et al. (2011) based on Cassini/UVIS observations of Titan's airglow. Note that the atmospheric density profiles assumed here and in the latter study are different. The hot N_2 population decreases the simulated CY(0,1)/CY(0,2) ratio at the peak emission altitude to values that are more consistent with the observations.

is ∼20 times smaller than the original excitation rate (Fig. 32). A significantly larger number of scattering events would be required to reach the same level of reduction in the final excitation, if fewer X(ν) vibrational levels were considered. For example, if only the $\nu = 0$ level was able to contribute to this process, the column excitation rate after the same number of scatterings would be only ∼7 times smaller than the original. In addition, our calculations show that the ground state vibrational levels up to $\nu = 10$ can make an important contribution to the resonant scattering, while higher levels have a minor effect (Fig. 32). This dependence results from the decreasing emission rates for the $c'_4(0)\rightarrow X(\nu)$ transitions with increasing ground state level.

In order to evaluate the role of the vibrational distribution of the ground state on the observed emissions from Titan's atmosphere, we need to compare the calculated limb emissions under different assumptions for the ground state population (Fig. 33). For this comparison we use four different scenarios: a case of thermal (Boltzmann) population with a temperature of 150 K, and the three vibrational distributions we calculate under the different scenarios of the N_2-CH_4 vibrational energy exchange rate (see above). The limb emission calculation is done in spherical geometry, taking into account attenuation by N_2 and CH_4.

Our results demonstrate that an increasing vibrational population of the ground state has a clear and observable influence on the anticipated emissions. For the CY(0,0) band, the increasing population of the ground state increases the observed emission because the overall excitation of the $c_4'(0)$ level is enhanced by contributions from the X(ν >0) levels. The ratio of the peak emission at 1100 km between the three vibrational populations calculated and the thermal case ranges between 1.3 and 1.5 for the low and high rate of vibrational energy exchange with methane, respectively. This is a relatively small increase and the resulting emissions are still consistent with the non-detection limit of this band from the UVIS observations.

For the CY(0,1) and CY(0,2) emissions the enhanced excitation due to the hot-N_2 population also increases the resulting emission out of the atmosphere at all altitudes. However, for the CY(0,1) emission the overlap of the emitted photons with the BH(2,0) band results in a further reduction of the photons escaping out of the atmosphere. This process is enhanced due to multiple scattering, which has its maximum effect at the region where the hot N_2 population is higher, i.e. close to 1000 km (Fig. 24). Thus, the CY(0,1) peak limb emission is reduced by factors between 2 and 1.3 for the three calculated distributions relative to the emission assuming a thermal distribution, while at other altitudes the net effect is an increase in the emitted radiation. On the contrary the CY(0,2) emission is increased at all altitudes and the peak emission is enhanced by up to 20% for the low reaction rate with methane. As a result the ratio of the two emissions does not have a monotonic behavior, and the overall effect of the hot vibrational population brings the simulated CY(0,1)/CY(0,2) ratio (Fig. 33) close to the observations from Cassini UVIS (Stevens et al., 2011).

The excited N_2 vibrational distribution also modifies the peak emission altitudes for these bands. Due to the increased pre-dissociation through the BH(2,0) transition and the higher population of hot molecules close to 1000 km relative to the lower altitudes, the peak emission altitude of the CY(0,1) emission is reduced compared to the thermal population case. On the contrary, as photons from the CY(0,2) band are lost only due to methane absorption, multiple scattering at a given altitude increases the total loss due to methane and so the peak of emission shifts to higher altitudes with increasing X(ν=2) population. For the CY(0,1) band the emission peak altitude is lowered by up to 20 km relative to the peak altitude for the thermal case, while for the CY(0,2) emission the peak emission altitude increases by 10 km. Thus, the excited ground state population tends to bring the peak emission altitudes for these two bands closer together.

These variations in the observable emissions for the CY bands demonstrate that the inclusion of the non-thermal vibrational distribution of the ground state, as calculated by our model, brings the simulated airglow results into better agreement with the Cassini observations with regard to the magnitude of the CY(0,1) emission and its ratio with the CY(0,2) emission (Stevens et al., 2011). At this point we should note that the absolute values of the limb radiances and peak altitudes we calculate, although consistent, should not be directly compared with the Stevens et al. (2011) observations as they do not reflect the specific flyby conditions (geometry and solar influx) and atmospheric properties (density profile) during that time. Our purpose here is only to demonstrate that the high vibrational population of the N_2 ground state we calculate is supported by the airglow observations. Finally, we note that among the different vibrational energy exchange cases we consider with methane, the low rate cases (k_{CH4}=10^{-15}-10^{-14} cm^3s^{-1}) provide results that are more consistent with the observations relative to the high rate case that tends to generate vibrational populations that are closer to the Boltzmann distribution.

6. Heating efficiency & energy transfer

As the role of collisions in de-exciting or transforming one excited state to another gradually increases with decreasing altitude, the rate at which photon energy is transformed to thermal energy increases as well. This process of energy transfer is critical for the thermal structure evaluation in the upper atmosphere and we discuss in this section the results of our study regarding this parameter.

An evaluation of the overall heating efficiency from N_2 states needs to consider the rate at which the energy exchange during each collision is transformed to heat. From the description of the production and loss rates of each state we saw that only three neutral and electronically excited states are significantly affected by collisions, the A, W, and a′. Each state/level has a different dependence on the collisional processes,

therefore the overall heating efficiency of each state depends on its vibrational population (Fig. 34).

For the A-state, the effect of collisions gradually increases with vibrational level for ν=0-7 due to the vibrational redistribution process within this state and decreases at higher levels (see Fig. 9). Nevertheless, due to the decreasing population with increasing level (see Fig. 10) the low vibrational levels dominate the overall heating efficiency and result in a weak energy transfer to the atmosphere that accounts for, at maximum, ∼15% of the total loss rate close to 600 km and a monotonic decrease of the heating efficiency towards higher altitudes (Fig. 34).

On the contrary, the W-state presents a non-monotonic altitude behavior that results from the significantly longer radiative lifetime of the ν=0 level relative to the higher levels. The rapid radiative cascade of the higher levels to lower states provides small heating efficiencies, while the ν=0 level survives long enough in the atmosphere to be affected by collisions at high altitudes. Therefore the overall heating efficiency for this state remains high as long as the population of the W(ν=0) level dominates the vibrational population (Fig. 34). As we move to altitudes below 800 km the vibrational distribution of the state becomes more homogeneous (see Fig. 14) and the contribution of the higher levels in the heating efficiency average increases, resulting in a decrease of the overall efficiency from ∼80% close to ∼900 km to 60% at 600 km (Fig. 34).

For the a′-state collisions become important only deep in the atmosphere, below 750 km, and are most efficient for levels ν=2 and ν=3 (see Fig. 20), which also have a significant population in the vibrational distribution. Nevertheless, the collisional processes for this state are always significantly weaker than its radiative cascade, leading to an overall heating efficiency of ∼10% at 600 km (Fig. 34).

The loss rates for the ground neutral and ground ion states are dominated by collisional processes, although not all energy in these processes is transferred to the atmosphere, as we discuss below. All other states are not significantly affected by collisions above 600 km, thus their heating efficiency is practically zero. As we move even deeper in the atmosphere collisions eventually dominate for all states, but at these altitudes the density of the excited states is extremely small.

Although we estimated the heating efficiency as the ratio of the collisional to total loss rates we need

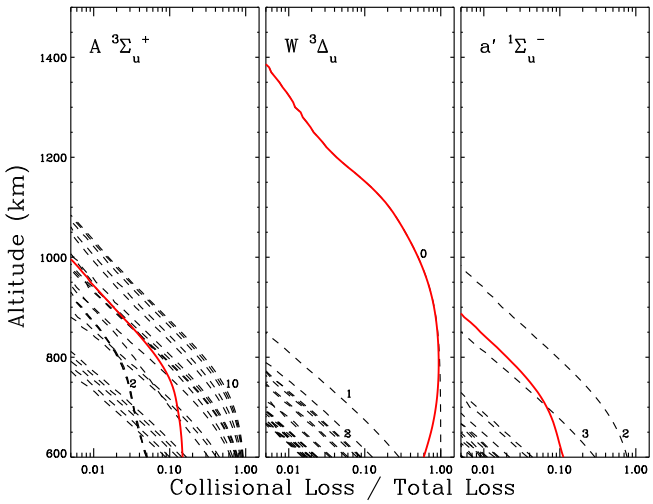

Figure 34: Variation with altitude of the heating efficiency for the A-, W-, and a′-states. We calculate the heating efficiency as the ratio of collisional loss to the total loss for each vibrational level at each altitude. The dashed lines represent the level specific heating efficiency and the red, thick lines, the average efficiency calculated from the vibrational distributions presented in Section 3. Small numbers designate some of the vibrational levels shown.

to be cautious as not all of the energy exchange during a collision results in atmospheric heating (i.e. transfer of energy to the translational degrees of freedom). Part of the energy of the reactants is transformed into internal energy of the products, and the energy difference between the two is the actual energy leading to heating (or cooling) of the atmosphere. One way to evaluate the overall heating efficiency is by calculating the rate at which energy is transformed into different types of energy. The total energy input in the system of the N_2 states is equal to:

$$\left.\frac{dE}{dt}\right|_{input} = \sum_{s,l}(1 - f_{dis}^{s,l})P_{s,l}^{h\nu,e}(E_{s,l}^{f} - E^{i}), \quad (6)$$

where $P^{h\nu,e}$ is the production rate of each state/level from photons and photoelectrons, and the last parenthesis is the energy difference between the final and initial states. Note that since we consider only the energy balance of the N_2 system we multiply every state/level contribution with its excitation yield $(1 - f_{dis}^{s,l})$. From this initial energy budget, part is transferred out of the system through emission:

$$\left.\frac{dE}{dt}\right|_{emiss} = \sum_{s,l}\sum_{s',l'} P_{s,l;s',l'}^{rad}(E_{s,l} - E_{s',l'}), \quad (7)$$

and part through reactions:

$$\left.\frac{dE}{dt}\right|_{react} = \sum_{s,l}\sum_{\chi} L^{react}_{s,l,\chi}\Delta E. \quad (8)$$

In equation 7 we add the energy emission rates for all possible radiative transitions within the N_2 system. For the energy transfer through reactions (eq. 8), we need to consider the possible collision partners, χ. For collisions within the N_2 manifold the energy transferred out of or into the system is due to the energy mismatch of the involved energy levels. For chemical reactions, the energy transferred to methane is equal to the energy difference between the final and initial N_2 state/level reacting with methane. Note that we do not multiply the energy transfer rates out of the N_2 system by the excitation yield of the produced state, as the energy is transferred in each transition whether or not the produced state/level pre-dissociates or not. As the population of the N_2 states can be reduced by pre-dissociation after each radiative transition, the energy lost needs to be accounted through:

$$\left.\frac{dE}{dt}\right|_{pd} = \sum_{s,l} f^{s,l}_{dis} P^{rad,react}_{s,l} E_{s,l}. \quad (9)$$

Through these definitions we calculate the energy transfer rate for the N_2 system (Fig. 35). Our results demonstrate that the main process of energy transfer out of the system is through the chemical reaction with methane, followed by the energy emitted through the radiative cascade. Other collisional processes have only a minor role in the energy transfer. Although only part of the energy transferred to the chemical energy inventory will heat the atmosphere, we can evaluate an effective local heating rate for the N_2 system based on the calculated energy transfer rates using an efficiency:

$$\epsilon = 1 - \left.\frac{dE}{dt}\right|_{emiss} \Big/ \left.\frac{dE}{dt}\right|_{input}. \quad (10)$$

This efficiency in practice describes the relative importance of emitted energy to the total energy input in the N_2 system (Fig. 35). The calculated ϵ values range between 70 and 85% and demonstrate a local minimum close to 1000 km. This non-monotonic decrease of the heating efficiency with increasing altitude is due to the variation of the methane profile with altitude in this region of the atmosphere; diffusive separation allows for the methane mixing ratio to increase above $\sim$ 900 km, which effectively translates to an increase of the efficiency of the energy transfer from the N_2 system to methane.

The heating efficiency derived here does not correspond to the overall heating efficiency in Titan's atmosphere. From the total UV energy deposited in the upper atmosphere a small fraction leads to excitation (which we consider here) while the largest fraction results in complete pre-dissociation. The atomic nitrogen is produced in multiple states and the energy transferred to the fragments is predominantly lost through chemical reactions, while emission from excited atoms (neutrals and ions) makes a secondary contribution to the energy budget. From the excited molecular population, part of its energy is emitted as

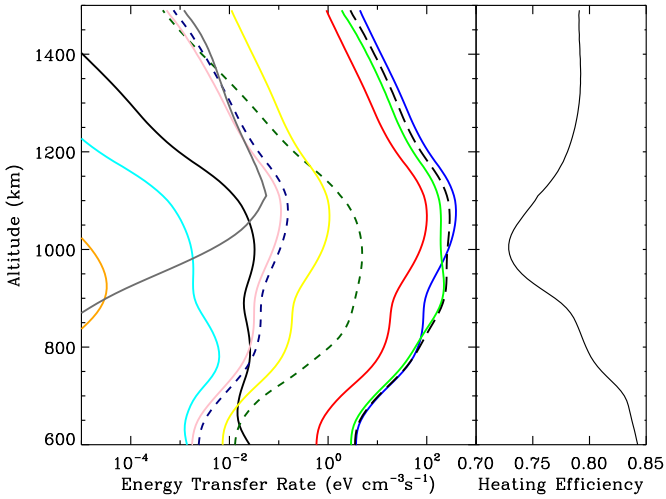

Figure 35: Energy transfer rates for different processes of the excited N_2 population. The blue line represents the total energy input for the excited neutral and ion states (initial pre-dissociation fraction removed). Most of the energy is transferred to chemistry through reactions with methane (light green line), while photon emission from transitions between different states is the second largest energy transfer mode (red line). Other secondary processes include the energy lost out of the N_2 system due to pre-dissociation of the different states (yellow line), and energy transferred during quenching (black line), during VV (dark green line) and VT (orange line) transitions of the ground state, as well as VV (navy line) and VT (pink line) transitions of the ground ion state, and other types of collisions discussed in the text (cyan line). Energy transferred during the dissociative recombination of the ion states is represented by the gray line. Broken lines represent regions where energy transfer is from the atmosphere to the N_2 population (cooling). The black long-dashed line represents the total energy transfer rate out of the N_2 system. Its shape is different from the total input rate (blue line) due to the diffusion of the ground state population. The column integrated rates for input and output are equal, though.

airglow while the largest fraction is transferred to the chemical energy inventory. All other reaction processes have a minor role in the energy balance of the N_2 system. Thus, a complete evaluation of the total energy transfer in Titan's atmosphere requires the consideration of the photochemical energy budget and will be performed in a future study.

7. Implications of hot N_2 for the ionosphere

Our study demonstrates that a large population of vibrationally excited nitrogen is present in Titan's upper atmosphere. Such a population could have important ramifications for the ionospheric densities, as has been demonstrated for the Earth's atmosphere in the past (e.g. Campbell et al., 2006, and references therein). In this case the reaction of O^+ with vibrationally excited nitrogen leads to the formation of NO^+ with a rate that increases with increasing vibrational level of N_2. As O^+ is a major ion in the F region of Earth's ionosphere, this process allows for a faster overall recombination rate, since molecular ions have significantly greater recombination rates than atomic ions. Thus, the excited vibrational population of N_2 in Earth's atmosphere leads to a decrease of the electron density.

A mechanism that would lead to a reduction of the electron density appears necessary in Titan's upper atmosphere as well. Analysis of Cassini observations in Titan's ionosphere demonstrates that the observed electron densities are lower (by a factor of 2) than densities calculated with theoretical models under the conditions of the observations (Vigren et al., 2013). This problem seems to appear only during the daytime conditions where energy deposition is dominated by solar photons. On the contrary, during night-time conditions the observed electron densities were found to be in good agreement with predictions from models of magnetospheric electron ionization (Vigren et al., 2015). Similarly, other studies find that observed densities of some of the ions (including the dominant $C_2H_5^+$ and $HCNH^+$ ions) are smaller than predictions from photochemical models, thereby suggesting a possible lack in our understanding of the loss mechanisms affecting the ionospheric properties (Vuitton et al., 2007; Robertson et al., 2009; Mandt et al., 2012; Sagnières et al., 2015).

The impact of the N_2 vibrational population on Titan's ionosphere must be of a different type than on the Earth's, however. Firstly, the most abundant ions in Titan's atmosphere are already molecules, thus the transformation of atomic to molecular ions with a mechanism similar to that of O^+ for the Earth would have a small influence in the overall electron abundance. Moreover, the observed influx of O^+ ions in Titan's atmosphere is a secondary ionization source compared to solar photons (Hörst et al., 2008), thus their role will be minor for the electron densities (although the possible enchancement of NO formation could be an important consequence, which is beyond the scope of the current study and will be addressed separately).

Notwithstanding the lack of atomic ions, the excited nitrogen molecules can react with the abundant molecular ions. This process can take place at two different steps in the ionospheric chemistry: the population of the primary N_2^+ ion could be homogeneously reduced due to the interaction with the hot N_2 molecules, thereby reducing the total ion and electron densities; or interactions with individual (and long-lived) ions, such as the dominant $HCNH^+$ and $C_2H_5^+$, could differentially affect the ion densities. Unfortunately, for the major ions of interest here the rates and products of these reactions are unknown. We can, however, estimate the magnitude of rates required for these processes to be efficient.

Starting with the homogeneous loss through the possible reduction of N_2^+, the major process defining the abundance of this ion, according to the current understanding, is reaction with methane:

$$\begin{aligned} N_2^+ + CH_4 \rightarrow \quad & CH_2^+/CH_3^+ + 2H/H + N_2 \\ \rightarrow \quad & N_2H^+ + CH_3, \end{aligned}$$

leading to a local loss rate of N_2^+ ions of:

$$\left.\frac{d[N_2^+]}{dt}\right|_{CH_4} = k_{CH_4} \times [CH_4] \times [N_2^+] \simeq 0.1 \times [N_2^+]$$

at 1000 km (brackets designate the number density of the enclosed species). Therefore, any processes induced by the hot N_2 molecules should compete with a rate comparable to the above.

The first process we can consider is the possible variation of the recombination rate of N_2^+ ions with vibrational level, ν. This mechanism though is not efficient, because the vibrational population of hot ions is small, but also because the recombination rate of the hot ions is smaller than the rate for the ground ion level (Bates and Mitchell, 1991).

Reaction of hot N_2^+ ions with methane can lead to the formation of vibrationally excited fragments:

$$N_2^+(\nu) + CH_4 \rightarrow CH_2^+(\nu)/CH_3^+(\nu) + 2H/H + N_2,$$

but this process will be of small importance due to the low abundance of hot ions. Even if the vibrationally excited fragments are formed from the reaction of the ground state ions with vibrationally excited methane molecules (the latter formed due to solar excitation or collisions with hot N_2):

$$N_2^+ + CH_4(\nu) \rightarrow CH_2^+(\nu)/CH_3^+(\nu) + 2H/H + N_2,$$

the vibrationally excited fragments recombine with a rate that is 2.5 times smaller than the ground state fragments (Sheehan and St Maurice, 2004). Moreover, the major loss of the produced ion fragments is through reaction with methane leading to larger mass ions. Thus, this mechanism cannot reduce the ionospheric densities.

Another process that could potentially affect the N_2^+ abundance is the formation of N_4^+, which has a fast recombination rate (2×10^{-6} cm^3s^{-1}, Keister et al., 2014) and could affect the total electron abundance. N_4^+ can be formed through a 3-body reaction:

$$N_2^+ + N_2 + M \rightarrow N_4^+ + M,$$

which, however, is not efficient at Titan's thermospheric pressures ($k_0 = 3\times10^{-28}$ cm^6s^{-1}, Troe, 2005), as it leads to an N_2^+ loss rate of:

$$\frac{d[N_2^+]}{dt} = k_0 \times [N_2]^2 \times [N_2^+] \simeq 10^{-8}[N_2^+]$$

at 1000 km. We do not know if formation through radiative association:

$$N_2^+ + N_2 \rightarrow N_4^+ + hv,$$

is possible for this case, but we can estimate that a reaction rate in the order of 10^{-11} cm^3s^{-1} is required for this process to compete with the loss rate of N_2^+ by methane. Even if radiative association is fast enough, the subsequent loss of N_4^+ ions through recombination would have to compete with reactions with methane, which would make the overall reduction of ionospheric densities small due to the large CH_4 abundance. The latter process has a rate comparable to the N_2^+ + CH_4 reaction rate and predominantly (90%) leads to the formation of CH_4^+ (Smith et al., 1978). Thus, the overall effect of the N_4^+ formation is unlikely to affect the ionospheric balance. Therefore, a homogeneous reduction of the ionospheric densities due to loss of the primary N_2^+ ions seems unlikely from the processes we have considered.

For the individual interaction of the major ions with the hot N_2 population we can consider multiple processes. The simplest case would be the vibrational energy transfer between hot N_2 molecules and the major ions:

$$N_2(\nu) + HCNH^+ \rightarrow HCNH^+(\nu') + N_2(\nu'' < \nu)$$
$$N_2(\nu) + C_2H_5^+ \rightarrow C_2H_5^+(\nu') + N_2(\nu'' < \nu).$$

Yet, for polyatomic ions the recombination rate is not expected to be significantly affected by their vibrational excitation (Vigren et al., 2012), although the branching among the different dissociation channels could be variable, as is known for the case of $HCNH^+$ where vibrational excitation defines the relative production of HCN and HNC (Ishii et al., 2006). Thus, from this perspective the vibrational energy transfer from N_2 to $HCNH^+$ could affect the relative abundance of HCN/HNC in Titan's upper atmosphere, but a quantitative assessment of this problem requires a detailed knowledge of the energy transfer mechanism, which is currently missing.

Another process to consider is the chemical reaction of hot nitrogen molecules with the major ions. The reaction for the ground state N_2 is endothermic, thus it is interesting to investigate if any of the possible reaction channels would be exothermic for the higher vibrational levels. We used formation enthalpies for the different compounds from the NIST database and performed this exercise for the possible products of reaction with the major ions mentioned above. Our results demonstrate that all studied channels are endothermic for all considered vibrational levels of N_2, with the exception of the N_2H^+ formation channel for $\nu\geq7$ when reacting with $C_2H_5^+$, and $\nu\geq9$ for reaction with $HCNH^+$ (Table 6). For these channels to affect the abundance of the major ions, they need to proceed with rates comparable with the dissociative recombination rates of the ions[3]:

$$\frac{d[C_2H_5^+]}{dt} = \alpha_e \times [e^-] \times [C_2H_5^+] \simeq 10^{-3} \times [C_2H_5^+]$$
$$\frac{d[HCNH^+]}{dt} = \alpha_e \times [e^-] \times [HCNH^+] \simeq 10^{-3} \times [HCNH^+]$$

[3]The major loss process for $C_2H_5^+$ is reaction with HCN that leads to the formation of $HCNH^+$. This process is not affecting the overall electron density, though, from the perspective under investigation here.

Table 6: Possible product channels for the reaction of hot N_2 molecules with $C_2H_5^+$ and $HCNH^+$ and the variation of the reaction endothermicity with the vibrational levels of N_2 for ν=1-10. Negative values correspond to exothermic channels. All values are in eV. For higher vibrational levels all channels remain endothermic, with the exception of the N_2H^+ channels.

	N_2 Vibrational Level									
Products	1	2	3	4	5	6	7	8	9	10
$N_2(\nu) + C_2H_5^+ \rightarrow$										
$N_2H^+ + C_2H_4$	1.65	1.36	1.08	0.80	0.53	0.26	−0.01	−0.28	−0.54	−0.79
$NH^+ + C_2H_4 + N$	12.95	12.66	12.38	12.10	11.83	11.56	11.29	11.03	10.77	10.51
$C_2H_4^+ + NH + N$	10.22	9.94	9.65	9.38	9.10	8.83	8.56	8.30	8.04	7.78
$N^+ + NH + C_2H_4$	14.24	13.96	13.68	13.40	13.12	12.85	12.58	12.32	12.06	11.80
$C_2H_5N^+ + N$	6.01	5.72	5.44	5.16	4.89	4.61	4.35	4.08	3.82	3.57
$N_2(\nu) + HCNH^+ \rightarrow$										
$N_2H^+ + HCN$	1.98	1.70	1.41	1.14	0.86	0.59	0.32	0.06	−0.20	−0.46
$NH^+ + HCN + N$	13.28	13.00	12.72	12.44	12.16	11.89	11.63	11.36	11.10	10.84
$HCN^+ + NH + N$	13.64	13.36	13.08	12.80	12.52	12.25	11.99	11.72	11.46	11.20
$N^+ + NH + HCN$	14.58	14.29	14.01	13.73	13.46	13.19	12.92	12.66	12.40	12.14
$NCNH_2^+ + N$	6.54	6.25	5.97	5.69	5.42	5.15	4.88	4.61	4.35	4.10

at 1000 km, where α_e is the recombination rate (1.3×10^{-7} cm^3s^{-1} for $HCNH^+$ and 4.5×10^{-7} cm^3s^{-1} for $C_2H_5^+$ for an electron temperature of 1000 K, Vuitton et al., 2007). The population of hot N_2 molecules at the high vibrational levels that allow for the formation of N_2H^+ is of the order of 10^{-5} mixing ratio (see Fig. 24), and in order for these processes to compete with dissociative recombination their reaction rates must be of the order of 10^{-2} cm^3s^{-1}, which is non-physical. Moreover, the recombination of N_2H^+ proceeds with a rate that is slower than the recombination rates of $C_2H_5^+$ and $HCNH^+$, therefore it would not significantly reduce the atmospheric electron densities. Thus, reactions of hot N_2 molecules with the major ions do not seem able to affect the ionospheric balance either.

The last process we can consider is possible modification of chemical products and rates for different steps of the ion chemistry due to vibrationally excited N_2. This process is similar to the previous mechanisms discussed for $C_2H_5^+$ and $HCNH^+$ but extends to all intermediate steps of the ion-neutral chemical evolution. This process would have to lead to the production of larger ions that recombine faster than the regular ions considered under ground state vibrational population. Since most of the ion-neutral chemistry proceeds through reactions with methane, the processes considered here do not only include reaction with $N_2(\nu)$, but also collisions with vibrationally excited methane, which can be formed through vibrational energy transfer from hot N_2. The possible contribution of these processes is difficult to evaluate because the reaction rates and possible reaction channels for such reactions are not known. Nevertheless, we do not expect these processes to significantly affect the ionospheric balance; from the previous discussion we showed that the mechanisms affecting the intermediate steps of the major ion formation are not going to significantly affect the current understanding, while effects on ions of larger mass than the major ions will have only a small effect on the total electron balance.

8. Conclusions

We have presented a detailed study on the population of all excited electronic states of N_2 in Titan's atmosphere, for vibrational levels that do not completely pre-dissociate. We considered in our calculations excitation by photoelectrons, as in previous studies, but also we included for the first time a detailed description for the excitation of the high energy singlet states by solar photons, using the latest results for the high resolution photo-absorption cross section of N_2 (Lewis et al., 2005b; Heays et al., 2014). Our results demonstrate that excitation by photons dominates over the excitation by electrons at altitudes above 1200 km for the high energy singlet states, and therefore it can increase the emission by these states at EUV wavelengths.

We also included multiple interaction processes between the different levels of radiative and collisional

origin. Our results demonstrate the relative contribution of each process to the final vibrational distribution and population of each state/level and, thereby, to the emissions from each state. Among the electronically excited states only the A-, W(ν=0)-, and a$'$-states are significantly affected by collisions, while the properties of all other states are controlled by the radiative processes. Therefore, among the non-predissociating states, only these three states make an important contribution to the heating rate of Titan's atmosphere.

We also find that a significant population of vibrationally excited ground state molecules survives in Titan's upper atmosphere. For the first excited vibrational level the density is comparable to that of methane, although the exact densities depend on the vibrational energy exchange rate with CH_4, which is not well constrained. We find that this vibrationally excited population of N_2 affects the resonant scattering for its excited singlet states and accounting for it leads to better agreement with the observed emissions from Cassini/UVIS. Particularly we find that the excited ground state levels result in a decrease of the CY(0,1) by a factor of 2, that is close to the required decrease (factor of 3) derived by Stevens et al. (2011) under the assumption of a thermal vibrational distribution. In addition, we find that the non-thermal population brings the altitudes of peak emission for the CY(0,1) and CY(0,2) bands closer.

Finally, we discussed possible implications of the hot N_2 population on the ionospheric chemistry. The processes we considered suggest that there is no significant influence of the $N_2(\nu)$ on the ionospheric balance, although a large number of the reaction rates required for the verification of this conclusion are currently lacking.

9. Acknowledgements

PL and VV are supported by the French space agency (CNES) as Cassini Participating Scientists and by the French National Program of Planetology (PNP). AH was supported by Grant No. 648.000.002 from the Netherlands Organization for Scientific Research (NWO) via the Dutch Astrochemistry Network. MJB and LC acknowledge some financial support from the Australian Research Council through its Centers of Excellence program. MG is partially funded by the Science & Technology Facilities Council (STFC) through the Consolidated Grant to Imperial College London.

10. References

Aboudan, A., Colombatti, G., Ferri, F., and Angrilli, F. (2008). Huygens probe entry trajectory and attitude estimated simultaneously with Titan atmospheric structure by Kalman filtering. *Planetary And Space Science*, 56:573.

Ajello, J. M., Gustin, J., Stewart, I., Larsen, K., Esposito, L., Pryor, W., McClintock, W., Stevens, M. H., Malone, C. P., and Dziczek, D. (2008). Titan airglow spectra from the Cassini Ultraviolet Imaging Spectrograph: FUV disk analysis. *Geophysical Research Letters*, 35(6):L06102.

Ajello, J. M., James, G. K., Franklin, B. O., and Shemansky, D. E. (1989). Medium-resolution studies of extreme ultraviolet emission from N_2 by electron impact - Vibrational perturbations and cross sections of the $c_4' \ ^1\Sigma_u^+$ and $b' \ ^1\Sigma_u^+$ states. *Phys Rev A*, 106(A3):3685–3689.

Ajello, J. M., Stevens, M. H., Stewart, I., Larsen, K., Esposito, L., Colwell, J., McClintock, W., Holsclaw, G., Gustin, J., and Pryor, W. (2007). Titan airglow spectra from Cassini Ultraviolet Imaging Spectrograph (UVIS): EUV analysis. *Geophysical Research Letters*, 34(2):24204.

Ajello, J. M., West, R. A., Gustin, J., Larsen, K., Stewart, A. I. F., Esposito, L. W., McClintock, W. E., Holsclaw, G. M., and Bradley, E. T. (2012). Cassini UVIS observations of Titan nightglow spectra. *Journal Of Geophysical Research-Space Physics*, 117(A12315):1–28.

Bachmann, R., Li, X., Ottinger, C., and Vilesov, A. F. (1992). Molecular-beam study of the collisional intramolecular coupling of $N_2(B^3\Pi g)$ with the $N_2(A^3\Sigma_u^+)$ and $N_2(W^3\Delta_u)$ states. *The Journal of Chemical Physics*, 96(7):5151–5164.

Bachmann, R., Li, X., Ottinger, C., Vilesov, A. F., and Wulfmeyer, V. (1993). Vibrational-state-to-state collision-induced intramolecular energy transfer $N_2(A^3\Sigma_u^+, v''\rightarrow B^3\Pi_g, v')$. *The Journal of Chemical Physics*, 98(11):8606–8625.

Bates, D. R. and Mitchell, J. B. A. (1991). Rate coefficients for $N_2^+(v)$ dissociative recombination. *Planetary and Space Science (ISSN 0032-0633)*, 39:1297–1300.

Bhardwaj, A. and Jain, S. K. (2012). Production of N_2 Vegard-Kaplan and other triplet band emissions in the dayglow of Titan. *Icarus*, 218(2):989–1005.

Billing, G. D. and Fisher, E. R. (1979). VV and VT rate coefficients in N_2 by a quantum-classical model. *Chemical Physics*, 43(3):395–401.

Bishop, J. and Feldman, P. D. (2003). Analysis of the Astro-1/Hopkins Ultraviolet Telescope EUV-FUV dayside nadir spectral radiance measurements. *Journal Of Geophysical Research-Space Physics*, 108(A):1243.

Borst, W. L. (1973). Excitation of metastable $N_2(A^3\Sigma_u^+)$ vibrational levels by electron impact. *The Journal of Chemical Physics*, 59(11):5830.

Cacciatore, M., Kurnosov, A., and Napartovich, A. (2005). Vibrational energy transfer in N_2–N_2 collisions: A new semiclassical study. *The Journal of Chemical Physics*, 123(17):174315–174315–10.

Campbell, L., Brunger, M. J., Cartwright, D. C., and Teubner, P. J. O. (2004). Production of vibrationally excited N_2 by electron impact. *Planetary And Space Science*, 52:815.

Campbell, L., Brunger, M. J., Teubner, P. J. O., and Cartwright, D. C. (2005). Prediction of electron-driven VUV emission in the earth's atmosphere. *Journal of Electron Spectroscopy and Related Phenomena*, 144-147:119–122.

Campbell, L., Cartwright, D. C., Brunger, M. J., and Teubner, P. J. O. (2006). Role of electronic excited N_2 in vibrational excitation of the N_2 ground state at high latitudes. *Journal of Geophysical Research*, 111:A09317.

Campbell, L., Kato, H., Brunger, M. J., and Bradshaw, M. D. (2010). Electron-impact excitation heating rates in the atmosphere of Titan. *Journal of Geophysical Research*, 115(A9):A09320.

Cartwright, D. C. (1978). Vibrational populations of the excited states of N_2 under auroral conditions. *Journal of Geophysical Research*, 83:517.

Clyne, M. A. A. and Heaven, M. C. (1981). Laser-excitation study of triplet CO. *Journal of the Chemical Society, Faraday Transactions 2*, 77(8):1375–1386.

Crandall, D., Kauppila, W., Phaneuf, R., Taylor, P., and Dunn, G. (1974). Absolute cross sections for electron-impact excitation of N_2^+. *Physical Review A*, 9(6):2545–2551.

Dilecce, G., Ambrico, P. F., and De Benedictis, S. (2006). OODR-LIF direct measurement of $N_2(C\ ^3\Pi_u$, v=0–4) electronic quenching and vibrational relaxation rate coefficients by N_2 collision. *Chemical Physics Letters*, 431(4-6):241–246.

Dilecce, G., Ambrico, P. F., and De Benedictis, S. (2010). On the collision quenching of $N_2^+(B\ ^2\Sigma_u^+, v = 0)$ by N_2 and O_2 and its influence on the measurement of E/N by intensity ratio of nitrogen spectral bands. *Journal of Physics D: Applied Physics*, 43(19):195201.

Dreyer, J. W. (1973). Deactivation of N_2 ($A\ ^3\Sigma_u^+$, v=0–7) by ground state nitrogen, ethane, and ethylene measured by kinetic absorption spectroscopy. *The Journal of Chemical Physics*, 58(3):1195–1201.

Dutuit, O., Carrasco, N., Thissen, R., and Vuitton, V. (2013). Critical Review of N, N^+, N_2^+, N^{2+}, and N_2^{2+} Main Production Processes and Reactions of Relevance to Titan's Atmosphere. *The Astrophysical Journal Supplement Series*, 204(20):1–45.

Eastes, R. W. and Dentamaro, A. V. (1996). Collision-induced transitions between the a, a′ and w states of N_2: Can they affect auroral N_2 Lyman-Birge-Hopfield band emissions? *Journal of Geophysical Research*, 101:26931–26940.

Fujimoto, G., Nitzan, A., and Weitz, E. (1976). Diffusion of vibrationally excited molecules. *Chemical Physics*, 15(2):217–225.

Geisen, H, Neuschäfer, D and Ottinger, Ch (1990). State-specific predissociation of $N_2(B^3\Pi_g)$ measured by laser-induced fluorescence on a molecular beam. *The Journal of Chemical Physics*, 92(1):104.

Gilmore, F. R., Laher, R. R., and Espy, P. J. (1992). Franck-Condon Factors, r-Centroids, Electronic Transition Moments, and Einstein Coefficients for Many Nitrogen and Oxygen Band Systems. *Journal of Physical and Chemical Reference Data*, 21(5):1005–1107.

Gordillo-Vazquez, F. J. (2010). Vibrational kinetics of air plasmas induced by sprites. *Journal of Geophysical Research*, 115:A00E25.

Haverd, V. E., Lewis, B. R., Gibson, S. T., and Stark, G. (2005). Rotational effects in the band oscillator strengths and predissociation linewidths for the lowest $^1\Pi_u$–$X^1\Sigma_g^+$ transitions of N_2. *The Journal of Chemical Physics*, 123(21):214304.

Heays, A. N., Ajello, J. M., Aguilar, A., Lewis, B. R., and Gibson, S. T. (2014). The high-resolution extreme ultraviolet spectrum of N_2 by electron impact. *The Astrophysical Journal Supplement Series*, 211(2):28.

Heays, A. N., Dickenson, G. D., Salumbides, E. J., de Oliveira, N., Joyeux, D., Nahon, L., Lewis, B. R., and Ubachs, W. (2011). High-resolution Fourier-transform extreme ultraviolet photoabsorption spectroscopy of $^{14}N^{15}N$. *The Journal of Chemical Physics*, 135(24):244301.

Herron, J. (1999). Evaluated Chemical Kinetics Data for Reactions of N (D), N (P), and N (A Σ) in the Gas Phase. *Journal of Physical and Chemical Reference Data*, 28(5):1453–1483.

Hörst, S. M., Vuitton, V., and Yelle, R. V. (2008). Origin of oxygen species in Titan's atmosphere. *Journal of Geophysical Research*, 113:10006.

Ishii, K., Tajima, A., Taketsugu, T., and Yamashita, K. (2006). Theoretical Elucidation of the Unusually High [HNC]/[HCN] Abundance Ratio in Interstellar Space: Two-dimensional and Two-State Quantum Wave Packet Dynamics Study on the Branching Ratio of the Dissociative Recombination Reaction $HCNH^+ + e^- \rightarrow HNC/HCN + H$. *The Astrophysical Journal*, 636(2):927–931.

Kato, S., Bierbaum, V. M., and Leone, S. R. (1998). Multiquantum Vibrational Deactivation of N_2^+(v) by Collisions with N_2 and O_2 at Thermal Energies. *Journal of Physical Chemistry A*, 102(33):6659–6667.

Keister, K. E., Wagner, C. J., Putney, J. L., Hewitt, J. D., and Eden, J. G. (2014). Determination of Ar_2^+ and N_4^+ recombination coefficients by subpicosecond multiphoton ionization at 248 nm and microwave interferometry. *Physical Review A*, 89(013401):1–11.

Kirillov, A. S. (1998). The calculation of TV, VT, VV, VV' - rate coefficients for the collisions of the main atmospheric components. *Annales Geophysicae*, 16:838.

Kirillov, A. S. (2008). The study of intermolecular energy transfers in electronic energy quenching for molecular collisions N_2-N_2, N_2-O_2, O_2-O_2. *Annales Geophysicae*, 26(5):1149–1157.

Kirillov, A. S. (2011). Calculation of the quenching rate constants for electronically excited singlet molecular nitrogen. *Technical Physics*, 56:1731–1736.

Kurnosov, A., Napartovich, A., Shnyrev, S., and Cacciatore, M. (2007). Vibrational Energy Exchanges in Nitrogen: Application of New Rate Constants for Kinetic Modeling. *Journal of Physical Chemistry A*, 111(30):7057–7065.

Kurnosov, A. K., Napartovich, A. P., Shnyrev, S. L., and Cacciatore, M. (2010). A database for V–V state-to-state rate constants in N_2–N_2 and N_2–CO collisions in a wide temperature range: dynamical calculations and analytical approximations. *Plasma Sources Science and Technology*, 19(4):045015.

Laher, R. R. and Gilmore, F. R. (1991). Improved fits for the vibrational and rotational constants of many states of nitrogen and oxygen. *J. Phys. Chem. Ref. Data*, 20(4):685–712.

Laporta, V., Celiberto, R., and Wadehra, J. M. (2012). Theoretical vibrational-excitation cross sections and rate coefficients for electron-impact resonant collisions involving rovibrationally excited N_2 and NO molecules. *Plasma Sources Science and Technology*, 21(5):055018.

Lavvas, P., Galand, M., Yelle, R. V., Heays, A. N., Lewis, B. R., Lewis, G. R., and Coates, A. J. (2011). Energy deposition and primary chemical products in Titan's upper atmosphere. *Icarus*, 213(1):233–251.

Lavvas, P., West, R. A., Gronoff, G., and Rannou, P. (2014).

Titan's emission processes during eclipse. *Icarus*, 241:397–408.

Lavvas, P. P., Coustenis, A., and Vardavas, I. M. (2008). Coupling photochemistry with haze formation in Titan's atmosphere, part I: Model description. *Planetary And Space Science*, 56(1):27–66.

Lewis, B. R., Gibson, S. T., Sprengers, J. P., Ubachs, W., Johansson, A., and Wahlström, C. G. (2005a). Lifetime and predissociation yield of $^{14}N_2$ b $^1\Pi_u$(v=1) revisited: Effects of rotation. *The Journal of Chemical Physics*, 123(23):236101.

Lewis, B. R., Gibson, S. T., Zhang, W., Lefebvre-Brion, H., and Robbe, J. M. (2005b). Predissociation mechanism for the lowest $^1\Pi_u$ states of N_2. *The Journal of Chemical Physics*, 122(14):144302.

Lewis, B. R., Heays, A. N., and Gibson, S. T. (2008). A coupled-channel model of the $^3\Pi_u$ states of N_2: Structure and interactions of the 3sσ $F_3\,^3\Pi_u$ and 3pπ_u $G_3\,^3\Pi_u$ Rydberg states. *Journal of Chemical Physics*, 129(164306):1–10.

Liu, X., Heays, A. N., Shemansky, D. E., Lewis, B. R., and Feldman, P. D. (2009). Analysis of terrestrial thermospheric N_2 $c_4'\,^1\Sigma_u^+(0)$~b$'\,^1\Sigma_u^+(1)$ - X $^1\Sigma_g^+$ dayglow emission observed by the Far Ultraviolet Spectroscopic Explorer. *Journal of Geophysical Research*, 114(D7):D07304.

Liu, X., Shemansky, D. E., Malone, C. P., Johnson, P. V., Ajello, J. M., Kanik, I., Heays, A. N., Lewis, B. R., Gibson, S. T., and Stark, G. (2008). Experimental and coupled-channels investigation of the radiative properties of the N_2 c_4' $^1\Sigma_u^+$ - X $^1\Sigma_g^+$ band system. *Journal of Geophysical Research*, 113(A02304):1–17.

Lofthus, A. and Krupenie, P. H. (1977). The spectrum of molecular nitrogen. *Journal of Physical and Chemical Reference Data*, 6:113–307.

Malone, C. P., Johnson, P. V., Liu, X., Ajdari, B., and Kanik, I. (2012). Integral cross sections for the electron-impact excitation of the $b\,^1\Pi_u$, $c_3\,^1\Pi_u$, $o_3\,^1\Pi_u$, $b'\,^1\Sigma_u^+$, $c_4'\,^1\Sigma_u^+$, $G\,^3\Pi_u$, and $F\,^3\Pi_u$ states of N_2. *Physical Review A*, 85(062704):1–17.

Mandt, K. E., Gell, D. A., Perry, M., Hunter Waite, J. J., Crary, F. A., Young, D., Magee, B. A., Westlake, J. H., Cravens, T., Kasprzak, W., Miller, G., Wahlund, J.-E., Ågren, K., Edberg, N. J. T., Heays, A. N., Lewis, B. R., Gibson, S. T., de La Haye, V., and Liang, M.-C. (2012). Ion densities and composition of Titan's upper atmosphere derived from the Cassini Ion Neutral Mass Spectrometer: Analysis methods and comparison of measured ion densities to photochemical model simulations. *Journal of Geophysical Research*, 117(E):E10006.

Margottin-Maclou, M., Doyennette, L., and Henry, L. (1971). Relaxation of Vibrational Energy in CO, HCl, CO_2, and N_2O. *Applied Optics*, 10(8):1768–1780.

Morrill, J. S. and Benesch, W. M. (1996). Auroral N_2 emissions and the effect of collisional processes on N_2 triplet state vibrational populations. *Journal of Geophysical Research*, 101:261.

Ottinger, C., Vilesov, A. F., and Xu, D. D. (1995). Isotopic study of the intermolecular versus intramolecular energy transfer in the N_2(W,A)+N_2(X) reactions. *The Journal of Chemical Physics*, 102(4):1673.

Pereira, L., Morozov, A., Fraga, M. M., Heindl, T., Krücken, R., Wieser, J., and Ulrich, A. (2010). Temperature dependence of the quenching of N_2(C $^3\Pi_u$) by N_2(X) and O_2(X). *The European Physical Journal D*, 56(3):325–334.

Piper, L. G. (1988a). State-to-state N_2(A $^3\Sigma_u^+$) energy-pooling reactions. I. The formation of N_2(C $^3\Pi_u$) and the Herman infrared system. *The Journal of Chemical Physics*, 88(1):231–239.

Piper, L. G. (1988b). State-to-state $N_2(A^4\Sigma_u^+)$ energy pooling reactions. II. The formation and quenching of $N_2(B^3\Pi_g$, v'=1–12). *The Journal of Chemical Physics*, 88(11):6911.

Piper, L. G. (1989). The excitation of $N_2(B^3\Pi_g$, v=1–12) in the reaction between $N_2(A^3\Sigma_u^+)$ and N_2(X, v≥5). *The Journal of Chemical Physics*, 91(2):864–873.

Piper, L. G. (1994). Further observations on the nitrogen orange afterglow. *The Journal of Chemical Physics*, 101(12):10229–10236.

Piper, L. G. (2002). Energy Transfer Kinetics of N_2(X $^1\Sigma_u^+$, v) and SiH_4. *Journal Of Physical Chemistry A*, 106(36):8355–8365.

Popov, N. A. (2013). Vibrational kinetics of electronically-excited $N_2(A\,^3\Sigma_u^+, v)$ molecules in nitrogen discharge plasma. *Journal of Physics D: Applied Physics*, 46(35):355204.

Press, W. H., Teukolsky, S. A., Vetterling, W. T., and Flannery, B. P. (2007). *Numerical Recipes: The Art of Scientific Computing (3rd ed.)*. New York: Cambridge University Press.

Robertson, I. P., Cravens, T. E., Waite, J. H., Yelle, R. V., Vuitton, V., Coates, A. J., Wahlund, J.-E., Ågren, K., Mandt, K., Magee, B., Richard, M. S., and Fattig, E. (2009). Structure of Titan's ionosphere: Model comparisons with Cassini data. *Planetary And Space Science*, 57(1):1834–1846.

Sagnières, L. B. M., Galand, M., Cui, J., Lavvas, P., Vigren, E., Vuitton, V., Yelle, R. V., Wellbrock, A., and Coates, A. J. (2015). Influence of local ionization on the ionospheric densities in Titan's upper atmosphere. *Journal of Geophysical Research*, under review.

Shaw, D. A., Holland, D., MacDonald, M. A., and Hopkirk, A. (1992). A study of the absolute photoabsorption cross section and the photionization quantum efficiency of nitrogen from the ionization threshold to 485 Å. *Chemical Physics*, 166:379–391.

Sheehan, C. H. and St Maurice, J. P. (2004). Dissociative recombination of the methane family ions: rate coefficients and implications. *Advances in Space Research*, 33(2):216–220.

Smith, D., Adams, N. G., and Miller, T. M. (1978). A laboratory study of the reactions of N^+, N_2^+, N_3^+, N_4^+, O^+, O_2^+, and NO^+ ions with several molecules at 300K. *The Journal of Chemical Physics*, 69(1):308.

Sohlberg, K. (1999). Mechanism of efficient V–V in collisions of $N_2^+(\nu>0)$ with N_2. *Chemical Physics*, 246(1-3):307–313.

Stahel, D., Leoni, M., and Dressler, K. (1983). Nonadiabatic representations of the $^1\Sigma_u^+$ and $^1\Pi_u$ states of the N_2 molecule. *The Journal of Chemical Physics*, 79(6):2541–2558.

Stark, G., Huber, K. P., Yoshino, K., Smith, P. L., and Ito, K. (2005). Oscillator strength and linewidth measurements of dipole-allowed transitions in $^{14}N_2$ between 93.5 and 99.5nm. *The Journal of Chemical Physics*, 123(21):214303.

Stark, G., Lewis, B. R., Heays, A. N., Yoshino, K., Smith, P. L., and Ito, K. (2008). Oscillator strengths and line widths of dipole-allowed transitions in $^{14}N_2$ between 89.7 and 93.5 nm. *Journal of Chemical Physics*, 128(1):4302.

Stephenson, J. C. and Mosburg, E. R. J. (1974). Vibrational energy transfer in CO from 100 to 300 °K. *The Journal of*

Chemical Physics, 60(9):3562.

Stevens, M. H. (2001). The EUV airglow of Titan: Production and loss of N_2 $c_4'(0)$-X. *Journal of Geophysical Research*, 106:3685–3689.

Stevens, M. H., Evans, J. S., Lumpe, J., Westlake, J. H., Ajello, J. M., Bradley, E. T., and Esposito, L. W. (2015). Molecular nitrogen and methane density retrievals from Cassini UVIS dayglow observations of Titan's upper atmosphere. *Icarus*, 247:301–312.

Stevens, M. H., Gustin, J., Ajello, J. M., Evans, J. S., Meier, R. R., Kochenash, A. J., Stephan, A. W., Stewart, A. I. F., Esposito, L. W., McClintock, W. E., Holsclaw, G., Bradley, E. T., Lewis, B. R., and Heays, A. N. (2011). The production of Titan's ultraviolet nitrogen airglow. *Journal of Geophysical Research*, 116(A):05304.

Stevens, M. H., Meier, R. R., Conway, R. R., and Strobel, D. F. (1994). A resolution of the N_2 Carroll-Yoshino (c_4' - X) band problem in the Earth's atmosphere. *Journal of Geophysical Research (ISSN 0148-0227)*, 99:417–433.

Strickland, D. J., Bishop, J., Evans, J. S., Majeed, T., Shen, P. M., Cox, R. J., Link, R., and Huffman, R. E. (1999). Atmospheric ultraviolet radiance integrated code (AURIC): theory, software architecture, inputs, and selected results. *Journal of Quantitative Spectroscopy and Radiative Transfer*, 62:689–742.

Strobel, D. F., Meier, R. R., Summers, M. E., and Strickland, D. J. (1991). Nitrogen airglow sources: Comparison of Triton, Titan, and Earth. *Geophysical Research Letters*, 18(4):689–692.

Thomas, J. M., Kaufman, F., and Golde, M. F. (1987). Rate constants for electronic quenching of N2(A 3Σ+u, v=0–6) by O2, NO, CO, N2O, and C2H4. *The Journal of Chemical Physics*, 86:6885–6892.

Tilford, S. G. and Benesch, W. M. (1976). Absorption oscillator strengths for the a′ $^1\Sigma_u^-$-X $^1\Sigma_g^+$ and w $^1\Delta_u$-X $^1\Sigma_g^+$ transitions of molecular nitrogen. *Journal Of Chemical Physics*, 64(8):3370–3374.

Troe, J. (2005). Temperature and pressure dependence of ion-molecule association and dissociation reactions: the $N_2^+ + N_2$ (+ M)→ N_4^+(+ M) reaction. *Physical Chemistry Chemical Physics*, 7:1560.

van der Kamp, A. B., Siebbeles, L. D. A., van der Zande, W. J., and Cosby, P. C. (1994). Evidence for predissociation of N_2 $a^1\Pi_g$(v7) by direct coupling to the $A'^5\Sigma_g^+$ state. *The Journal of Chemical Physics*, 101(11):9271–9279.

Vigren, E., Galand, M., Yelle, R. V., Cui, J., Wahlund, J.-E., Ågren, K., Lavvas, P. P., Mueller-Wodarg, I. C. F., Strobel, D. F., Vuitton, V., and Bazin, A. (2013). On the thermal electron balance in Titan's sunlit upper atmosphere. *Icarus*, 223(1):234–251.

Vigren, E., Galand, M., Yelle, R. V., Wellbrock, A., Coates, A. J., Snowden, D., Cui, J., Lavvas, P., Edberg, N. J. T., Shebanits, O., Wahlund, J.-E., Vuitton, V., and Mandt, K. (2015). Ionization balance in Titan's nightside ionosphere. *Icarus*, 248:539–546.

Vigren, E., Semaniak, J., Hamberg, M., Zhaunerchyk, V., Kaminska, M., Thomas, R. D., Ugglas, M. a., Larsson, M., and Geppert, W. D. (2012). Dissociative recombination of nitrile ions with implications for Titan's upper atmosphere. *Planetary And Space Science*, 60(1):102–106.

Vuitton, V., Yelle, R. V., and McEwan, M. J. (2007). Ion chemistry and N-containing molecules in Titan's upper atmosphere. *Icarus*, 191(2):722–742.

West, R. A., Ajello, J. M., Stevens, M. H., Strobel, D. F., Gladstone, G. R., Evans, J. S., and Bradley, E. T. (2012). Titan airglow during eclipse. *Geophysical Research Letters*, 39(1):18204.

Wu, C. Y. R., Judge, D. L., Tsai, M. H., Lin, Y. C., Yih, T. S., Lo, J. I., Fung, H. S., Lee, Y. Y., Lewis, B. R., Heays, A. N., and Gibson, S. T. (2012). Experimental verification of strong rotational dependence of fluorescence and predissociation yield in the b $^1\Pi_u$(v = 1) level of $^{14}N_2$. *Journal of Chemical Physics*, 136(4):4301.

Xu, Y., Chang, Y. C., Lu, Z., and Ng, C. Y. (2013). Absolute integral cross sections and product branching ratios for the vibrationally selected ion-molecule reactions: N_2^+($X^2\Sigma_g^+$; v^+= 0-2) + CH_4. *The Astrophysical Journal*, 769(1):72.